博士論文

Manganese Oxide Water Oxidation Catalysts and Application to Proton Exchange Membrane Electrolyzers

（酸化マンガン酸素発生触媒と
その固体高分子形電解槽への応用）

林　徹

Table of Contents

List of Abbreviations

Abbreviation	Meaning
AEM	alkaline exchange membrane
ATP	adenosine triphosphate
BET	Brunauer–Emmett–Teller
CMD	chemical manganese dioxide
CODH	carbon monoxide (CO) dehydrogenase
CPET	concerted proton–electron transfer
CV	cyclic voltammetry
DFT	density functional theory
EC-MS	electrochemical mass spectroscopy
EELS	electron energy loss spectroscopy
EMD	electrolytic manganese dioxide
ENDOR	electron nuclear double resonance
EPR	electron paramagnetic resonance
EXAFS	extended X-ray absorption fine structure
FT	Fourier transform
FTO	fluorine-doped tin oxide
H/D KIE	hydrogen/deuterium kinetic isotope effect
HER	hydrogen evolution reaction
ICP-AES	inductively coupled plasma atomic emission spectroscopy
IR	infrared
ITO	indium tin oxide
KIE	kinetic isotope effect
LSV	linear sweep voltammetry
NADP	nicotinamide adenine dinucleotide phosphate
NHE	normal hydrogen electrode
NP	nanoparticle
OER	oxygen evolution reaction
OMS	oxygen microsensor
ORR	oxygen reduction reaction
PC	plastocyanin
PCET	proton-coupled electron transfer
PEC	photoelectrochemical
PEM	proton exchange membrane or polymer electrolyte membrane
PQ	plastoquinone
PSI	photosystem I
PSII	photosystem II
PTFE	polytetrafluoroethylene
PV	photovoltaic
QM/MM	quantum mechanics/molecular mechanics
RDE	rotating disk electrode
RDS	rate-determining step
RHE	reversible hydrogen electrode
RIXS	resonant inelastic X-ray scattering spectroscopy
SAED	selected area electron diffraction
SEM	scanning electron microscopy
SERS	surface-enhanced Raman spectroscopy
SHE	standard hydrogen electrode
STH	solar-to-hydrogen
TEM	transmission electron microscopy
TOF	turnover frequency
TON	turnover number
UV–vis	ultraviolet–visible
VIE	vertical ionization energy
XANES	X-ray absorption near edge structure
XAS	X-ray absorption spectroscopy
XES	X-ray emission spectroscopy
XFEL	X-ray free electron lasers
XRD	X-ray diffraction

Chapter 1.
General Introduction

1.1 Background and Objective of This Study

Establishment of sustainable energy supply is one of the major global challenges to maintain the modern civilization and to further advance it to provide more people with more choices.[1–4] According to International Energy Agency, however, human beings currently rely on fossil fuels, which are not renewable, to meet ~80% of the energy demand.[5] Not only is the reliance on fossil fuels unsustainable but also it causes environmental problems represented by the increase of atmospheric carbon dioxide concentration.[6] The consensus of the majority of people on the Earth about the necessity to reduce carbon dioxide emission is represented by Paris Agreement sealed in 2015.[7] It is strongly required to increase the usage of renewable energy to replace fossil fuels.

Fluctuation of the output, however, is one of the significant factors which impede the penetration of renewable energy, such as solar and wind energy, requiring the development of energy storage methods suitable for practical use. Among storage methods, the importance of the conversion of renewable energy to storable chemical energy, or chemical fuels represented by hydrocarbon and hydrogen gas, will never disappear, because it will also help replace fossil fuels as raw materials in the chemical industry. The conversion of renewable energy to storable chemical fuels can be achieved by (photo)electrochemical methods to reduce carbon dioxide to hydrocarbon or protons to hydrogen gas.[1,3,4,8–12] In either case, an electron donor to be oxidized is required, and water is a desirable candidate because of its abundance in Nature and non-toxicity. The oxygen evolution reaction (OER) by water oxidation ($2H_2O \rightarrow O_2 + 4H^+ + 4e^-$), however, is a multi-electron transfer reaction which requires four-electron and four-proton transfer and kinetically slow, which often limits the energy conversion efficiency.[13] Thus, the development of

novel materials which can efficiently and stably catalyze the OER is one of the most significant challenges for the establishment of renewable energy storage systems.

In continuous researches conducted so far, it has been found that, in alkaline conditions, not only noble metal catalysts but also cobalt (Co)-, nickel (Ni)-, and manganese (Mn)-based catalysts function as active catalysts for the OER (Section 1.3.2.2 and 1.3.2.4). Nevertheless, currently, catalysts known to be active for the OER by oxidizing water of neutral pH are limited to noble metal materials which contain iridium (Ir) or ruthenium (Ru) (Section 1.3.2.2).[14] For the ultimate usage of water as chemical sources, it has been highly desired to construct catalysts which can efficiently catalyze the OER by oxidation of abundant neutral water, by using non-critical first-row transition metal elements.

Against this background, this study aimed to explore the methodology to maximize the multi-electron-transfer ability of Mn oxides, which exist abundantly in Nature, as the catalysts for the OER. To be more precise, this study tried to regulate reaction pathways by developing the methodology to install ligands for the induction of concerted proton–electron transfer (CPET) or structural distortion to the Mn oxide crystals. According to the previous reports, the rate-determining step (RDS) for the OER catalyzed by Mn oxides is the generation of Mn^{3+}, which possesses degenerated electronic state of e_g orbitals.[15,16] Also, it was revealed that the potential required for the generation of Mn^{3+} can be lowered by the introduction of organic ligands to induce CPET[17] or to introduce Jahn-Teller distortion,[18] enhancing the OER activity of Mn oxides. In these systems, however, the activity gradually deteriorated because of the decomposition of organic ligands. Thus, in this study, Mn^{3+} was tried to be stabilized by the introduction of stable ligands or the allowance of structural distortion by decreasing the size of Mn oxides to nanoparticles (NPs). Here, as to the Mn_4 cluster ($CaMn_4O_x$) in photosystem II (PSII), which is the only catalytic site for the OER known in Nature,[19] the importance of surrounding amino-acid

residues and the distorted structure with Mn–O bonds longer than those in Mn oxides has been pointed out. Thus, clarification of the relationship between the multi-electron-transfer ability of Mn oxides and the ligand environment or structural distortion will also lead to the further understanding of the evolution of PSII. Also, this study investigated the utilization of high OER activity of Mn oxides achieved by the usage of ligands or the control of structural distortion in proton exchange membrane or polymer electrolyte membrane (PEM) electrolyzers, whose energy loss is low.[20]

1.2 Overview of This Dissertation

This dissertation consists of five chapters. In Chapter 1, first, the background, objective, and the brief overview of this dissertation are herein summarized. The general introduction of natural oxygenic photosynthesis and artificial catalysts for the OER then follows. Current challenges regarding remaining problems in both experimental achievement and theoretical approaches on the OER catalysts are also pointed out.

In Chapter 2, attention was focused on the amino-acid residues around the Mn_4 cluster in PSII as the candidates for the ligands which are stable and meet acid–base rule (libido rule)[21] required to induce CPET. The ligands of the Mn_4 cluster stably exist during the OER, and the turnover number (TON) reaches as high as ~10^6.[22] Therefore, the surface coordination structure and anodic reactions were investigated using artificial amino-acid analogs and the electrode of α-MnO_2, which has been proposed to be the origin of the Mn_4 cluster.[23,24] After the addition of benzoate into the electrolyte, the overpotential for the OER decreased in accordance with the cathodic shift of the onset potential of the anodic current. It was revealed that benzoate induced CPET during this enhancement of the OER activity by the measurement of electrokinetics based on Tafel plots and pH-dependence of overpotential, as well as hydrogen/deuterium (H/D) kinetic isotope effect (KIE). Also, it was demonstrated by infrared (IR) absorption spectroscopy that benzoate constituted outer-sphere complexes *via* water molecules on the surface of α-MnO_2, the same configuration to the coordination structure of aspartate-61 in the D1 subunit of PSII (D1-Asp61) on the Mn_4 cluster.[25] On the other hand, when imidazole was added, the lower onset potential of the anodic current than that of the OER revealed the existence of the potential region where only imidazole oxidation proceeds. Addition of guanidine did not cause obvious changes of the anodic current nor the OER. Overall, it was revealed that benzoate, with a carboxyl group, which accounts for six to seven direct amino-acid ligands of the Mn_4 cluster[25] and is suggested to act as

a proton acceptor,[26–28] constituted outer-sphere complexes on the surface of α-MnO_2 and induced CPET, stably facilitating the OER activity. The high ratio of the carboxyl group in the ligands is a distinctive feature of the Mn_4 cluster. There is a possibility that carboxyl groups were selectively incorporated as the ligand which can stably activate Mn reaction center in the course of evolution of PSII. The results which revealed the stable activity enhancement by carboxyl groups showed that the introduction of organic acid ligands which are stable against oxidation and able to control proton transfer can be a strategy to stably enhance the OER activity of Mn oxides.

In Chapter 3, the OER activity of Mn oxides was tried to be maximized by the introduction of structural distortion to the Mn oxide crystals themselves. It was expected that, because in Mn oxide NPs, whose ratio of the number of the surface atoms to the total atoms is large, there exist Mn atoms with non-degenerate electronic structures due to the distortion of ligand fields, and thus that Mn^{3+} can be generated at low potential. Mn oxide NPs with a diameter of approximately 10 nm have indeed been reported as the OER catalyst with the highest activity among the non-noble-metal-based materials reported so far.[29] However, the reason for the high activity and the reaction mechanism including Mn^{3+} generation was unclear. Therefore, *in-situ* electrochemical spectroscopic techniques were comprehensively applied to reveal the structure of the NPs and its potential-dependent changes, the potential for the generation of Mn^{3+}, and the reaction mechanism. The Mn oxide NPs synthesized by a hot injection method were monodisperse with a diameter of approximately 10 nm. First, *in-situ* electrochemical Raman spectroscopy was conducted without noble metal substrates for surface-enhanced Raman scattering (SERS), expecting that spectra can be obtained without SERS effect because the ratio of the number of the surface atoms to the total atoms is large in the case of NPs. As a result, reversible changes between Mn^{2+}, Mn^{3+}, and Mn^{4+} and resulting changes in the structure and vibration modes were clearly observed. The flexible valency changes were confirmed, and the number of transferred protons was measured by *in-situ*

electrochemical ultraviolet–visible (UV–vis) absorption and X-ray absorption spectroscopy (XAS). The results led to the proposal of the reaction mechanism with O–O bond formation, not charge accumulation, as the RDS. In other words, it was revealed that Mn^{3+} was specifically stabilized and the OER activity was drastically enhanced by decreasing the size of Mn oxides to NPs. The result of *in-situ* Raman spectroscopy demonstrated that the bonding structure in the NPs smoothly and reversibly changed depending on the potential. The asymmetry of the ligand field resulted from the dynamic changes in the bonding structure may be the reason for the stabilization of Mn^{3+}. The results showed that the dramatically higher OER activity than conventional Mn-based catalysts can be achieved by the stabilization of Mn^{3+} inside the Mn oxides which can accommodate structural distortion by smooth changes of the structure.

In Chapter 4, application of Mn oxide OER catalysts to PEM electrolyzers was investigated. In PEM electrolyzers, the catalysts are generally surrounded by sulfonic acid groups of PEMs,[20] which may enhance the OER activity of Mn oxides by controlling proton transfer. Six types of Mn oxides synthesized by industrial methods at Tosoh Corporation, a supplier of electrolytic Mn dioxides (EMDs) which is only in Japan and largest in the world, were evaluated in PEM electrolyzers and in acidic aqueous electrolyte. As a result, it was revealed that the Mn oxides can readily show a comparable OER activity to that of Pt/C in PEM electrolyzers. It is worth noting that Sugiyama and Fujii *et al.* demonstrated as high as 24.4% of solar-to-hydrogen (STH) energy conversion efficiency by using PEM electrolyzers with Pt/C as the OER catalyst.[30] Also, the activity trend was found to be different in PEM electrolyzers and in acidic aqueous electrolytes. The results demonstrated that Mn oxides are promising OER catalysts for PEM electrolyzers to achieve high STH energy conversion efficiency without using noble metal components, and importance of the evaluation of OER catalysts in PEM electrolyzers.

In Chapter 5, conclusions are summarized, and the perspective from this study is presented.

1.3 Introduction of Conversion of Renewable Energy to Chemical Fuels

The fixation of energy from sunlight as chemical energy is conducted by photosynthesis in Nature. The most general type of photosynthesis is oxygenic photosynthesis, where the electrons extracted from water are used for fixation of carbon dioxide as organic compounds, obviously providing a blueprint for sustainable energy conversion systems from renewable energy to chemical energy using water as the electron source. In this Section, the general introduction of natural photosynthesis, especially about the Mn_4 cluster in PSII, the OER as a multi-electron transfer reaction, and the catalysts for the OER is summarized.

1.3.1 Natural Photosynthesis

1.3.1.1 General Scheme of Natural Oxygenic Photosynthesis

Photosynthesis is a process conducted by a variety of organisms including plants, algae, and cyanobacteria where light energy is converted and fixed as chemical energy. Although there are several types of anoxygenic photosynthesis, where substances other than water such as sulfide ions are used as the electron donor, oxygenic photosynthesis, where water serves as the electron donor and oxygen is produced, is the most common type of photosynthesis and the word photosynthesis in the narrow sense means this type. The evolution of oxygenic photosynthetic organisms drastically increased the concentration of oxygen in the atmosphere on the Earth and completely changed the ecosystem (oxygen catastrophe).[19,31] Here, the general principle of oxygenic photosynthesis is briefly summarized (Figure 1.1).[32]

The light-dependent reactions of the oxygenic photosynthesis proceed at the thylakoid membrane of the chloroplast, where redox-active proteins and molecules are embedded. They include protein complexes photosystem I (PSI), PSII, and cytochrome b_6f complex, the former

two of which absorb light. There are plastoquinones (PQs) between PSII and cytochrome b_6f complex, and plastocyanin (PC) between cytochrome b_6f complex and PSI. The reaction centers of PSI and PSII are denoted as P_{700} and P_{680}, respectively, based on the wavelength of maximum light absorption. The reactions start from light-induced charge separation at P_{680}, which subsequently donates an electron to pheophytin followed further transfer to a PQ, and extracts an electron from redox-active tyrosine-161 in the D1 subunit of PSII (D1-Tyr161) called as tyrosine Z (Y_Z). Y_Z oxidizes the Mn_4 cluster, the reaction site for the OER. During the oxidation of one water molecule, four protons are released to the lumen. The reaction mechanism around the Mn_4 cluster will be later summarized more in detail (Section 1.3.1.2). The electron transferred to the PQ is subsequently transferred to PSI *via* another PQ, cytochrome b_6f complex, and a PC, during which protons are transported from stroma to lumen. The proton concentration gradient generated by this transfer process and the OER is used by the adenosine triphosphate (ATP) synthase to synthesize ATP. The electron donated to PSI is excited again at P_{700} and used for the reduction of nicotinamide adenine dinucleotide phosphate (NADP) to NADPH. The generated NADPH and ATP are used for the fixation of carbon dioxide to synthesize organic compounds in Calvin cycle.

The conversion of carbon dioxide to organic compounds is reduction reactions. Thus, it is required to oxidize an electron donor to obtain electrons to proceed the reactions. It was water that cyanobacteria, the first oxygenic photosynthetic organism, adopted as the electron donor. Again, water is by far the most abundant electron source on the Earth. The development of a method to utilize water is regarded as a significant factor which led to the prosperity of photosynthetic organisms. The reaction site for the OER is the Mn_4 cluster in PSII, which can be a blueprint for artificial OER catalysts in the sense of activity, stability, and non-usage of noble metal elements. The structure, thermodynamics, and reaction mechanism at and around the Mn_4 cluster are herein briefly summarized.

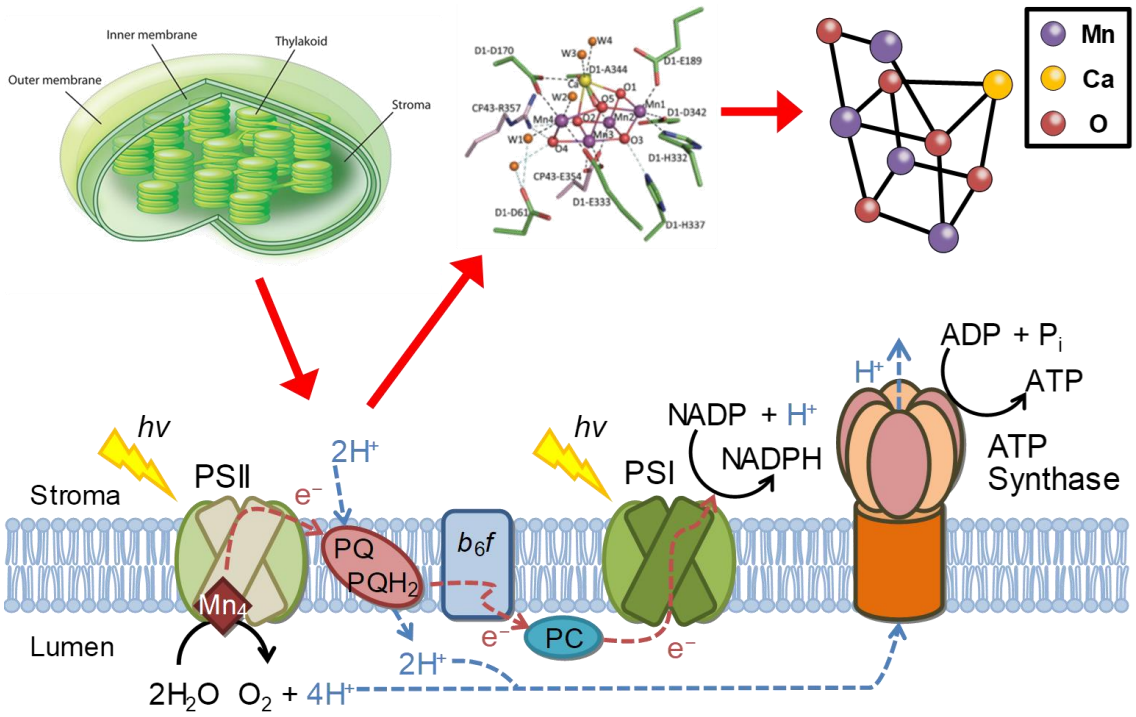

Figure 1.1 | Overview of photochemical reactions at thylakoid membranes (Chloroplast: reprinted from ref. 33. Copyright 2010 Nature Education. The Mn_4 cluster and the surrounding molecules: reprinted by permission from ref. 25. Copyright 2011 Macmillan Publishers Limited).

1.3.1.2 The Mn_4 Cluster in Photosystem II and Surrounding Molecules

The Structure of PSII at Dark-Stable S_1 State

PSII is a membrane-protein complex which consists of 20 subunits with the mass in total for a monomer of 350 kDa.[25] The OER proceeds *via* a reaction cycle called Kok cycle. Kok *et al.* demonstrated that, after four light flashes and resulting accumulation of four oxidizing equivalents, the OER proceeds.[34] The states in Kok cycle are denoted as S_i (i = 0–4), where oxygen evolves during the transition from S_3 to S_0 *via* S_4. The structure of PSII, especially the reaction center for the OER, had been elusive because of the difficulty in crystallization and low resolution. In 2011, Kamiya and Shen *et al.* demonstrated the structure of PSII at dark-stable S_1 state at 1.9 Å resolution by X-ray diffraction (XRD) analysis using synchrotron radiation.[25] The result

demonstrated for the first time that the reaction center for the OER in PSII at S_1 state is a Mn_4CaO_5 cluster surrounded by a well-defined environment of water molecules and amino-acid residues. To avoid the possible reduction of Mn cations by X-ray irradiation, Shen *et al.* minimized the X-ray damage by using femtosecond pulses of X-ray free electron lasers (XFEL) and reported a structure at 1.95 Å resolution in 2014.[35] While those measurements were conducted at 100 K, Young *et al.* reported the structure measured by XFEL at room temperature.[36]

Because the structure and the surrounding environment of the Mn_4 cluster were basically already demonstrated except for the small possible deviation of bond lengths or positions of atoms, the structure at S_1 state demonstrated by Kamiya and Shen *et al.* in 2011 is shown in Figure 1.2a.[25] A schematic image to clearly show the structure is shown as Figure 1.2b. In Figure 1.2a and b, coordination bonds are shown as black broken lines, and hydrogen bonds are shown as broken blue lines in Figure 1.2a and dotted black lines in Figure 1.2b, respectively. There are seven direct ligands *via* coordination bonds to the Mn_4 cluster: D1-Glu333, CP43-Glu354, D1-Glu189, D1-Asp342, D1-Ala344, D1-Asp170, and D1-His332. D1-His337 and CP43-Arg357 are hydrogen-bonded with the Mn_4 cluster. D1-Asp61 constitutes an outer-sphere complex *via* water molecules to the Mn_4 cluster. Here, D1 and CP43 are protein subunits of PSII; Glu, Asp, Ala, His, are Arg are standard three-letter abbreviations of amino acids of glutamate, aspartate, alanine, histidine, and arginine; three-letter abbreviations of amino acids are not included in List of Abbreviation of this dissertation).

The bond lengths of the Mn_4 cluster reported by Shen *et al.* in 2014 are shown in Figure 1.2c.[35] The structure is called as “distorted chair” structure,[25] and there are Mn–O bonds with various lengths, within the range from 1.8 Å to as long as 2.7 Å. This contrasts with general inorganic Mn oxide crystals with a limited variety of Mn–O bond lengths which are far shorter than 2.7 Å. For example, studies about experimental determination of the structure of β-MnO_2 samples reported

that the lengths of Mn–O bonds are in the narrow range from 1.879 to 1.8981 Å.[37,38]

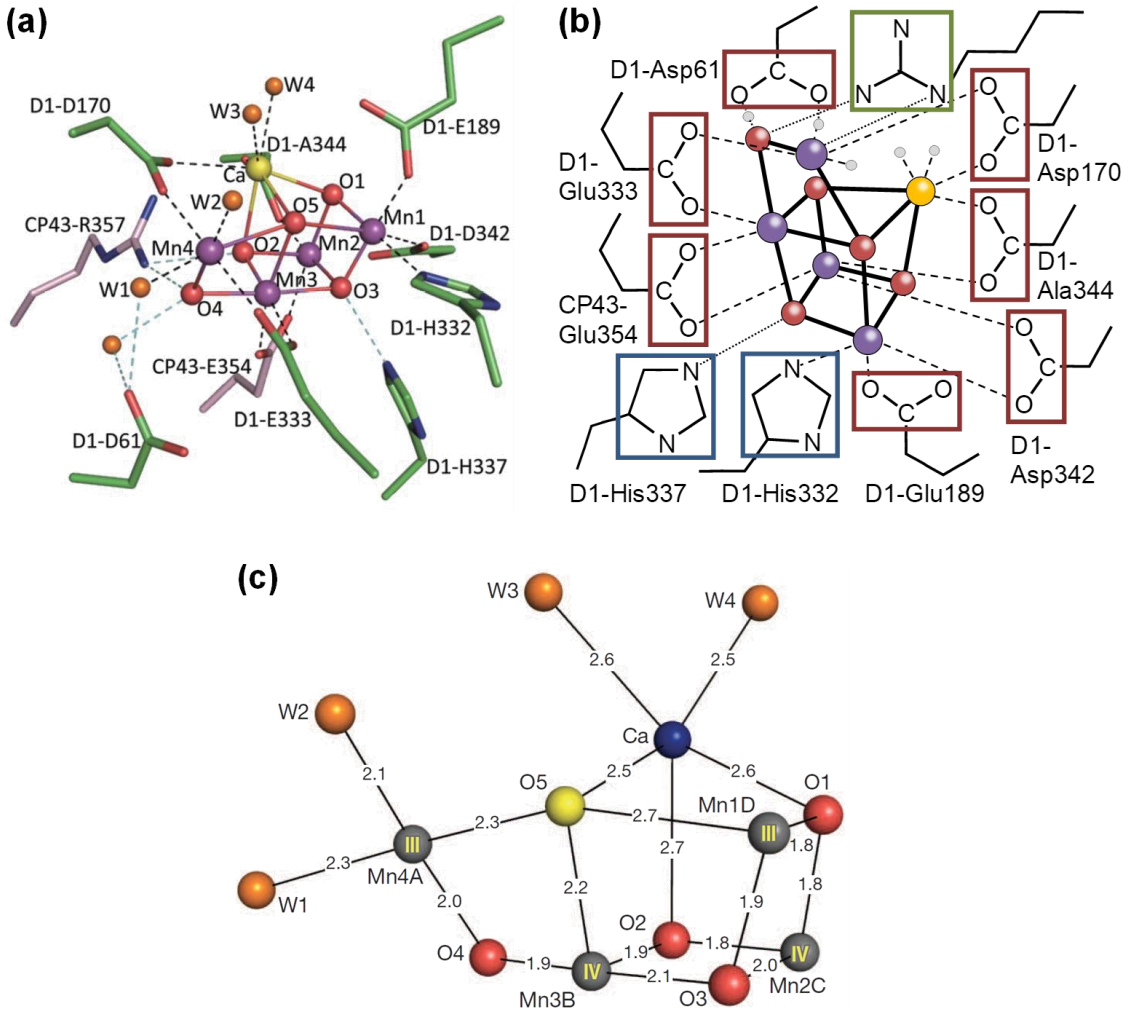

Figure 1.2 | (a) Structure of the Mn_4 cluster and its ligand environment revealed by Umena *et al.* (Reprinted by permission from ref. 25. Copyright 2011 Macmillan Publishers Limited.) and (b) its schematic image modified for the clarity. In (b), water is shown as gray circles. (c) Structure of the Mn_4 cluster with Mn–O, Ca–O, Mn–water, and Ca–water distance values (in Å). Reprinted by permission from ref. 35. Copyright 2015 Macmillan Publishers Limited.

The static structure analysis also revealed hydrogen-bond networks around the Mn_4 cluster, which can be the pathways for proton transport to the lumen. For example, the 1.9-Å structure reported by Kamiya and Shen *et al.* revealed a hydrogen-bond network starting from O4 (As for the numbering, see Figure 1.2a and c.) to the lumenal bulk phase.[25] Saito, Rutherford, and Ishikita demonstrated using a quantum mechanics/molecular mechanics (QM/MM) method that this network serves as a transport chain for the proton extracted during the changes from S_0 to S_1 state from the Mn_4 cluster to lumen (Figure 1.3).[39]

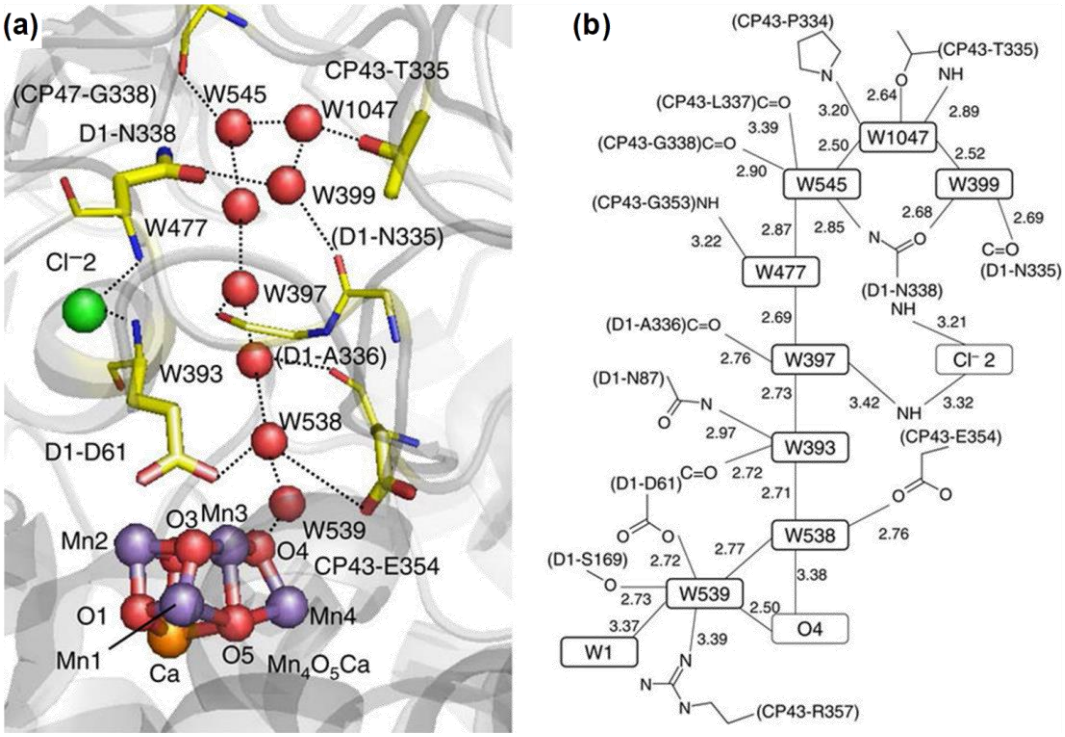

Figure 1.3 | (a) The structure of hydrogen-bond network around the Mn_4 cluster revealed by Umena *et al.*,[25] which was demonstrated to be a transport chain for the proton to lumen by Ishikita *et al.*[39] (b) The distances of hydrogen bonds in the network in Å. Adapted from ref. 39.

Kok Cycle: Mn Valency and Proton-Coupled Electron Transfer

The reaction cycle of PSII is called as Kok cycle, as previously explained. The changes in the bonding structure and electronic structure during Kok cycle have been investigated both experimentally and theoretically. Representative experimental methods for the analysis of the reaction mechanism include XRD,[25,35,36] extended X-ray absorption fine structure (EXAFS),[19,40] X-ray emission spectroscopy (XES), resonant inelastic X-ray scattering spectroscopy (RIXS),[19] Fourier-transform IR (FT-IR) spectroscopy,[41,42] electron paramagnetic resonance (EPR), and electron nuclear double resonance (ENDOR).[43] Computational methods such as density functional theory (DFT)[44] and QM/MM[39] have been powerful for the analysis of the reaction cycle. This dissertation does not summarize the full detail of the current understanding of the reaction cycle about which the discussion has not been settled, but the emphasis will be put on the valency changes of the Mn_4 cluster and the possible roles of proton-coupled electron transfer (PCET) during the reaction cycle. Representative reviews are also herein referred.[19,45–49]

As for the Mn valency of the Mn_4 cluster during Kok cycle, EPR and ENDOR studies strongly suggested that the formal oxidation state of Mn in the S_0, S_1, and S_2 states are (III, III, III, IV), (III, III, IV, IV), and (III, IV, IV, IV), respectively.[50,51] It is, however, to be noted that there are also supporters of a low-valent paradigm, where the valency of Mn in the S_0, S_1, and S_2 states are (II, III, III, III), (III, III, III, III), and (III, III, III, IV), respectively.[52,53] As for the changes from the S_2 to S_3 state, there has been a discussion about whether the oxidation is Mn-centered[54,55] or ligand-centered.[56] The bonding structure and electronic structure of the S_4 state, which is immediately before the OER, are a target for extensive discussion (Figure 1.4). In fact, it also remains uncertain whether the histidine directly coordinated to the Mn_4 cluster, D1-His332 (Figure 1.2a and b), is subject to one-electron oxidation to a transient radical during Kok cycle.[19,45,57–62] The formal oxidation states of Mn during Kok cycle have not been determined as

seen above. However, it is noted that, in all cases, the trivalent Mn exists during the reaction cycle without dissipation of oxidizing equivalent before the OER, in contrast to the disproportionation of Mn^{3+} in artificial systems at neutral pH ($2Mn^{3+} \rightarrow Mn^{2+} + Mn^{4+}$).

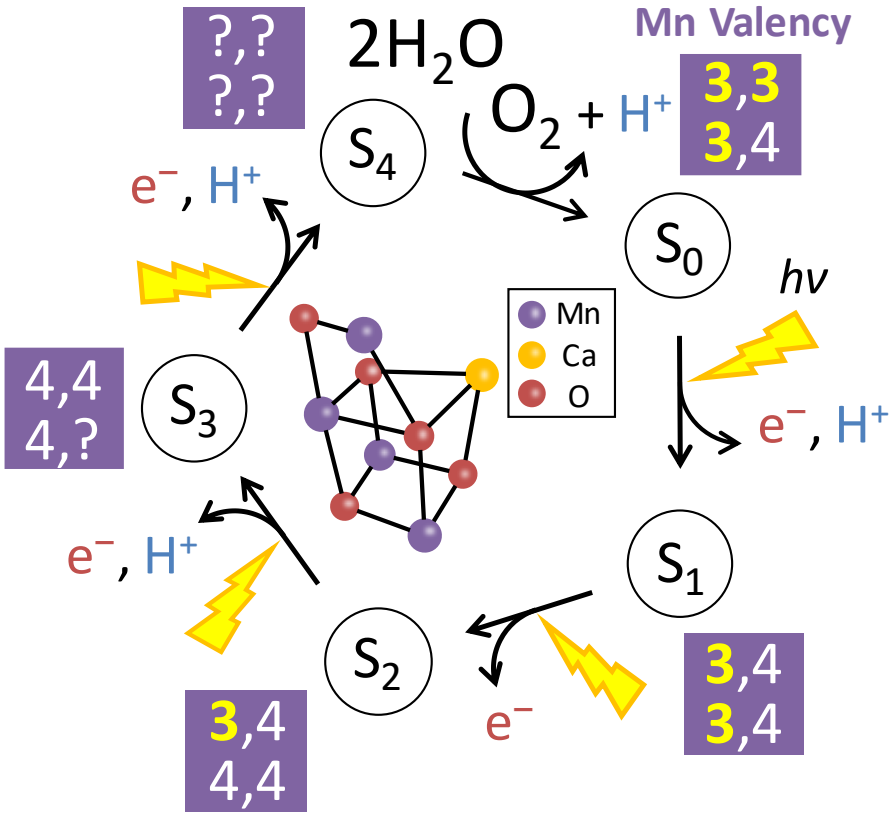

Figure 1.4 | The structure of the Mn_4 cluster[25] and Mn valency during Kok cycle.

During the OER in Kok cycle, four protons need to be removed and transported to the lumen. It was strongly suggested by the Frost diagram of the Mn_4 cluster comparing with those of hypothetical Mn tetramer without PCET (Figure 1.5) that, during Kok cycle proceeds proton transfer from the Mn_4 cluster coupled with the oxidation of the cluster, namely, PCET.[27] The involvement of PCET in Kok cycle can prevent the charge buildup. For example, PCET with D1-

Asp61 as the proton acceptor during the step from S_0 to S_1 state was proposed (Figure 1.6).[28] The coordination structure of D1-Asp61 to the Mn_4 cluster, an outer-complex *via* water molecules (Figure 1.2a and b), is a suitable configuration for D1-Asp61 to accept a proton. D1-Asp61 was also proposed to function as the starting point of a proton exit pathway. [28] It is also noted in passing that the oxidation of Y_Z by P_{680}^+ is also coupled with proton transfer to D1-His190. PCET is utilized at multiple timing and places in Kok cycle to minimize the energy loss.[28]

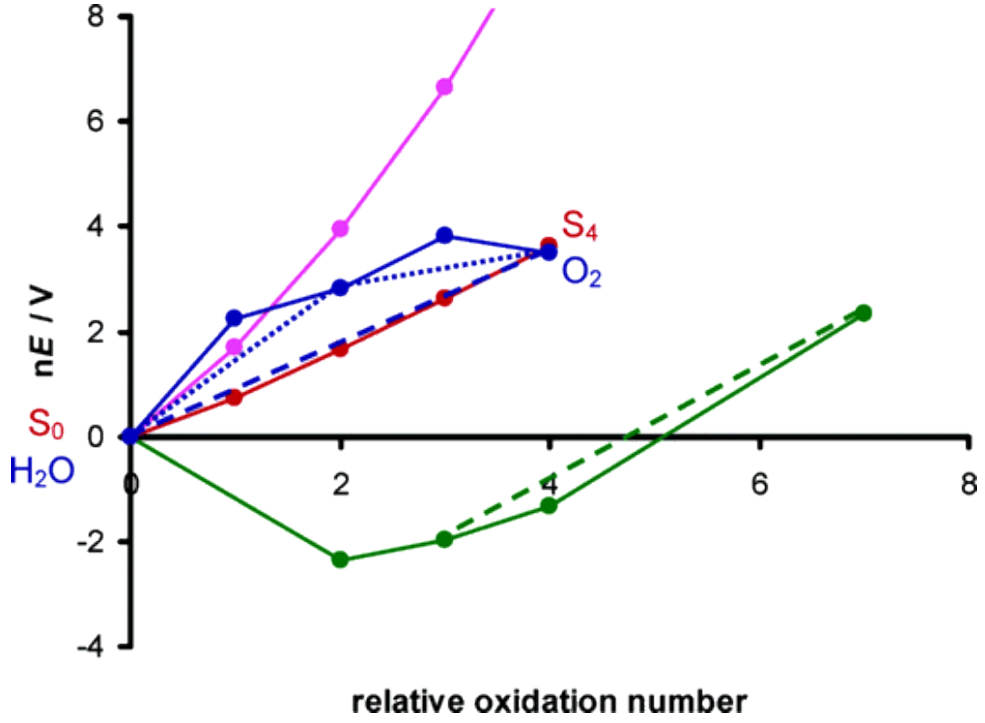

Figure 1.5 | Frost diagram of four species: the Mn_4 cluster in red (pH = 6, referenced to S_0), a single manganese ion[63] in green (pH = 6, referenced to Mn^0), a hypothetical manganese tetramer, without PCET, in magenta (referenced to $Mn^{3+}{}_3Mn^{4+}$), and oxygen[63–65] in blue (pH = 6, referenced to $2H_2O$; the species with relative oxidation number of 0, 1, 2, 3, and 4 are $2H_2O$, $H_2O + OH^{\bullet}$, H_2O_2, $O_2^{-\bullet}$, and O_2, respectively. All potentials are given versus standard hydrogen electrode (SHE). Reprinted with permission from ref. 27. Copyright 2006 American Chemical Society.

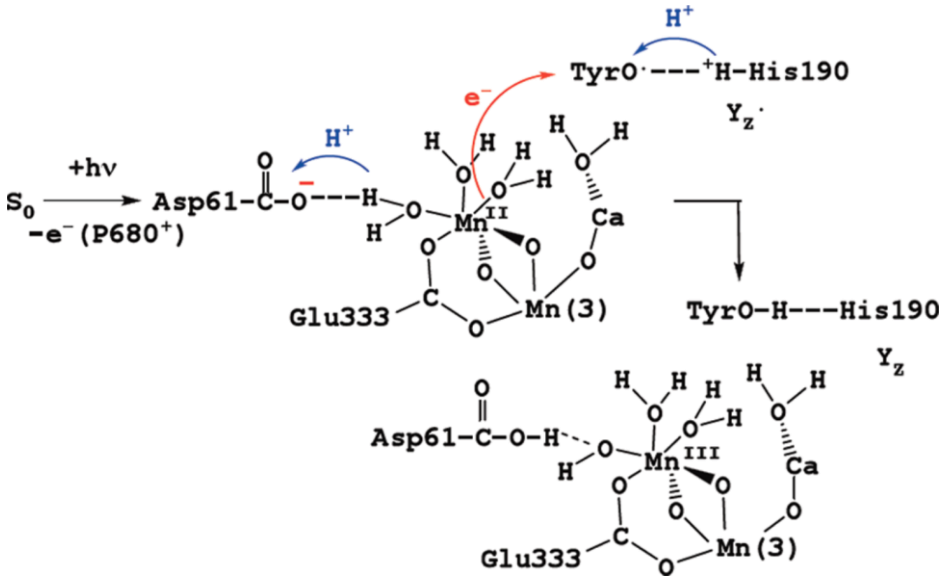

Figure 1.6 | The proposed PCET during the oxidation of Mn^{2+}–OH_2 in the Mn_4 cluster to Mn^{3+}–OH in the step from S_0 to S_1 state in Kok cycle. Reprinted with permission from ref. 28. Copyright 2012 American Chemical Society.

Thermodynamics: Overpotential for the OER

The redox potential of the redox-active molecules in PSII has been measured by chemical or electrochemical redox titration in combination with spectroscopy,[66,67] as well as calculation.[68] From the results, the overpotential for the OER by PSII can be estimated. Reduction of the primary PQ electron acceptor, Q_A, can be relatively easily monitored by fluorescence.[66] Thus, Q_A is a feasible target for the redox titration.[67] The potential of Q_B, the secondary PQ electron acceptor, was recently measured by Noguchi *et al.* by FT-IR spectroelectrochemistry.[67] The redox potential thus experimentally measured can be used for the anchoring point for the determination of redox potential of other molecules based on free-energy changes during electron transfer, which can be determined from the yield and rate of the electron transfer.[69] From the results, the energy diagram can be depicted (Figure 1.7). The overpotential for the Mn_4 cluster for the OER (the difference between the redox potential of the Mn_4 cluster and Y_Z) can be calculated to be ~300 mV.[69]

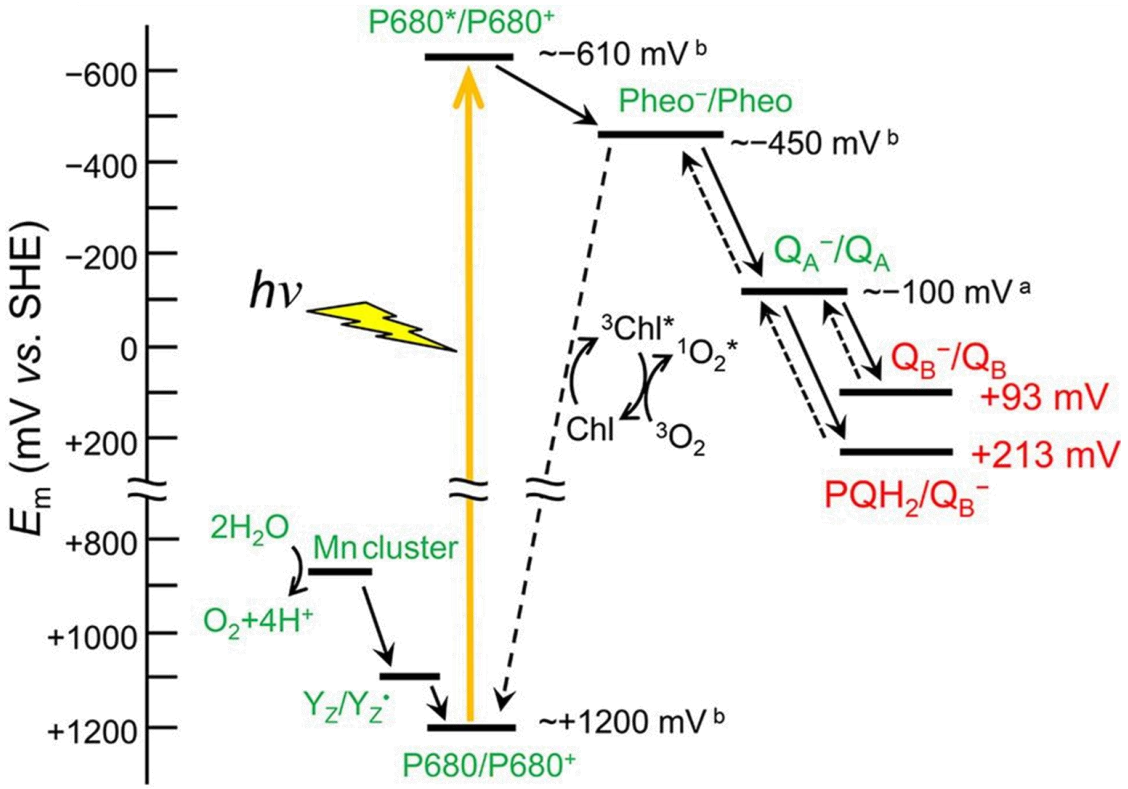

Figure 1.7 | Diagram of the potential of redox-active components in PSII. Reprinted from ref. 67. Copyright 2016 National Academy of Sciences.

Surrounding Molecules Around the Mn_4 Cluster: Proton Transfer and Effect of Point Mutation

The surrounding molecules around the Mn_4 cluster are essential for its activity. As mentioned above, the surrounding water and amino-acid residues comprise hydrogen-bond networks which can transfer protons away from the Mn_4 cluster to the lumen. Also, point mutation of any of the surrounding amino-acid residues drastically decreases the activity.[70–73]

1.3.2 Oxygen Evolution *via* Water Oxidation by Artificial Catalysts

As described above, the natural oxygenic photosynthesis utilizes the Mn_4 cluster as the oxygen evolution center. Thus, it is natural to regard Mn-based materials as the candidates for OER catalysts. The activity and stability of Mn-based OER catalysts need to be improved to rival the Mn_4 cluster or noble metal catalysts. The overpotential for the OER by the Mn_4 cluster is ~300 mV, as described above, and the maximum TON is ~10^3 s^{-1}.[74]

In this Section, the OER and multi-electron transfer reaction in general, the OER catalysts, and Mn-based OER catalysts are reviewed.

1.3.2.1 Water Oxidation Catalysts for Conversion Systems of Renewable Energy to Chemical Fuels

The OER by water oxidation is a multi-electron transfer reaction which requires four-electron and four-proton transfer (Equation 1.1).

$$2H_2O \rightarrow O_2 + 4\ e^- + 4\ H^+ \quad (E^\circ = +1.23\ \text{V vs. SHE}) \tag{1.1}$$

Multi-electron transfer reactions are the reactions where multiple electrons are transferred in one time, and, compared to one-electron transfer reactions, their standard thermodynamic potential is usually less anodic in the case of anodic reactions and less cathodic in the case of cathodic reactions. The standard potentials for carbon dioxide reduction reactions[75] and water oxidation reactions[76,77] are summarized in Table 1.1. For example, the standard potential for eight-electron reduction of carbon dioxide to methane is −0.24 V vs. SHE, which is far less negative than that for one-electron reduction, −1.9 V vs. SHE.

Table 1.1 | Standard potentials for carbon dioxide reduction[75] and water oxidation reactions[76,77]

Potential / V vs. SHE (at pH 7)	
−1.9	$CO_2 + e^- \longrightarrow CO_2^{\bullet -}$
−0.61	$CO_2 + 2H^+ + 2e^- \longrightarrow HCO_2H$
−0.53	$CO_2 + 2H^+ + 2e^- \longrightarrow CO + H_2O$
−0.48	$CO_2 + 4H^+ + 4e^- \longrightarrow HCHO + H_2O$
−0.38	$CO_2 + 6H^+ + 6e^- \longrightarrow CH_3OH + H_2O$
−0.24	$CO_2 + 8H^+ + 8e^- \longrightarrow CH_4 + 2H_2O$

Potential / V vs. SHE (at pH 0)	
2.65	$H_2O \longrightarrow OH + H^+ + e^-$
1.776	$2H_2O \longrightarrow H_2O_2 + 2H^+ + 2e^-$
1.229	$2H_2O \longrightarrow O_2 + 4H^+ + 4e^-$

While standard potentials for multi-electron transfer reactions are less demanding compared to those of one-electron transfer reactions, the investigation of the active catalysts for multi-electron transfer reactions with small overpotential tends to be more demanding than those for one-electron transfer reactions because of the existence of multiple intermediates, whose energy should be optimized. It is also to be noted that, in organisms, not only the OER and carbon dioxide fixation but also the oxygen reduction reaction (ORR),[78,79] nitrogen fixation,[80,81] sulfate reduction,[81,82] nitrate reduction,[83] and the hydrogen evolution reaction (HER)[84] proceed as multi-electron transfer reactions and play important roles in their metabolism. The development of the catalysts for multi-electron transfer reactions has been a challenge for the establishment of a society with sustainable material and energy cycles.

Especially, the OER needs to be efficiently catalyzed if one aims to construct an efficient system to convert renewable energy to chemical fuels using water as the electron source, as already mentioned. Water electrolyzers are one of the representative components of the energy conversion systems from renewable energy to chemical fuels, which can be connected to

renewable-power-generating facilities such as photovoltaics (PVs) or wind turbines either directly or *via* electricity grid. As for the systems for "direct" conversion of solar energy to chemical fuels, several types have been proposed in a series from PV-electrolyzers (electrolyzers connected to PVs) to self-standing photoelectrodes without external grids (Figure 1.8a)[85] or photocatalysts.[86] There is also increasing interest in these types of systems with microbes which can fix carbon dioxide utilizing hydrogen generated on cathodes or directly extracting electrons from cathodes (Figure 1.8b).[87] In all kinds of systems summarized above, the overpotential for the OER can be a bottleneck for the energy conversion efficiency.

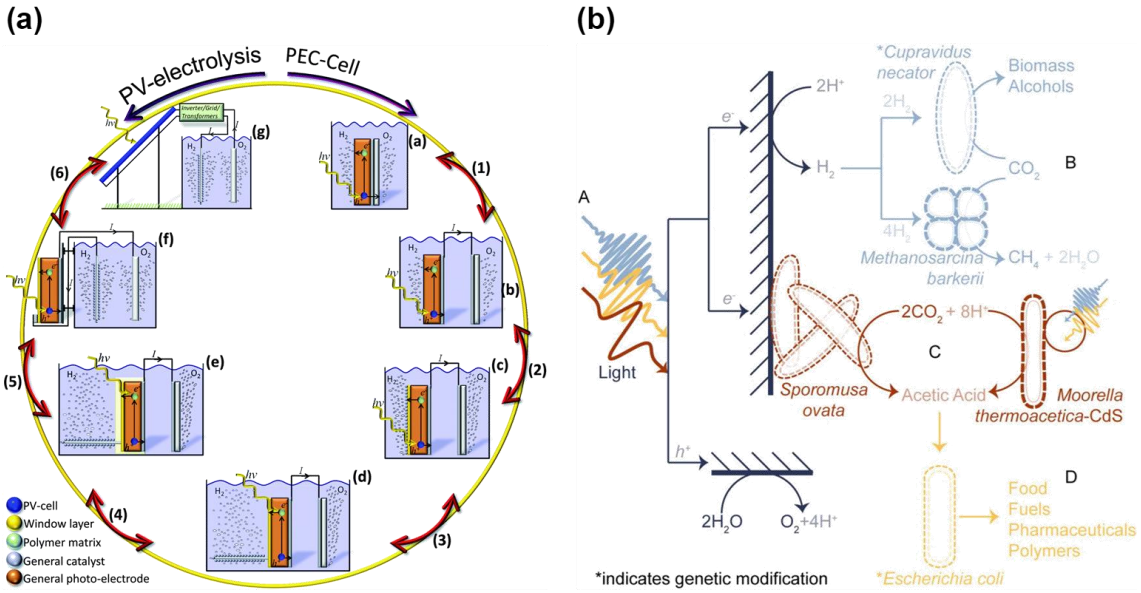

Figure 1.8 | (a) Illustration of seven types of systems for "direct" conversion of solar energy to chemical fuel in a series from PV-electrolyzers (electrolyzers connected to PVs) to photoelectrochemical (PEC) cells with self-standing photoelectrodes without external grids. Reproduced from ref. 85 with permission from The Royal Society of Chemistry. (b) Overview of photosynthetic biohybrid systems, where microbes use hydrogen gas generated on or electrons from (photo)cathodes for the fixation of carbon dioxide. Reprinted with permission from ref. 87. Copyright 2017 American Chemical Society.

The catalysts for the OER can be divided into two types: complex molecules and heterogeneous inorganic materials. Heterogeneous inorganic OER catalysts are represented by metal oxides; others include metal chalcogenides, metal pnictides, and non-metal compounds such as nitrogen-doped carbon materials.[88,89] One of the advantages of complex catalysts is that the electronic structure can be tuned by the kind and the position of substituent groups. There are, however, problems of the metal complex catalysts to be solved in addition to the problems in activity, including the cost for the production of catalysts and generally low robustness originating from the usage of organic ligands. The heterogeneous inorganic OER catalysts other than metal oxides can also suffer problems regarding oxidative decomposition. In the case of metal chalcogenide and pnictide OER catalysts, numerous reports have even suggested that a thin oxide layer formed in anodic conditions catalyzes the OER while the original materials serve as conducting supports.[88] For the development of energy conversion systems which can be used on a large scale in industry, it is thus natural to consider metal oxides the most promising candidates for the OER catalysts. From here, the focus is put on metal-oxide-based OER catalysts.

The development of OER catalysts has been conducted by experimental trial-and-error-based approaches, theory-based approaches, and the combination of both. Here, representative OER catalysts and theories developed so far and existing challenges are overviewed. Then, the focus will be put on Mn-oxide-based catalysts.

1.3.2.2 Metal-Oxide-Based Water Oxidation Electrocatalysts

Noble-Metal-Based Catalysts

After the report of RuO_2 on titanium catalyzing the OER at the overpotential of 200 mV by Trasatti and Buzzanca in 1971,[90] Ru-based catalysts have attracted attention as OER catalysts.

Colloidal or solid RuO_2-based materials were reported as efficient OER catalysts.[91,92] These materials, however, dissolved in anodic conditions at high potential. On the other hand, Ir oxides are also one of the most efficient OER catalysts and furthermore was demonstrated to be more stable than Ru oxides.[91–93] Among them, an Ir oxide electrode synthesized by electrodeposition was reported by Mallouk *et al.* in 2011 demonstrating its activity for the OER with the current density of 1.5 mA cm^{-2} at the overpotential of 200 mV, over a wide pH range (Figure 1.9a).[94] Recent examples of OER catalysts with the highest activity in acidic pH include $IrO_x/SrIrO_3$ reported by Jaramillo *et al.* (Figure 1.9b)[95] and Ir double perovskites reported by Koper *et al*.[96]

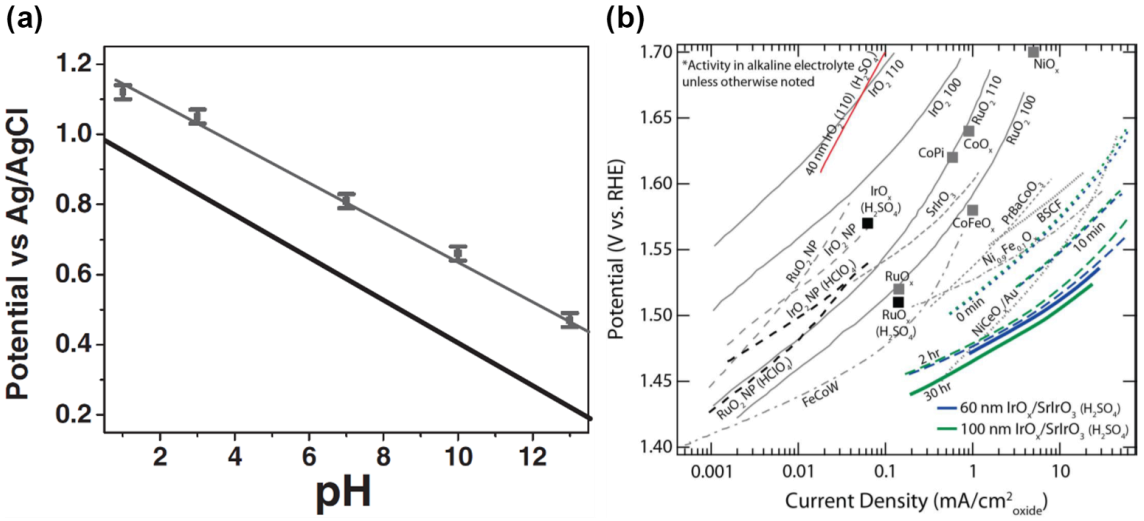

Figure 1.9 | (a) pH dependence of the average overpotential taken from the initiation of the OER at 1.5 mA cm^{-2} and 1 mA cm^{-2} on $IrO_x \cdot nH_2O$ NP films deposited on glassy carbon and gold (Au) electrodes, respectively, reported by Mallouk *et al.* The standard potential for the OER is also shown as the black line. Adapted with permission from ref. 94. Copyright 2011 Wiley-VCH Verlag GmbH & Co. KGaA, Weinheim. (b) Tafel plots comparing the current density from OER catalysts in acidic and alkaline electrolyte. From ref. 95. Reprinted with permission from AAAS.

Non-Noble-Metal-Based Catalysts (Other Than Mn-Based Ones)

There have been numerous reports of non-noble-metal-oxide-based materials with comparable OER activity to noble-metal-based catalysts at alkaline pH, which typically contain Ni, Co, or both.[14,97] A representative example is Ni–Fe oxides. Using a Ni–Fe oxide, the overpotential as small as 30 mV to achieve 1 mA cm^{-2} per projected area in 1 M KOH was reported by Merrill and Dougherty.[98] A Ni–Fe layered double hydroxide was adopted as the catalyst for both the OER and the HER at alkaline pH to achieve the STH energy conversion efficiency of 12.3% using an electrolyzer without noble metal catalysts and a perovskite solar cell.[99] Another group of materials actively investigated as OER catalysts is perovskite materials, whose flexible choice of constituent elements allows rational design (the developed theory is reviewed later). For example, Shao-Horn *et al.* reported based on a theoretical approach that $Ba_{0.5}Sr_{0.5}Co_{0.8}Fe_{0.2}O_{3-\delta}$ is an active OER catalyst with the overpotential of ~250 mV at 50 μA cm^{-2} per the surface area of the catalyst in 0.1 M KOH.[100]

In non-alkaline pH conditions, non-noble-metal-based OER catalysts with comparable activity to noble-metal-based catalysts have not been established.[14,29] In 2008, Nocera *et al.* reported the formation of a Co-based catalyst during the application of anodic potential on indium tin oxide (ITO) electrodes in a neutral solution containing Co^{2+} and phosphate ions, which exhibited the OER activity with the overpotential of 280 mV at 1.0 mA cm^{-2} at pH 7.0.[101] This report garnered attention to the OER catalysis in neutral ambient conditions and also pointed renewed attention to the studies from the early 1980s about Co oxides and soluble Co aqua or hydroxyl complexes as homogeneous[102] or heterogeneous[103] catalysts for the OER. The catalyst attracted attention also due to the self-healing property based on the electrodeposition of Co ions dissolved during the OER. After this report, the OER activity of metal oxides containing Co, Ni, Fe, or some of them was evaluated in neutral conditions.[104–108] The investigation regarding Mn-oxide-based catalysts

is reviewed in Section 1.3.2.4; the non-noble-metal-based OER catalysts which can function in acidic conditions are summarized in Section 4.1. Although the investigation so far has revealed non-noble-metal-oxide-based OER catalysts with high activity, as is evident when the activity is compared with the results shown in Figure 1.10, the activity still needs to be improved to rival that of noble-metal-based catalysts.

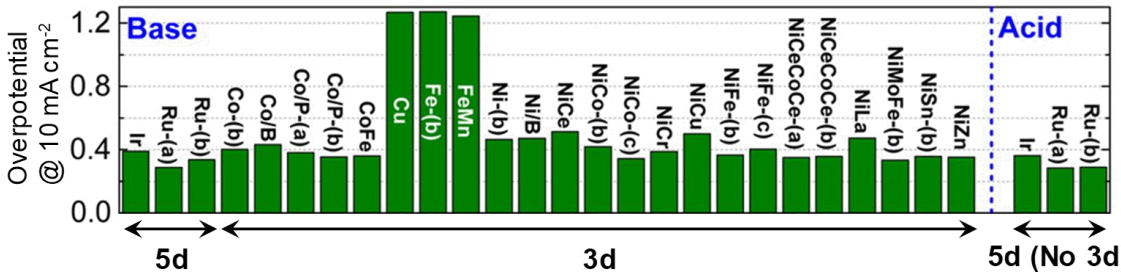

Figure 1.10 | Summary of the overpotential for the OER by various catalysts at the current density of 10 mA cm^{-2} per geometric area after the electrolysis for 2 hours. Adapted with permission from ref. 14. Copyright 2015 American Chemical Society.

1.3.2.3 Theoretical Approaches for Metal-Oxide-Based Water Oxidation Electrocatalysts

Theories to explain or predict the activity of OER catalysts have also been developed, allowing rational development of novel catalysts. A widely-conducted approach is based on DFT calculation of the energy of intermediate species, assuming a certain reaction mechanism. Another approach correlates a physical property, such as the number of electrons in a specific orbital or the enthalpy of transition from a lower to a higher oxidation state, to the activity.

There are two mechanisms of the OER which have mainly been considered: the acid–base and direct-coupling mechanisms. Elementary steps of each mechanism are as follows:

Acid–base mechanism

$$H_2O\ (l) + * \rightarrow HO* + H^+ + e^- \quad (1.2)$$

$$HO* \rightarrow O* + H^+ + e^- \quad (1.3)$$

$$O* + H_2O\ (l) \rightarrow HOO* + H^+ + e^- \quad (1.4)$$

$$HOO* \rightarrow * + O_2\ (g) + H^+ + e^- \quad (1.5)$$

Direct-coupling mechanism

$$2H_2O\ (l) \rightarrow 2HO* + 2H^+ + 2e^- \quad (1.6)$$

$$2HO* \rightarrow 2O* + 2H^+ + 2e^- \quad (1.7)$$

$$2O* \rightarrow *OO* \quad (1.8)$$

$$*OO* \rightarrow O_2\ (g) \quad (1.9)$$

Here, * denotes a surface site, and the notation in acidic conditions is used. For both mechanisms, the energy of the intermediates can be calculated.

The theoretical investigation based on the acid–base mechanism has been vigorously explored by Nørskov and Rossmeisl *et al.*,[4,109] who successfully correlated the result of DFT calculation of each step with the activity of OER catalysts. Theoretical overpotential can be calculated where all steps (Equation 1.2–1.5) become thermodynamically downhill. The Gibbs free energy changes of each step can be expressed as follows:[109]

$$\Delta G_1 = \Delta G_{HO*} - \Delta G_{H_2O(l)} - eU + k_b T \ln a_{H^+} \quad (1.10)$$

$$\Delta G_2 = \Delta G_{O*} - \Delta G_{HO*} - eU + k_b T \ln a_{H^+} \quad (1.11)$$

$$\Delta G_3 = \Delta G_{HOO*} - \Delta G_{O*} - eU + k_b T \ln a_{H^+} \quad (1.12)$$

$$\Delta G_4 = \Delta G_{O_2} - \Delta G_{HOO*} - eU + k_b T \ln a_{H^+} \quad (1.13)$$

where ΔG_X is the Gibbs free energy of adsorption of X; e is an elementary charge, U is the electrode potential versus SHE; k_b is Boltzmann constant; T is temperature; a_{H^+} is the activity of proton. Therefore, the amount of change of ΔG_{1-4} depending on the potential is the same. In the case of the ideal catalyst, ΔG_{1-4} equals 1.23 eV at zero potential (U = 0) because, as can be noted by the standard potential for the OER, the Gibbs free energy of water and oxygen are the same at 1.23 V vs. SHE. In this case, the OER proceeds without overpotential (Figure 1.11).

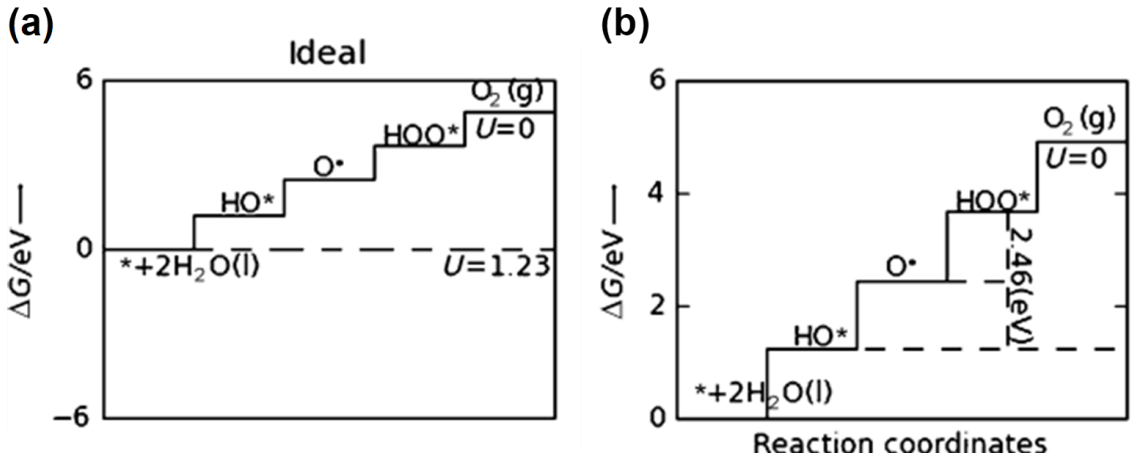

Figure 1.11 | (a) The diagram of standard free energy for the OER at zero potential (U = 0) and equilibrium potential for the OER (U = 1.23) in the case of the ideal catalyst. (b) Expansion of (a) showing that $\Delta G_{HOO^*} - \Delta G_{HO^*}$ = 2.46 eV. Adapted with permission from ref. 109. Copyright 2011 Wiley-VCH Verlag GmbH & Co. KGaA, Weinheim.

However, scaling relationships exist between the adsorption energy of surface species. Koper pointed out that ΔG_{HO^*} and ΔG_{HOO^*} are correlated with a constant difference of 3.2 eV, which is different from the ideal value of 2.46 eV (1.23 eV × 2).[110] With this relationship, the magnitude of the potential-determining step for the OER, G^{OER}, becomes as follows:

$$G^{\mathrm{OER}} = \max\left[\Delta G_1, \Delta G_2, \Delta G_3, \Delta G_4\right] \quad (1.14)$$

$$= \max\left[\Delta G_2, \Delta G_3\right] \quad (1.15)$$

$$= \max\left[(\Delta G_{\mathrm{O}*} - \Delta G_{\mathrm{HO}*}), (\Delta G_{\mathrm{HOO}*} - \Delta G_{\mathrm{O}*})\right] \quad (1.16)$$

$$\approx \max\left[(\Delta G_{\mathrm{O}*} - \Delta G_{\mathrm{HO}*}), 3.2\ \mathrm{eV} - (\Delta G_{\mathrm{O}*} - \Delta G_{\mathrm{HO}*})\right] \quad (1.17)$$

Thus, $\Delta G_{\mathrm{O}*} - \Delta G_{\mathrm{HO}*}$ is a universal descriptor for the OER. Figure 1.12a and b show the relationship between $\Delta G_{\mathrm{O}*} - \Delta G_{\mathrm{HO}*}$ and overpotential for the OER which was experimentally determined in alkaline condition and theoretically determined, respectively.

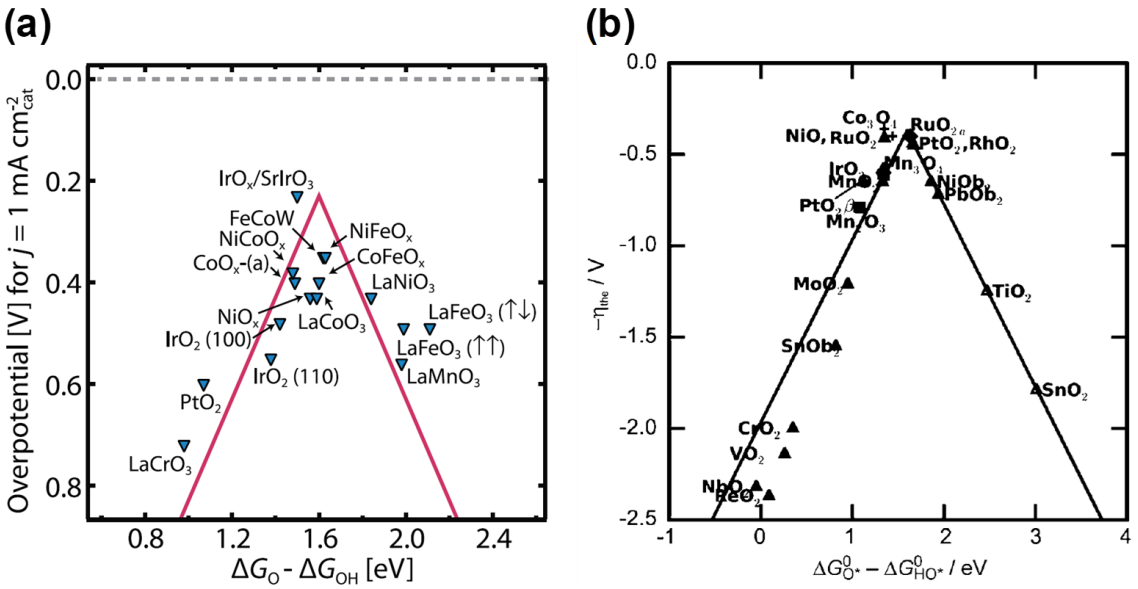

Figure 1.12 | Volcano-type relationship between $\Delta G_{\mathrm{O}*} - \Delta G_{\mathrm{HO}*}$ and the overpotential for the OER which was experimentally determined in alkaline condition (a) and theoretically determined (b), respectively. The volcano lines correspond to $\Delta G_{\mathrm{HOO}*} - \Delta G_{\mathrm{HO}*} = 3.2$ eV. (a): from ref. 4. Reprinted with permission from AAAS; (b): adapted with permission from ref. 109. Copyright 2011 Wiley-VCH Verlag GmbH & Co. KGaA, Weinheim.

This volcano-type relationship has been successful in explaining the activity trend of OER catalysts in alkaline conditions, which justifies the assumption of the reaction mechanism at least in some cases. Note that the activity of RuO_2 and IrO_2 is expected to be similar to non-noble-metal oxide catalysts in Figure 1.12b.

The direct-coupling mechanism was also theoretically investigated by DFT calculation. The existence of this mechanism in actual catalysis was supported by experimental results using isotopes.[111] Curiously, the result of DFT calculation of the thermodynamic energy levels of each intermediate in the direct-coupling mechanism by Panas *et al.* also indicated similar OER activity of Ir oxides and Mn oxides.[112] The reason for the difference in the OER activity between Ir oxides and Mn oxides in actual experimental cases was explained to be due to the difference in kinetics.

More simple descriptors of the activity of OER catalysts than $\Delta G_{O^*} - \Delta G_{HO^*}$ have been sought and reported both before and after the success of the volcano-type relationship summarized above. One reason of the investigation is the difficulty in the measurement and the control of the binding energy of adsorbates.[113] The descriptors summarized below are related to the d-band of metal oxides, which, to a first approximation, determines the bond strength between the surface and adsorbates.[114] Iwakura *et al.* reported that, with the increase of the number of d electrons, the OER activity of spinel oxides, $Co_xFe_{3-x}O_4$ and $Mn_xFe_{3-x}O_4$, increases but that of $Co_xFe_{3-x}O_4$ decreases in 1 M KOH. The result was explained by the increased stability of OH radicals on the surface with more d electrons. In the case of the former two spinel oxides, because the generation of OH radicals from hydroxide ions is rate-determining the activity increases with more d electrons, while, in the case of the latter oxide, the activity decreases with more d electrons because the chemical reaction between the surface OH radicals and hydroxide ions in the electrolyte is rate-

determining.[115] Bockris and Otagawa reported using 18 perovskite materials that the OER activity in 1 M NaOH increases with the increase of the number of d electrons, which was ascribed to increased occupancy of the antibonding orbitals of M–OH, where M denotes a surface metal atom.[116] In 2011, Shao-Horn *et al.* demonstrated a volcano-shaped dependence of the OER activity of more than ten perovskite oxides in 0.1 M KOH on the occupancy of e_g orbitals of surface metal cations, identifying $Ba_{0.5}Sr_{0.5}Co_{0.8}Fe_{0.2}O_{3-\delta}$ as the most active catalyst among the examined materials (Figure 1.13).[100] They argued that the filling of e_g orbitals is a more appropriate descriptor for the OER activity than the number of d electrons because the σ-bonding e_g orbitals overlap more strongly with oxygen-related adsorbates than the π-bonding t_{2g} orbitals.

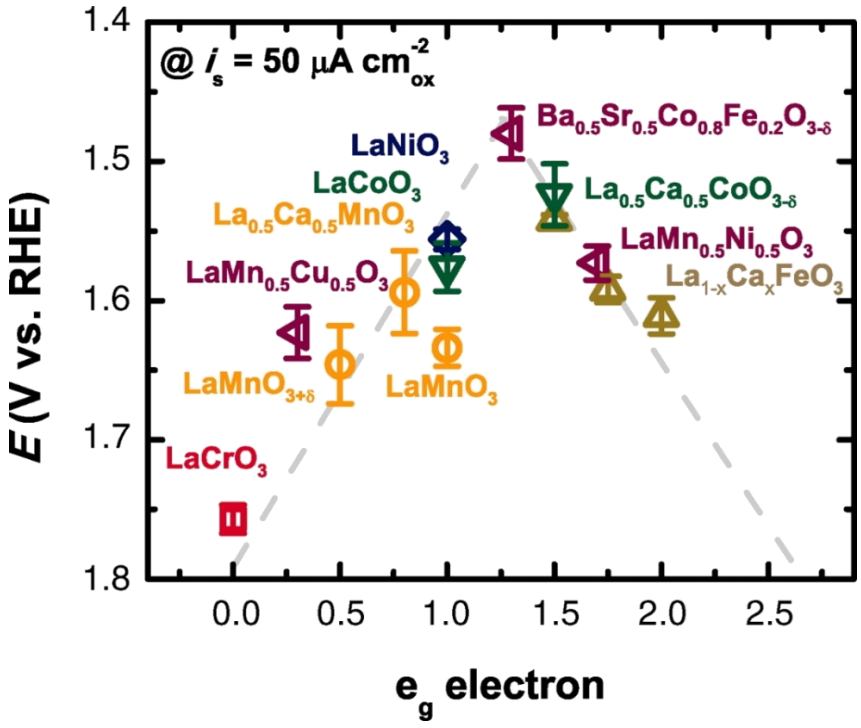

Figure 1.13 | The relationship between the overpotential for the OER at the current density of 50 μA cm^{-2} per the surface area of the catalyst and the occupancy of the e_g orbitals. The dashed volcano lines are only for the guidance of the eyes. From ref. 100. Reprinted with permission from AAAS.

Problems in Existing Theories

As mentioned above, there is a numerous number of reports of non-noble-metal-based OER catalysts with comparable activity to noble-metal-based catalysts at alkaline pH.[14,97] However, non-noble-metal-based OER catalysts with comparable activity to noble-metal-based catalysts in non-alkaline conditions have not been developed.[14,29] This activity discrepancy between alkaline and non-alkaline conditions is an example which shows the problems to be solved in existing theories summarized above. The existing theories overviewed above worked well in alkaline conditions, as shown in Figure 1.12a and 1.13 for example, while often do not work in non-alkaline conditions.

For example, based on the assumption of the acid–base mechanism (Equation 1.2–1.5), the overpotential becomes independent of pH; this is true in the case of Ir oxides, as shown in Figure 1.9a, but not in the case of Mn oxides (as discussed later; Figure 1.14). Although the volcano plot generated based on the assumption indicates that the activity of Ir oxides and Mn oxides are similar (Figure 1.12b), there is a significant activity discrepancy in neutral conditions. Similar overpotential for Ir oxides and Mn oxides was also predicted based on the assumption of the direct-coupling mechanism.[112]

Also, the activity descriptors based on the number of electrons in the e_g orbitals (or the d-band) worked well in alkaline conditions, and perovskite oxides which are more active than IrO_2 were found (Figure 1.13).[100] However, active catalysts in neutral conditions have not been established based on this approach, and there is a report which shows that the descriptor of the number of electrons in the e_g orbitals did not work in neutral conditions. Raabe *et al.* reported amorphization of the surface of praseodymium-doped perovskite $CaMnO_3$ observed by transmission electron microscopy (TEM) which proceeded under the reaction condition for the OER in neutral conditions. The generated near-surface oxygen vacancies decreased the Mn

valency and thus increased the occupation of the e_g orbitals, as evidenced by the results of the measurement of electron energy loss spectroscopy (EELS) and X-ray absorption near edge structure (XANES). Many perovskite oxides are stable during the OER only in alkaline conditions.[117]

Here, possible problems regarding the assumption of existing theories can be summarized, which can lead to wrong conclusions especially in the case of non-noble-metal OER catalysts in non-alkaline conditions.

First, the reaction steps are often assumed to be PCET. For example, all of the elementary electrochemical steps in the acid–base and direct-coupling mechanisms summarized above (Equation 1.2–1.7) are PCET. Based on the acid–base mechanism summarized in Equation 1.2–1.5, where all steps are PCET, the potential for the overall reaction depends on pH at the same rate with the Nernstian equation. Thus, the overpotential for the reaction from the thermodynamic equilibrium potential becomes independent of pH. This is true in the case of Ir oxides (Figure 1.9a), but not in the case for Mn oxides (discussed later; Figure 1.14).

Second, the existing theories usually assume clear two-dimensional surfaces without structural changes during the OER except for surface adsorbate species. The importance of consideration of three-dimensional structure was already proposed in the paper by Man *et al.*, which established the validity of the assumption of the acid–base mechanism, because the structure of surface species can be different from those on two-dimensional structures.[109] Recently, some results were reported considering three-dimensional coordination structures. Calle-Vallejo *et al.* showed by DFT calculation that the scaling relationship between ΔG_{HO*} and ΔG_{HOO*} holds true even on some surfaces with steps, kinks, or adatoms.[118] On the other hand, Calle-Vallejo *et al.* later also revealed deviation from scaling relationships between other pairs of surface species than HO* and HOO*

due to specific stabilization of the species on particular catalyst surface structures.[119] The participation of a surface –OH group bound to a neighboring metal atom to stabilize a surface –OO intermediate for the OER was also recently demonstrated by theoretical[120,121] and experimental[121] approaches. Those reports represent recent advancement of the understanding of the relationship between surface structures and catalytic activities. However, it is noted that dynamic structural changes which may proceed during the OER or the effect of external ligands which may coordinate to reaction species has not been considered; they are extensively utilized in enzymes.

Third, in the theoretical approaches summarized above, the RDS is considered to be related to the changes in chemical bonds, which is not true in the case of Mn or Fe oxides as summarized in the next Section.

1.3.2.4 Manganese-Oxide-Based Water Oxidation Electrocatalysts

As overviewed in Section 1.3.1, in Nature, no other reaction center for the OER other than the Mn_4 cluster has been revealed. Therefore, it has been expected that an active and stable OER catalyst in ambient non-alkaline conditions can be constructed by using Mn.

Overview of Catalysts Reported Before 2012

The electrochemical OER has been investigated using Mn oxides including simple oxides such as MnO_2, Mn_2O_3, and MnOOH, double oxides such as $MnFe_2O_3$, and molybdenum (Mo)- or tungsten (W)-doped MnO_2.[122–131] It was demonstrated that Mn oxides can function as active OER catalysts in alkaline conditions. For example, small overpotential for the OER of 360 mV and 390 mV was reported in the case of $MnFe_2O_4$ in 1 M KOH[129] and nanostructured MnOOH at pH 14

electrodeposited on Au,[126] respectively. The overpotential of 290 mV was also reported by using Mn_2O_3 at pH 14.[125] However, in neutral conditions, the OER activity of Mn oxides largely decreases. Tamura *et al.* reported that the overpotential largely increased from 300 mV at pH 14 to 610 mV at pH 6.5 in the case of MnO_2 electrodes.[122] Figure 1.14 shows the pH-dependence of the onset potential of the OER by δ-MnO_2 summarized by Takashima *et al.*[15] The reason why the OER activity of Mn-based electrocatalysts, which is active in alkaline conditions, decreases in neutral conditions had not been revealed.

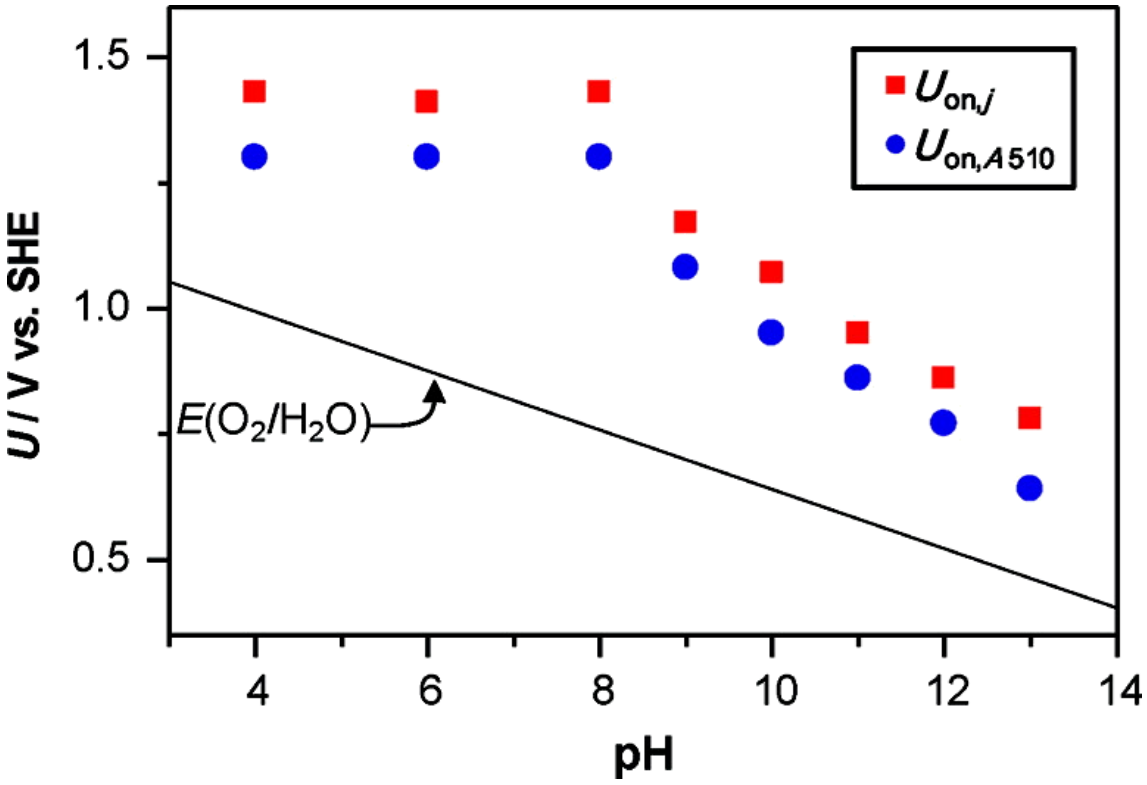

Figure 1.14 | pH dependence of the onset potential for the anodic current ($U_{on,j}$, red squares) and absorption at the wavelength of 510 nm ($U_{on,A510}$, blue circles). The black solid line shows the standard potential for the OER. Reprinted with permission from ref. 15. Copyright 2012 American Chemical Society.

Development After the Finding That Mn^{3+} Generation is the RDS

Takashima, Hashimoto, and Nakamura reported a mechanism in 2012 which explained why the overpotential for the OER by Mn oxides is not constant irrespective of pH as shown in Figure 1.14.[15] It was demonstrated based on *in-situ* electrochemical UV–vis spectroscopy and titration by pyrophosphate that the potential for the generation of Mn^{3+} and the onset potential for the OER correlate (Figure 1.14). Thus, Mn^{3+} can be considered as an intermediate species during the OER by Mn oxides. Mn^{3+} disproportionates in neutral conditions ($2Mn^{3+} \rightarrow Mn^{2+} + Mn^{4+}$), while Mn^{2+} and Mn^{4+} comproportionate in alkaline conditions ($Mn^{2+} + Mn^{4+} \rightarrow 2Mn^{3+}$). In other words, Mn^{3+} is stable at alkaline pH, while unstable at neutral pH. Thus, to accumulate Mn^{3+} in neutral conditions, electrochemical oxidation of Mn^{2+} to Mn^{3+} by the application of the potential where Mn^{3+} is more stable than Mn^{2+} is required. This potential ($Mn^{2+} \rightarrow Mn^{3+} + e^-$; E° = 1.51 V vs. SHE), however, is far more anodic than the thermodynamic potential for the OER ($2H_2O \rightarrow O_2 + 4H^+ + 4e^-$; E° = 0.81 V vs. SHE, at pH 7). The reason why the OER by Mn oxides requires an overpotential as large as 500–700 mV is now considered to be because of this high potential required for the electrochemical generation of Mn^{3+}.

Ooka and Nakamura *et al.* further generalized the idea to explain the difference between the OER activity of Ir oxides and Mn or Fe oxides in neutral conditions based on *in-situ* spectroelectrochemical studies.[132] As shown above, the generation of Mn^{3+} was found to be the RDS for the OER by Mn oxides.[15,16] Takashima *et al.* reported that the RDS for the OER by Fe oxides is the generation of Fe^{4+}.[133] The high potential required to generate Mn^{3+} or Fe^{4+} was explained to be because of their high-spin d^4 configuration resulting in charge disproportionation.[15,132,133] On the other hand, Ooka and Nakamura *et al.* demonstrated that, in the case of Ir oxides, charge accumulation is not rate-determining.[134,135] The discrepancy between the theoretical expectation of similar OER activity of Mn and Ir oxides and the actual activity

difference in neutral conditions was explained to be because of the difference in charge accumulation.[132]

Thus, one strategy to enhance the OER activity of Mn oxides in neutral conditions can be the development of the methods to stabilize Mn^{3+}. The importance of Mn^{3+} for the OER activity of Mn oxides in neutral conditions was also exemplified by the study of amorphized Mn oxides,[136,137] Mn oxides with noble metal substrates,[138] and electrodeposited Mn oxides[139] and a comparative study of Mn oxides.[140] The relationship between the crystal structures, the stability of Mn^{3+}, and the OER activity will be summarized more in detail in Section 3.1.

The stabilization of Mn^{3+} by rational approaches was achieved by the introduction of organic ligands. For example, the coordination of nitrogen-containing organic ligands to the octahedral Mn site of Mn oxides enhanced the OER activity,[18] a response that is attributed to the increased stabilization of Mn^{3+}.[15,16] The improved stability of Mn^{3+} is ascribed to the asymmetric ligand field, where the two e_g orbitals of Mn^{3+} have different energies and therefore the charge disproportionation of Mn^{3+} to Mn^{2+} and Mn^{4+} for eliminating the orbital degeneracy is effectively suppressed.[18,141] Also, pyridine derivatives were shown to enhance the OER activity of Mn oxides by inducing CPET, thereby reducing the required potential for the generation of Mn^{3+} *via* electrochemical oxidation of Mn^{2+}.[17] Najafpour *et al.* also reported the enhanced OER activity of Mn oxides modified by amino-acid residues or other ligands.[142–144]

Remaining Problems and Concept of This Study

Enhancement of the multi-electron-transfer OER activity of Mn oxides has been achieved by the introduction of organic ligands. Here, it can be noticed that the utilization of organic ligands for the OER is analogous to the Mn_4 cluster in PSII. Oxygenic photosynthesis with the Mn_4 cluster

in PSII as the reaction center for the OER is established as a system. On the other hand, however, there are some points in the artificial system consisted of Mn oxides and organic ligands for the OER which need to be improved the practical application.

First, the stability needs to be improved. The synthetic systems described above generally undergo the self-oxidation and resulting degradation of organic compounds. The TON of PSII reaches as high as ~10^6,[22] as previously mentioned. Second, the system needs to be compatible with industrial electrolyzer systems. Here, surprisingly, the existence of organic molecules around the OER catalysts is also the case in PEM electrolyzers, which exhibit high energy conversion efficiency (more details will be discussed in Chapter 4 and 5).[20] The realization of high activity in the combination of Mn oxides and PEM electrolyzers will be a significant advancement for the application of Mn oxides for high-efficiency conversion systems from renewable energy to chemical fuels. Also, it is noted that the effect of crystal or surface bonding structures was not discussed in the systems of Mn oxides and organic ligands summarized above. The consideration of crystal structures may be able to make the usage of organic ligands unnecessary if the crystal structure can already accommodate distortion. Also, if charge accumulation becomes no longer the RDS and the surface bonding changes becomes the RDS, the consideration of surface bonding structures and their changes during the OER will be important considering the theories for the development of the OER catalysts summarized above.

Based on the success of the systems consisting of Mn oxides and organic ligands, this study aimed to maximize the multi-electron-transfer ability of Mn oxides in solution systems and PEM electrolyzers by controlling the reaction intermediates by stable ligands or distortion in crystal structures, bridging the gap between PSII and industrially applicable energy conversion systems.

References of Chapter 1

1. J. A. Turner, Sustainable hydrogen production. *Science* **2004**, *305*, 972–974.
2. S. Chu and A. Majumdar, Opportunities and challenges for a sustainable energy future. *Nature* **2012**, *488*, 294–303.
3. N. S. Lewis and D. G. Nocera, Powering the planet: Chemical challenges in solar energy utilization. *Proc. Natl. Acad. Sci. U. S. A.* **2006**, *103*, 15729–15735.
4. Z. W. Seh, J. Kibsgaard, C. F. Dickens, I. Chorkendorff, J. K. Nørskov and T. F. Jaramillo, Combining theory and experiment in electrocatalysis: Insights into materials design. *Science* **2017**, *355*, eaad4998.
5. F. Birol, World Energy Outlook 2015, International Energy Agency (IEA), Paris, France, **2015**.
6. IPCC, **2014**: Climate Change 2014: Synthesis Report. Contribution of Working Groups I, II and III to the Fifth Assessment Report of the Intergovernmental Panel on Climate Change [Core Writing Team, R.K. Pachauri and L.A. Meyer (eds.)]. IPCC, Geneva, Switzerland, 151 pp.
7. United Nations / Framework Convention on Climate Change (**2015**) Adoption of the Paris Agreement, 21st Conference of the Parties, Paris, France: United Nations.
8. A. Fujishima and K. Honda, Electrochemical photolysis of water at a semiconductor electrode. *Nature* **1972**, *238*, 37–38.
9. A. J. Nozik, Photoelectrochemistry: Applications to solar energy conversion. *Annu. Rev. Phys. Chem.* **1978**, *29*, 189–222.
10. A. J. Bard and M. A. Fox, Artificial photosynthesis: Solar splitting of water to hydrogen and oxygen. *Acc. Chem. Res.* **1995**, *28*, 141–145.
11. X. Zou and Y. Zhang, Noble metal-free hydrogen evolution catalysts for water splitting.

Chem. Soc. Rev. **2015**, *44*, 5148–5180.

12. J. Qiao, Y. Liu, F. Hong and J. Zhang, A review of catalysts for the electroreduction of carbon dioxide to produce low-carbon fuels. *Chem. Soc. Rev.* **2014**, *43*, 631–675.
13. H. Dau, C. Limberg, T. Reier, M. Risch, S. Roggan and P. Strasser, The mechanism of water oxidation: From electrolysis via homogeneous to biological catalysis. *ChemCatChem* **2010**, *2*, 724–761.
14. C. C. L. McCrory, S. Jung, I. M. Ferrer, S. M. Chatman, J. C. Peters and T. F. Jaramillo, Benchmarking hydrogen evolving reaction and oxygen evolving reaction electrocatalysts for solar water splitting devices. *J. Am. Chem. Soc.* **2015**, *137*, 4347–4357.
15. T. Takashima, K. Hashimoto and R. Nakamura, Mechanisms of pH-dependent activity for water oxidation to molecular oxygen by MnO_2 electrocatalysts. *J. Am. Chem. Soc.* **2012**, *134*, 1519–1527.
16. T. Takashima, A. Yamaguchi, K. Hashimoto, H. Irie and R. Nakamura, In situ UV-vis absorption spectra of intermediate species for oxygen-evolution reaction on the surface of MnO_2 in neutral and alkaline media. *Electrochemistry* **2014**, *82*, 325–327.
17. A. Yamaguchi, R. Inuzuka, T. Takashima, T. Hayashi, K. Hashimoto and R. Nakamura, Regulating proton-coupled electron transfer for efficient water splitting by manganese oxides at neutral pH. *Nat. Commun.* **2014**, *5*, 4256.
18. T. Takashima, K. Hashimoto and R. Nakamura, Inhibition of charge disproportionation of MnO_2 electrocatalysts for efficient water oxidation under neutral conditions. *J. Am. Chem. Soc.* **2012**, *134*, 18153–18156.
19. J. Yano and V. Yachandra, Mn_4Ca cluster in photosynthesis: Where and how water is oxidized to dioxygen. *Chem. Rev.* **2014**, *114*, 4175–4205.
20. M. Carmo, D. L. Fritz, J. Mergel and D. Stolten, A comprehensive review on PEM water

electrolysis. *Int. J. Hydrogen Energy* **2013**, *38*, 4901–4934.

21. W. P. Jencks, Requirements for general acid–base catalysis of complex reactions. *J. Am. Chem. Soc.* **1972**, *94*, 4731–4732.

22. N. Cox, M. Retegan, F. Neese, D. A. Pantazis, A. Boussac and W. Lubitz, Electronic structure of the oxygen-evolving complex in photosystem II prior to O–O bond formation. *Science* **2014**, *345*, 804–808.

23. M. J. Russell and A. J. Hall, presented in part at Sixth International Congress on Carbon Dioxide Utilization, Breckenridge, Colorado, U. S. A., September **2001**.

24. K. Sauer and V. K. Yachandra, A possible evolutionary origin for the Mn_4 cluster of the photosynthetic water oxidation complex from natural MnO_2 precipitates in the early ocean. *Proc. Natl. Acad. Sci. U. S. A.* **2002**, *99*, 8631–8636.

25. Y. Umena, K. Kawakami, J.-R. Shen and N. Kamiya, Crystal structure of oxygen-evolving photosystem II at a resolution of 1.9 Å. *Nature* **2011**, *473*, 55–61.

26. T. J. Meyer, M. H. V. Huynh and H. H. Thorp, The possible role of proton-coupled electron transfer (PCET) in water oxidation by photosystem II. *Angew. Chem., Int. Ed.* **2007**, *46*, 5284–5304.

27. J. P. McEvoy and G. W. Brudvig, Water-splitting chemistry of photosystem II. *Chem. Rev.* **2006**, *106*, 4455–4483.

28. D. R. Weinberg, C. J. Gagliardi, J. F. Hull, C. F. Murphy, C. A. Kent, B. C. Westlake, A. Paul, D. H. Ess, D. G. McCafferty and T. J. Meyer, Proton-coupled electron transfer. *Chem. Rev.* **2012**, *112*, 4016–4093.

29. K. Jin, A. Chu, J. Park, D. Jeong, S. E. Jerng, U. Sim, H.-Y. Jeong, C. W. Lee, Y-S. Park, K. D. Yang, G. K. Pradhan, D. Kim, N.-E. Sung, S. H. Kim and K. T. Nam, Partially oxidized sub-10 nm MnO nanocrystals with high activity for water oxidation catalysis. *Sci. Rep.* **2015**,

5, 10279.

30. A. Nakamura, Y. Ota, K. Koike, Y. Hidaka, K. Nishioka, M. Sugiyama and K. Fujii, A 24.4% solar to hydrogen energy conversion efficiency by combining concentrator photovoltaic modules and electrochemical cells. *Appl. Phys. Exp.* **2015**, *8*, 107101.
31. J. F. Allen and W. Martin, Evolutionary biology: Out of thin air. *Nature* **2007**, *445*, 610–612.
32. B. Alberts, A. Johnson, J. Lewis, D. Morgan, M. Raff, K. Roberts and P. Walter, *Molecular biology of the cell, 6th edition*. Garland Science, New York, U. S. A., **2014**.
33. "Plant Cells, Chloroplasts, and Cell Walls." Scitable by Nature Education. http://www.nature.com/scitable/topicpage/plant-cells-chloroplasts-and-cell-walls-14053956 (accessed January 1, 2018).
34. B. Kok, B. Forbush and M. McGloin, Cooperation of charges in photosynthetic oxygen evolution. I. A linear four step mechanism. *Photochem. Photobiol.* **1970**, *11*, 457–475.
35. M. Suga, F. Akita, K. Hirata, G. Ueno, H. Murakami, Y. Nakajima, T. Shimizu, K. Yamashita, M. Yamamoto, H. Ago and J.-R. Shen, Native structure of photosystem II at 1.95 Å resolution viewed by femtosecond X-ray pulses. *Nature* **2015**, *517*, 99–103.
36. I. D. Young, M. Ibrahim, R. Chatterjee, S. Gul, F. D. Fuller, S. Koroidov, A. S. Brewster, R. Tran, R. Alonso-Mori, T. Kroll, T. Michels-Clark, H. Laksmono, R. G. Sierra, C. A. Stan, R. Hussein, M. Zhang, L. Douthit, M. Kubin, C. de Lichtenberg, L. V. Pham, H. Nilsson, M. H. Cheah, D. Shevela, C. Saracini, M. A. Bean, I. Seuffert, D. Sokaras, T.-C. Weng, E. Pastor, C. Weninger, T. Fransson, L. Lassalle, P. Bräuer, P. Aller, P. T. Docker, B. Andi, A. M. Orville, J. M. Glownia, S. Nelson, M. Sikorski, D. Zhu, M. S. Hunter, T. J. Lane, A. Aquila, J. E. Koglin, J. Robinson, M. Liang, S. Boutet, A. Y. Lyubimov, M. Uervirojnangkoorn, N. W. Moriarty, D. Liebschner, P. V. Afonine, D. G. Waterman, G. Evans, P. Wernet, H. Dobbek, W. I. Weis, A. T. Brunger, P. H. Zwart, P. D. Adams, A. Zouni,

J. Messinger, U. Bergmann, N. K. Sauter, J. Kern, V. K. Yachandra and J. Yano, Structure of photosystem II and substrate binding at room temperature. *Nature* **2016**, *540*, 453–457.

37. W. H. Baur, Rutile-type compounds. V. Refinement of MnO_2 and MgF_2. *Acta Cryst.* **1976**, *B32*, 2200–2204.

38. M. Regulski, R. Przeniosło, I. Sosnowska and J.-U. Hoffmann, Short and long range magnetic ordering in β-MnO_2 —A temperature study—. *J. Phys. Soc. Jpn.* **2004**, *73*, 3444–3447.

39. K. Saito, A. W. Rutherford and H. Ishikita, Energetics of proton release on the first oxidation step in the water-oxidizing enzyme. *Nat. Commun.* **2015**, *6*, 8488.

40. A. Grundmeier and H. Dau, Structural models of the manganese complex of photosystem II and mechanistic implications. *Biochim. Biophys. Acta, Bioenerg.* **2012**, *1817*, 88–105.

41. R. J. Debus, FTIR studies of metal ligands, networks of hydrogen bonds, and water molecules near the active site Mn_4CaO_5 cluster in photosystem II. *Biochim. Biophys. Acta, Bioenerg.* **2015**, *1847*, 19–34.

42. H. Sakamoto, T. Shimizu, R. Nagao and T. Noguchi, Monitoring the reaction process during the $S_2 \rightarrow S_3$ transition in photosynthetic water oxidation using time-resolved infrared spectroscopy. *J. Am. Chem. Soc.* **2017**, *139*, 2022–2029.

43. V. Krewald, M. Retegan, F. Neese, W. Lubitz, D. A. Pantazis and N. Cox. Spin state as a marker for the structural evolution of nature's water-splitting catalyst. *Inorg. Chem.* **2016**, *55*, 488–501.

44. P. E. M. Siegbahn, Water oxidation mechanism in photosystem II, including oxidations, proton release pathways, O–O bond formation and O_2 release. *Biochim. Biophys. Acta, Bioenerg.* **2013**, *1827*, 1003–1019.

45. N. Cox and J. Messinger, Reflections on substrate water and dioxygen formation. *Biochim.*

Biophys. Acta, Bioenerg. **2013**, *1827*, 1020–1030.

46. J.-R. Shen, The structure of photosystem II and the mechanism of water oxidation in photosynthesis. *Annu. Rev. Plant Biol.* **2015**, *66*, 23–48.

47. M. Pérez-Navarro, F. Neese, W. Lubitz, D. A. Pantazis and N. Cox. Recent developments in biological water oxidation. *Curr. Opin. Chem. Biol.* **2016**, *31*, 113–119.

48. D. J. Vinyard and G. W. Brudvig, Progress toward a molecular mechanism of water oxidation in photosystem II. *Annu. Rev. Phys. Chem.* **2017**, *68*, 101–116.

49. H. Dau, I. Zaharieva and M. Haumann, Recent developments in research on water oxidation by photosystem II. *Curr. Opin. Chem. Biol.* **2012**, *16*, 3–10.

50. L. V. Kulik, B. Epel, W. Lubitz and J. Messinger. ^{55}Mn pulse ENDOR at 34 GHz of the S_0 and S_2 states of the oxygen-evolving complex in photosystem II. *J. Am. Chem. Soc.* **2005**, *127*, 2392–2393.

51. L. V. Kulik, B. Epel, W. Lubitz and J. Messinger. Electronic structure of the Mn_4O_xCa cluster in the S_0 and S_2 states of the oxygen-evolving complex of photosystem II based on pulse ^{55}Mn-ENDOR and EPR spectroscopy. *J. Am. Chem. Soc.* **2007**, *129*, 13421–13435.

52. S. Petrie, R. J. Pace and R. Stranger, Resolving the differences between the 1.9 Å and 1.95 Å crystal structures of photosystem II: A single proton relocation defines two tautomeric forms of the water-oxidizing complex. *Angew. Chem., Int. Ed.* **2015**, *54*, 7120–7124.

53. V. Krewald, F. Neese and D. A. Pantazis, Resolving the Mn oxidation states in the OEC of natural photosynthesis. *Isr. J. Chem.* **2015**, *55*, 1219–1232.

54. H. Dau and M. Haumann, The manganese complex of photosystem II in its reaction cycle — Basic framework and possible realization at the atomic level. *Coord. Chem. Rev.* **2008**, *252*, 273–295.

55. L. Iuzzolino, J. Dittmer, W. Dörner, W. Meyer-Klaucke and H. Dau, X-ray absorption

spectroscopy on layered photosystem II membrane particles suggests manganese-centered oxidation of the oxygen-evolving complex for the S_0-S_1, S_1-S_2, and S_2-S_3 transitions of the water oxidation cycle. *Biochemistry* **1998**, *37*, 17112–17119.

56. J. Messinger, J. H. Robblee, U. Bergmann, C. Fernandez, P. Glatzel, H. Visser, R. M. Cinco, K. L. McFarlane, E. Bellacchio, S. A. Pizarro, S. P. Cramer, K. Sauer, M. P. Klein and V. K. Yachandra, Absence of Mn-centered oxidation in the $S_2 \rightarrow S_3$ transition: Implications for the mechanism of photosynthetic water oxidation. *J. Am. Chem. Soc.* **2001**, *123*, 7804–7820.
57. A. Boussac, J.-L. Zimmermann, A. W. Rutherford and J. Lavergne, Histidine oxidation in the oxygen-evolving photosystem-II enzyme. *Nature* **1990**, *347*, 303–306.
58. B. J. Hallahan, J. H. A. Nugent, J. T. Warden and M. C. W. Evans, Investigation of the origin of the "S3" EPR signal from the oxygen-evolving complex of photosystem 2: the role of tyrosine Z. *Biochemistry* **1992**, *31*, 4562–4573.
59. A. Boussac and A. W. Rutherford, The origin of the split S_3 EPR signal in Ca^{2+}-depleted photosystem II: Histidine versus tyrosine. *Biochemistry* **1992**, *31*, 7441–7445.
60. J. Stubbe and W. A. van der Donk, Protein radicals in enzyme catalysis. *Chem. Rev.* **1998**, *98*, 705–762.
61. M. L. Gilchrist, Jr., J. A. Ball, D. W. Randall and R. D. Britt, Proximity of the manganese cluster of photosystem II to the redox-active tyrosine Y_Z. *Proc. Natl. Acad. Sci. U. S. A.* **1995**, *92*, 9545–9549.
62. X.-S. Tang, D. W. Randall, D. A. Force, B. A. Diner and R. D. Britt, Manganese-tyrosine interaction in the photosystem II oxygen-evolving complex. *J. Am. Chem. Soc.* **1996**, *118*, 7638–7639.
63. M. Pourbaix, *Atlas of electrochemical equilibria*. Pergamon Press, Oxford, U. K., **1966**.
64. P. M. Wood, The potential diagram for oxygen at pH 7. *Biochem. J.* **1988**, *253*, 287–289.

65. W. H. Koppenol and J. F. Liebman, The oxidizing nature of the hydroxyl radical. A comparison with the ferryl ion (FeO^{2+}). *J. Phys. Chem.* **1984**, *88*, 99–101.

66. T. Shibamoto, Y. Kato, M. Sugiura and T. Watanabe, Redox potential of the primary plastoquinone electron acceptor Q_A in photosystem II from *Thermosynechococcus elongatus* determined by spectroelectrochemistry. *Biochemistry* **2009**, *48*, 10682–10684.

67. Y. Kato, R. Nagao and T. Noguchi, Redox potential of the terminal quinone electron acceptor Q_B in photosystem II reveals the mechanism of electron transfer regulation. *Proc. Natl. Acad. Sci. U. S. A.* **2016**, *113*, 620–625.

68. H. Ishikita, J. Biesiadka, B. Loll, W. Saenger and E.-W. Knapp, Cationic state of accessory chlorophyll and electron transfer through pheophytin to plastoquinone in photosystem II. *Angew. Chem., Int. Ed.* **2006**, *45*, 1964–1965.

69. H. Dau and I. Zaharieva, Principles, Efficiency, and blueprint character of solar-energy conversion in photosynthetic water oxidation. *Acc. Chem. Res.* **2009**, 42, 1861–1870.

70. P. J. Nixon and B. A. Diner, Aspartate 170 of the photosystem II reaction center polypeptide D1 is involved in the assembly of the oxygen-evolving manganese cluster. *Biochemistry* **1992**, *31*, 942–948.

71. R. J. Debus, K. A. Campbell, D. P. Pham, A. M. A. Hays and R. D. Britt, Glutamate 189 of the D1 polypeptide modulates the magnetic and redox properties of the manganese cluster and tyrosine Y_Z in photosystem II. *Biochemistry* **2000**, *39*, 6275–6287.

72. H. A. Chu, A. P. Nguyen and R. J. Debus, Amino acid residues that influence the binding of manganese or calcium to photosystem II. 2. The carboxy-terminal domain of the D1 polypeptide. *Biochemistry* **1995**, *34*, 5859–5882.

73. H. J. Hwang, P. Dilbeck, R. J. Debus and R. L. Burnap, Mutation of arginine 357 of the CP43 protein of photosystem II severely impairs the catalytic S-state cycle of the H_2O

oxidation complex *Biochemistry* **2007**, *46*, 11987–11997.

74. D. J. Vinyard, G. M. Ananyev and G. C. Dismukes, Photosystem II: The reaction center of oxygenic photosynthesis. *Annu. Rev. Biochem.* **2013**, *82*, 577–606.

75. K. Tanaka and D. Ooyama, Multi-electron reduction of CO_2 via Ru–CO_2, –C(O)OH, –CO, –CHO, and –CH_2OH species. *Coord. Chem. Rev.* **2002**, *226*, 211–218.

76. W. M. Haynes, *CRC handbook of chemistry and physics*. CRC Press, Boca Raton, Florida, U. S. A., **2014**.

77. H. A. Schwarz, Free radicals generated by radiolysis of aqueous solutions. *J. Chem. Educ.* **1981**, *58*, 101–105.

78. S. Yoshikawa and A. Shimada, Reaction mechanism of cytochrome *c* oxidase. *Chem. Rev.* **2015**, *115*, 1936–1989.

79. S. A. Roberts, A. Weichsel, G. Grass, K. Thakali, J. T. Hazzard, G. Tollin, C. Rensing and W. R. Montfort, Crystal structure and electron transfer kinetics of CueO, a multicopper oxidase required for copper homeostasis in *Escherichia coli*. *Proc. Natl. Acad. Sci. U. S. A.* **2002**, *99*, 2766–2771.

80. B. K. Burgess, The iron-molybdenum cofactor of nitrogenase. *Chem. Rev.* **1990**, *90*, 1377–1406.

81. R. H. Burris, Nitrogenases. *J. Biol. Chem.* **1991**, *266*, 9339–9342.

82. J. Tan and J. A. Cowan, Enzymic redox chemistry: A proposed reaction pathway for the six-electron reduction of SO_3^{2-} to S^{2-} by the assimilatory-type sulfite reductase from *Desulfovibrio vulgaris* (Hildenborough). *Biochemistry* **1991**, *30*, 8910–8917.

83. M. W. Adams and L. E. Mortenson, *Molybdenum Enzymes*. Wiley-Interscience, New York, U. S. A., **1985**.

84. M. W. Adams, The structure and mechanism of iron-hydrogenases. *Biochim. Biophys. Acta*,

Bioenerg. **1990**, *1020*, 115–145.

85. T. J. Jacobsson, V. Fjällström, M. Edoff and T. Edvinsson, Sustainable solar hydrogen production: from photoelectrochemical cells to PV-electrolyzers and back again. *Energy Environ. Sci.* **2014**, *7*, 2056–2070.

86. D. M. Fabian, S. Hu, N. Singh, F. A. Houle, T. Hisatomi, K. Domen, F. E. Osterloh and S. Ardo, Particle suspension reactors and materials for solar-driven water splitting. *Energy Environ. Sci.* **2015**, *8*, 2825–2850.

87. K. K. Sakimoto, N. Kornienko and P. Yang, Cyborgian Material design for solar fuel production: The emerging photosynthetic biohybrid systems. *Acc. Chem. Res.* **2017**, *50*, 476–481.

88. N.-T. Suen, S.-F. Hung, Q. Quan, N. Zhang, Y.-J. Xu and H. M. Chen, Electrocatalysis for the oxygen evolution reaction: recent development and future perspectives. *Chem. Soc. Rev.* **2017**, *46*, 337–365.

89. Y. Zhao, R. Nakamura, K. Kamiya, S. Nakanishi and K. Hashimoto, Nitrogen-doped carbon nanomaterials as non-metal electrocatalysts for water oxidation. *Nat. Commun.* **2013**, *4*, 2390.

90. S. Trasatti and G. Buzzanca, Ruthenium dioxide: a new interesting electrode material. Solid state structure and electrochemical behavior. *J. Electroanal. Chem.* **1971**, *29*, A1–A5.

91. A. Harriman, M. Richoux, P. A. Christensen, S. Moseri and P. Neta, Redox reactions with colloidal metal oxides. Comparison of radiation-generated and chemically generated $RuO_2 \cdot 2H_2O$. *J. Chem. Soc., Faraday Trans. 1* **1987**, *83*, 3001–3014.

92. J. Kiwi and M. Grätzel, Colloidal redox catalysts for evolution of oxygen and for light-induced evolution of hydrogen from water. *Angew. Chem., Int. Ed.* **1979**, *18*, 624–626.

93. A. Mills and T. Russell, Comparative study of new and established heterogeneous oxygen

catalysts. *J. Chem. Soc. Faraday Trans.* **1991**, *87*, 1245–1250.

94. Y. Zhao, N. M. Vargas-Barbosa, E. A. Hernandez-Pagan and T. E. Mallouk, Anodic deposition of colloidal iridium oxide thin films from hexahydroxyiridate(IV) solutions. *Small* **2011**, *7*, 2087–2093.

95. L. C. Seitz, C. F. Dickens, K. Nishio, Y. Hikita, J. Montoya, A. Doyle, C. Kirk, A. Vojvodic, H. Y. Hwang, J. K. Norskov and T. F. Jaramillo, A highly active and stable $IrO_x/SrIrO_3$ catalyst for the oxygen evolution reaction. *Science* **2016**, *353*, 1011–1014.

96. O. Diaz-Morales, S. Raaijman, R. Kortlever, P. J. Kooyman, T. Wezendonk, J. Gascon, W. T. Fu and M. T. M. Koper, Iridium-based double perovskites for efficient water oxidation in acid media. *Nat. Commun.* **2016**, *7*, 12363.

97. I. Roger, M. A. Shipman and M. D. Symes, Earth-abundant catalysts for electrochemical and photoelectrochemical water splitting. *Nat. Rev. Chem.* **2017**, *1*, 3.

98. M. D. Merrill and R. C. Dougherty, Metal oxide catalysts for the evolution of O_2 from H_2O. *J. Phys. Chem. C* **2008**, *112*, 3655–3666.

99. J. Luo, J.-H. Im, M. T. Mayer, M. Schreier, M. K. Nazeeruddin, N.-G. Park, S. D. Tilley, H. J. Fan and M. Grätzel, Water photolysis at 12.3% efficiency via perovskite photovoltaics and Earth-abundant catalysts. *Science* **2014**, *345*, 1593–1596.

100. J. Suntivich, K. J. May, H. A. Gasteiger, J. B. Goodenough and Y. Shao-Horn, A Perovskite oxide optimized for oxygen evolution catalysis from molecular orbital principles. *Science* **2011**, *334*, 1383–1385.

101. M. W. Kanan and D. G. Nocera, In situ formation of an oxygen-evolving catalyst in neutral water containing phosphate and Co^{2+}. *Science* **2008**, *321*, 1072–1075.

102. V. Y. Shafirovich, N. K. Khannanov and V. V. Strelets, Chemical and light-induced catalytic water oxidation. *Nouv. J. Chem.* **1980**, *4*, 81–84.

103. B. S. Brunschwig, M. H. Chou, C. Creutz, P. Ghosh and N. Sutin, Mechanisms of water oxidation to oxygen: cobalt(IV) as an intermediate in the aquocobalt(II)-catalyzed reaction. *J. Am. Chem. Soc.* **1983**, *105*, 4832–4833.

104. M. Dincă, Y. Surendranath and D. G. Nocera, Nickel-borate oxygen-evolving catalyst that functions under benign conditions. *Proc. Natl. Acad. Sci. U. S. A.* **2010**, *107*, 10337–10341.

105. J. G. McAlpin, Y. Surendranath, M. Dincă, T. A. Stich, S. A. Stoian, W. H. Casey, D. G. Nocera and R. D. Britt, EPR evidence for Co(IV) species produced during water oxidation at neutral pH. *J. Am. Chem. Soc.* **2010**, *132*, 6882–6883.

106. H. S. Ahn and T. D. Tilley, Electrocatalytic water oxidation at neutral pH by a nanostructured $Co(PO_3)_2$ anode. *Adv. Funct. Mater.* **2013**, *23*, 227–233.

107. T. Takashima, K. Ishikawa and H. Irie, Enhancement of oxygen evolution activity of ruddlesden-popper-type strontium ferrite by stabilizing Fe^{4+}. *J. Mater. Sci. Chem. Eng.* **2017**, *5*, 75927.

108. T. Takashima, K. Ishikawa and H. Irie, Efficient oxygen evolution on hematite at neutral pH enabled by proton-coupled electron transfer. *Chem. Commun.* **2016**, *52*, 14015–14018.

109. I C. Man, H.-Y. Su, F. Calle-Vallejo, H. A. Hansen, J. I. Martínez, N. G. Inoglu, J. Kitchin, T. F. Jaramillo, J. K. Nørskov and J. Rossmeisl, Universality in oxygen evolution electrocatalysis on oxide surfaces. *ChemCatChem* **2011**, *3*, 1159–1165.

110. M. T. M. Koper, Thermodynamic theory of multi-electron transfer reactions: Implications for electrocatalysis. *J. Electroanal. Chem.* **2011**, *660*, 254–260.

111. S. Fierro, T. Nagel, H. Baltruschat and C. Comninellis, Investigation of the oxygen evolution reaction on Ti/IrO_2 electrodes using isotope labelling and on-line mass spectrometry. *Electrochem. Commun.* **2007**, *9*, 1969–1974.

112. M. Busch, E. Ahlberg and I. Panas, Water oxidation on MnO_x and IrO_x: Why similar

performance? *J. Phys. Chem. C* **2013**, *117*, 288–292.

113. W. T. Hong, M. Risch, K. A. Stoerzinger, A. Grimaud, J. Suntivich and Y. Shao-Horn, Toward the rational design of non-precious transition metal oxides for oxygen electrocatalysis. *Energy Environ. Sci.* **2015**, *8*, 1404–1427.
114. M. T. M. Koper and R. A. van Santen, Interaction of H, O and OH with metal surfaces. *J. Electroanal. Chem.* **1999**, *472*, 126–136.
115. C. Iwakura, M. Nashioka and H. Tamura, Anodic evolution of oxygen on solid solutions with spinel-type structure. *Nippon Kagaku Kaishi (J. Chem. Soc. Jpn., Chem. Ind. Chem.)* **1982**, *8*, 1294–1298.
116. J. O. Bockris and T. Otagawa, The electrocatalysis of oxygen evolution on perovskites. *J. Electrochem. Soc.* **1984**, *131*, 290–302.
117. S. Raabe, D. Mierwaldt, J. Ciston, M. Uijttewaal, H. Stein, J. Hoffmann, Y. Zhu, P. Blöchl and C. Jooss, In situ electrochemical electron microscopy study of oxygen evolution activity of doped manganite perovskites. *Adv. Funct. Mater.* **2012**, *22*, 3378–3388.
118. F. Calle-Vallejo, D. Loffreda, M. T. M. Koper and P. Sautet, Introducing structural sensitivity into adsorption-energy scaling relations by means of coordination numbers. *Nat. Chem.* **2015**, *7*, 403–410.
119. H. Li, Y. Li, M T. M. Koper and F. Calle-Vallejo, Bond-making and breaking between carbon, nitrogen, and oxygen in electrocatalysis. *J. Am. Chem. Soc.*, **2014**, *136*, 15694–15701.
120. Y. Ping, R. J. Nielsen and W. A. Goddard III, The reaction mechanism with free energy barriers at constant potentials for the oxygen evolution reaction at the IrO_2 (110) surface. *J. Am. Chem. Soc.* **2017**, *139*, 149–155.
121. R. R. Rao, M. J. Kolb, N. B. Halck, A. F. Pedersen, A. Mehta, H. You, K. A. Stoerzinger, Z.

Feng, H. A. Hansen, H. Zhou, L. Giordano, J. Rossmeisl, T. Vegge, I. Chorkendorff, I. E. L. Stephens and Y. Shao-Horn, Towards identifying the active sites on RuO_2(110) in catalyzing oxygen evolution. *Energy Environ. Sci.* **2017**, *10*, 2626–2637.

122. M. Morita, C. Iwakura and H. Tamura, The anodic characteristics of manganese dioxide electrodes prepared by thermal decomposition of manganese nitrate. *Electrochim. Acta* **1977**, *22*, 325–328.
123. M. Morita, C. Iwakura and H. Tamura, The anodic characteristics of modified Mn oxide electrode: Ti/RuOx/MnOx. *Electrochim. Acta* **1977**, *23*, 331–335.
124. Y. Gorlin and T. F. Jaramillo, A bifunctional nonprecious metal catalyst for oxygen reduction and water oxidation. *J. Am. Chem. Soc.* **2010**, *132*, 13612–13614.
125. M. Morita, C. Iwakura and H. Tamura, The anodic characteristics of massive manganese oxide electrode. *Electrochim. Acta* **1979**, *24*, 357–362.
126. M. S. El-Deab, M. I. Awad, A. M. Mohammad and T. Ohsaka, Enhanced water electrolysis: Electrocatalytic generation of oxygen gas at manganese oxide nanorods modified electrodes. *Electrochem. Commun.* **2007**, *9*, 2082–2087.
127. A. M. Mohammad, M. I. Awad, M. S. El-Deab, T. Okajima and T. Ohsaka, Electrocatalysis by nanoparticles: Optimization of the loading level and operating pH for the oxygen evolution at crystallographically oriented manganese oxide nanorods modified electrodes. *Electrochim. Acta* **2008**, *53*, 4351–4358.
128. S. Trasatti, Electrocatalysis in the anodic evolution of oxygen and chlorine. *Electrochim. Acta* **1984**, *29*, 1503–1512.
129. R. N. Singh, J. P. Singh, H. N. Cong and P. Chartier, Effect of partial substitution of Cr on electrocatalytic properties of $MnFe_2O_4$ towards O_2-evolution in alkaline medium. *Int. J. Hydrogen Energy* **2006**, *31*, 1372–1378.

130. K. Fujimura, K. Izumiya, A. Kawashima, E. Akiyama, H. Habazaki, N. Kumagai and K. Hashimoto, Anodically deposited manganese-molybdenum oxide anodes with high selectivity for evolving oxygen in electrolysis of seawater. *J. Appl. Electrochem.* **1999**, *29*, 765–771.

131. K. Izumiya, E. Akiyama, H. Habazaki, N. Kumagai, A. Kawashima and K. Hashimoto, Anodically deposited manganese oxide and manganese-tungsten oxide electrodes for oxygen evolution from seawater. *Electrochim. Acta* **1998**, *43*, 3303–3312.

132. H. Ooka, T. Takashima, A. Yamaguchi, T. Hayashi and R. Nakamura, Element strategy of oxygen evolution electrocatalysis based on *in situ* spectroelectrochemistry. *Chem. Commun.* **2017**, *53*, 7149–7161.

133. T. Takashima, K. Ishikawa and H. Irie, Detection of intermediate species in oxygen evolution on hematite electrodes using spectroelectrochemical measurements. *J. Phys. Chem. C* **2016**, *120*, 24827–24834.

134. H. Ooka, A. Yamaguchi, T. Takashima, K. Hashimoto and R. Nakamura, Efficiency of oxygen evolution on iridium oxide determined from the pH dependence of charge accumulation. *J. Phys. Chem. C* **2017**, *121*, 17873–17881.

135. H. Ooka, Y. Wang, A. Yamaguchi, M. Hatakeyama, S. Nakamura, K. Hashimoto and R. Nakamura, Legitimate intermediates of oxygen evolution on iridium oxide revealed by *in situ* electrochemical evanescent wave spectroscopy. *Phys. Chem. Chem. Phys.* **2016**, *18*, 15199–15204.

136. A. Indra, P. W. Menezes, I. Zaharieva, E. Baktash, J. Pfrommer, M. Schwarze, H. Dau and M. Driess, Active mixed-valent MnO_x water oxidation catalysts through partial oxidation (corrosion) of nanostructured MnO particles. *Angew. Chem., Int. Ed.* **2013**, *52*, 13206–13210.

137. I. Zaharieva, P. Chernev, M. Risch, K. Klingan, M. Kohlhoff, A. Fischer and H. Dau, Electrosynthesis, functional, and structural characterization of a water-oxidizing manganese oxide. *Energy Environ. Sci.* **2012**, *5*, 7081–7089.

138. C. H. Kuo, W. Li, L. Pahalagedara, A. M. El-Sawy, D. Kriz, N. Genz, C. Guild, T. Ressler, S. L. Suib and J. He, Understanding the role of gold nanoparticles in enhancing the catalytic activity of manganese oxides in water oxidation reactions. *Angew. Chem., Int. Ed.* **2015**, *54*, 2345–2350.

139. M. Huynh, D. K. Bediako and D. G. Nocera, A functionally stable manganese oxide oxygen evolution catalyst in acid. *J. Am. Chem. Soc.* **2014**, *136*, 6002–6010.

140. D. M. Robinson, Y. B. Go, M. Mui, G. Gardner, Z. Zhang, D. Mastrogiovanni, E. Garfunkel, J. Li, M. Greenblatt and G. C. Dismukes, Photochemical water oxidation by crystalline polymorphs of manganese oxides: Structural requirements for catalysis. *J. Am. Chem. Soc.* **2013**, *135*, 3494–3501.

141. I. I. Mazin, D. I. Khomskii, R. Lengsdorf, J. A. Alonso, W. G. Marshall, R. M. Ibberson, A. Podlesnyak, M. J. Martínez-Lope and M. M. Abd-Elmeguid, Charge ordering as alternative to Jahn-Teller distortion. *Phys. Rev. Lett.* **2007**, *98*, 176406.

142. M. M. Najafpour, M. Z. Ghobadi, B. Haghighi, T. Tomo, R. Carpentier, J.-R. Shen and S. I. Allakhverdiev, A nano-sized manganese oxide in a protein matrix as a natural water-oxidizing site. *Plant Physiol. Biochem.* **2014**, *81*, 3–15.

143. M. M. Najafpour, M. Z. Ghobadi, D. J. Sedigh and B. Haghighi, Nano-sized layered manganese oxide in a poly-L-glutamic acid matrix: a biomimetic, homogenized, heterogeneous structural model for the water-oxidizing complex in photosystem II. *RSC Adv.* **2014**, *4*, 39077–39081.

144. M. M. Najafpour, D. J. Sedigh, S. M. Hosseini and I. Zaharieva, Treated nanolayered Mn

oxide by oxidizable compounds: A strategy to improve the catalytic activity toward water oxidation. *Inorg. Chem.* **2016**, *55*, 8827–8832.

Chapter 2.

Water Oxidation by Manganese Oxides in the Presence of Amino-Acid Analogs

2.1 Introduction

As summarized in Section 1.3.2.4, recently, several beneficial roles of organic compounds for the OER activity of Mn-based catalysts at neutral pH were revealed. However, the synthetic systems described above composed of Mn oxides and organic compounds generally undergo the self-oxidation and resulting degradation of organic compounds. Here, the focus is put on the indispensability and the stability of amino-acid residues around the Mn_4 cluster of PSII.

During the OER, as already discussed in Section 1.3.1.2, nine amino-acid residues belonging to the two proteins (D1 and CP43) of PSII are directly coordinated or hydrogen-bonded to the cluster (Figure 2.1a) and provide a structural and electrostatic environment indispensable for the function of PSII.[1] The importance of these amino acids is demonstrated by the fact that any point mutation of the nine residues drastically reduces the OER activity of the Mn_4 cluster.[2–5] D1-Asp61 has also been regarded as an important residue as a proton acceptor in the CPET to prevent the charge buildup during Kok cycle and the starting point of the proton exit pathway,[6] which is also shown in Figure 2.1a. The residues, however, seem to be at risk for the oxidative decomposition, because the chlorophyll dimer P_{680} in PSII generates the highest oxidative potential known in biology (1.15–1.26 V vs. SHE)[7–9] for initiating the OER. In fact, it remains uncertain whether the histidine directly liganded to the Mn_4 cluster, D1-His332 (Figure 2.1a), is subject to one-electron oxidation to a transient radical during Kok cycle.[10–16] Still, the residues around the Mn_4 cluster are highly stable against oxidative decomposition and therefore the TON of PSII can reach as high as ~10^6,[18] even if transient oxidation is operative in this system.

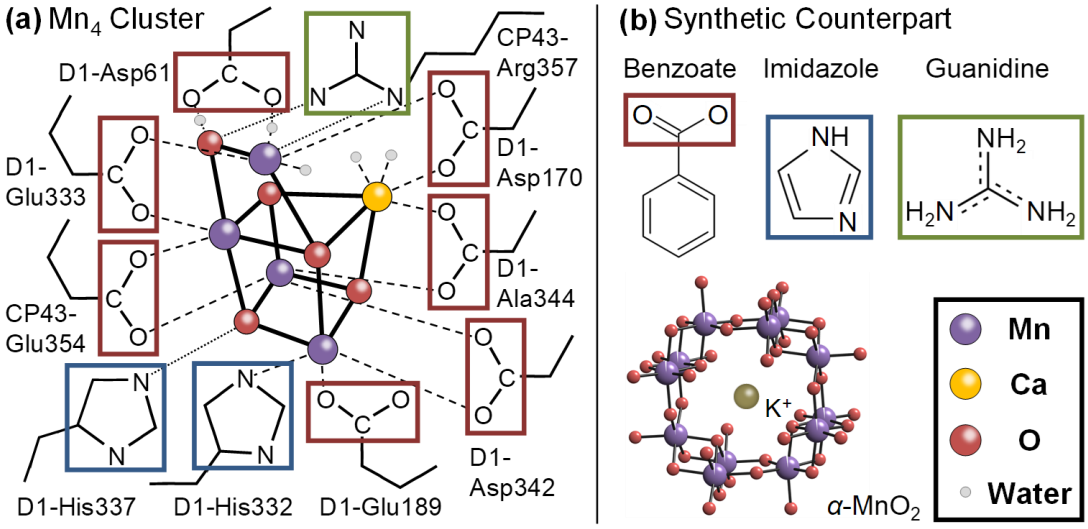

Figure 2.1 | (a) A schematic diagram of the ligand environment around the Mn_4 cluster in PSII[1] (broken lines: coordination bonds, dotted lines: hydrogen bonds). (b) The synthetic counterpart of PSII examined in this study. The red, blue and green boxes are shown around carboxyl, imidazolyl, and guanidino groups, respectively.

Although organic compounds are indispensable for the efficient OER for both natural and artificial Mn-based catalysts, there is a distinct difference in the stability against the self-oxidation. As determining the origin of the different stability is expected to provide the new design strategy of Mn-based OER catalysts that are highly efficient and stable under neutral conditions, possible oxidation pathways of organic compounds in a synthetic counterpart were here analyzed and compared them with extant PSII from the viewpoint of energetics.

Russell, Hall, Sauer, and Yachandra proposed that the Mn_4 cluster in PSII originate from a Mn mineral.[19,20] Sauer and Yachandra further speculated based on the bond length that the origin was a tunnel-type Mn oxide, such as α-MnO_2, which contains all four Mn cluster arrangements possible in this mineral class (Figure 2.1b).[20] Fine-tuning of the catalytic activity was also proposed to occur through the reorganization and modification of the Mn oxide mineral during the incorporation into a protein.[20] Regardless of the underlying process, the interaction between a

Mn compound and the surrounding amino-acid residues could have influenced the evolution of the ancestor of PSII. In the present study, α-MnO_2 and several artificial amino-acid analogs, including benzoate, imidazole, and guanidine, were therefore used as a synthetic model of the reaction center of PSII (Figure 2.1b).

2.2 Experimental Methods

Anodic reactions by α-MnO_2 electrodes in electrolyte containing artificial amino-acid analogs were first investigated by measuring anodic current and the evolution of oxygen and carbon dioxide over a range of potentials using a potentiostat, needle-type oxygen microsensor (OMS), and inlet electrochemical mass spectroscopy (EC-MS) system. Particulate film electrodes were prepared with synthesized α-MnO_2 powder[21,22] using a spray deposition method, as previously described.[23] The artificial amino-acid analogs benzoate, imidazole, and guanidine were dissolved in the electrolyte, which consisted of 0.5 M Na_2SO_4. The pH of the electrolyte was adjusted using NaOH and H_2SO_4. Other details are as follows.

Synthesis of α-MnO_2 Powder

The α-MnO_2 powder was synthesized as previously reported.[21,22] 1.10 g of $KMnO_4$ in 20 mL of water was stirred for 30 minutes at 60 ℃. Separately, 1.89 g of $MnSO_4 \cdot 5H_2O$ in 25 mL of a 2 M acetic acid aqueous solution was stirred for 20 minutes at room temperature. The solutions were mixed and heated for 2 hours at 80 ℃ under a stirred condition. The particles thus obtained were collected, washed, and dried overnight at 60 ℃.

Preparation of α-MnO_2 Particulate Film Electrodes

Particulate film electrodes of α-MnO_2 were prepared by a spray deposition method as previously described.[23] The amount of deposited α-MnO_2 was ~0.14 mg cm^{-2} unless otherwise noted. In this case, 75 mg of the α-MnO_2 powder was ground in an agate mortar for 5 minutes and suspended in 100 mL of highly pure Milli-Q water (18 MΩ cm^{-1}) by a sonicator (Q700, QSonica). The suspension was sprayed by a spray gun (ST-6, Fuso Seiki Co., Ltd.) onto a clean conducting fluorine-tin-oxide-coated glass substrate (SPD Laboratory, Inc.) heated at 200 ℃. The electrodes were gently washed with the highly pure Milli-Q water and calcined in air for 4 hours at 500 ℃. The deposited amount was controlled by the initial amount of the α-MnO_2 powder.

Electrochemical Measurement in General

Current density (*j*) and potential (*U*) were controlled and measured with a commercial potentiostat and potential programmer (HZ-5000, Hokuto Denko), using a Pt wire as the counter electrode and a Ag/AgCl/KCl (saturated) electrode as the reference electrode. Na_2SO_4 was used as the supporting electrolyte with the concentration set at 0.5 M. Sodium benzoate, imidazole, and guanidine sulfate were used as artificial amino-acid analogs and were introduced by dissolving them into the electrolyte. The electrolyte solution was prepared using the highly pure Milli-Q water and reagent-grade chemicals, and the pH was adjusted using 1.0 M H_2SO_4 and 1.0 M NaOH. Guanidine sulfate and isotopic reagents (D_2O, and D_2SO_4 for pD adjustment) were obtained from Sigma-Aldrich, and all other reagents are obtained from Wako and used without further purification.

Oxygen Measurement by a Fluorescence-Based Needle-Type Microsensor

The concentration of dissolved oxygen in the electrolyte solution was monitored using a

fluorescence-based needle-type OMS (Microx TX3-trace, PreSens) under stirred condition.

Tafel Plots

Tafel plots were made by plotting steady-state current at each potential. The electrolyte was filled and stirred by a stir bar at *ca.* 1000 rpm. The amount of deposited α-MnO_2 was decreased to be ~0.056 mg cm^{-2} to lessen the effect of pseudo-capacitance. The highest potential was kept for more than 500 seconds to avoid the effect of pseudo-capacitance. At other potentials, the steady-state current was measured after 90 seconds. The solution resistance was measured and the resulting ohmic potential loss was corrected.

pH Dependence of Potential Under a Constant Current Condition

pH dependence of potential under a constant current condition was measured by plotting the potential during the change of pH by the addition of NaOH aqueous solution. The electrolyte was filled and stirred by a stir bar at *ca.* 800 rpm. The amount of deposited α-MnO_2 was decreased to be ~0.056 mg cm^{-2} to lessen the effect of pseudo-capacitance. Although ohmic potential loss cannot be corrected because of the change in the composition of the electrolyte, the change in the solution resistance was so small that the slope value was not affected in the experimental accuracy in this time.

Kinetic Isotope Effect Measurement

KIE was measured based on the ratio of current density during linear sweep voltammetry (LSV). The concentration of sodium benzoate was 0.5 M, and the scan rate was 10 mV s^{-1}. pD was adjusted based on the relationship between pD and pH: pD = pH + 0.4.[24] The amount of deposited α-MnO_2 was ~0.056 mg cm^{-2}. The KIE was calculated at the potentials where the current density

reaches 0.25 mA cm^{-2} in undeuterated electrolyte. The measurement was conducted twice.

Fourier-Transform Infrared Spectroscopy

The structure of bases on the surface of α-MnO_2 was analyzed by an FT-IR spectrometer (Vertex 70, Bruker). 60 mg of α-MnO_2 powder was immersed in 10 mL of the solution of sodium benzoate or imidazole with 0.1 M deprotonated anions whose pH was adjusted to 7.5 by H_2SO_4 or NaOH. The solution was stirred for 12 hours. The powder was then separated by suction filtration with a hydrophilic polytetrafluoroethylene (PTFE) membrane filter with a 0.2 μm pore size (JGWP04700, Merck Millipore), followed by vacuum drying in a Schlenk flask. As a control sample, α-MnO_2 powder immersed in the highly pure Milli-Q water was also prepared. After ground in an agate mortar, 20 mg of the dried powder was pressed by a hydraulic press (SSP-10A, Shimadzu) into a pellet with a diameter of 12 mm for the measurement.

Inlet Electrochemical Mass Spectroscopy

Inlet EC-MS was also performed to measure the onset potentials of oxygen and carbon dioxide evolution. The principle of the EC-MS system was the same as previously reported.[25,26] A stainless capillary connected a gas-tight electrochemical chamber and a quadrupole mass spectrometer (QMG 220 M1, Pfeiffer Vacuum). The end of the capillary in the electrochemical chamber was covered with a microporous PTFE membrane (Poreflon WP-010-80, Sumitomo Electric Fine Polymer). Before measuring the evolution of oxygen or carbon dioxide, the electrochemical chambers were bubbled with argon for 30 minutes.

In-situ UV–Vis Spectroscopy

Optical absorption of electrodes in contact with the electrolyte was measured by a UV–vis

spectrometer (UV-2550, Shimadzu) equipped with a multipurpose large-sample compartment with a built-in integrating sphere (MPC-2200, Shimadzu), by placing electrodes in front of the integrating sphere and collecting diffused transmission light. The amount of deposited α-MnO_2 was decreased to be ~0.056 mg cm^{-2} to lessen the original absorption by the catalyst.

2.3 Results and Discussion

The presence of benzoate in the electrolyte increased both the anodic current and concentration of dissolved oxygen generated by the α-MnO_2 electrode (Figure 2.2). In the absence of benzoate, the slope of the Tafel plot was 120.7 mV (Figure 2.2a-1, inset), indicating that the RDS of the OER is a one-electron transfer reaction.[27,28] Also, the potential at a constant current was not dependent on pH (Figure 2.3), indicating that the reaction order of the proton concentration in the total reaction rate was zero. This further suggested that proton transfer was not involved in the RDS or during the pre-equilibrium phase of the step.[27,28] The results from the mechanistic analysis are consistent with previous reports that the RDS of the OER on α-MnO_2 is the one-electron oxidation from Mn^{2+} to Mn^{3+} without proton transfer.[29,30] In contrast, after the addition of benzoate to the electrolyte, the slope value of the Tafel plot decreased (Figure 2.2a-1, inset) and the potential at a constant current exhibited pH dependence (Figure 2.3). The H/D KIE also increased from 1.18 ± 0.09 to 1.45 ± 0.05 (pH(pD) 7). These results affirm that the reaction order of the proton concentration increased in the total reaction rate equation by the addition of benzoate.[27,28] The observed enhancement of the OER activity in response to the induction of proton transfer is consistent with the previous finding that CPET is required to avoid the formation of high-energy intermediates (Mn^{3+}–OH_2), leading to the enhancement of the activity for the OER.[23] Considering the libido rule of general acid–base catalysis,[31] which shows that the pK_a

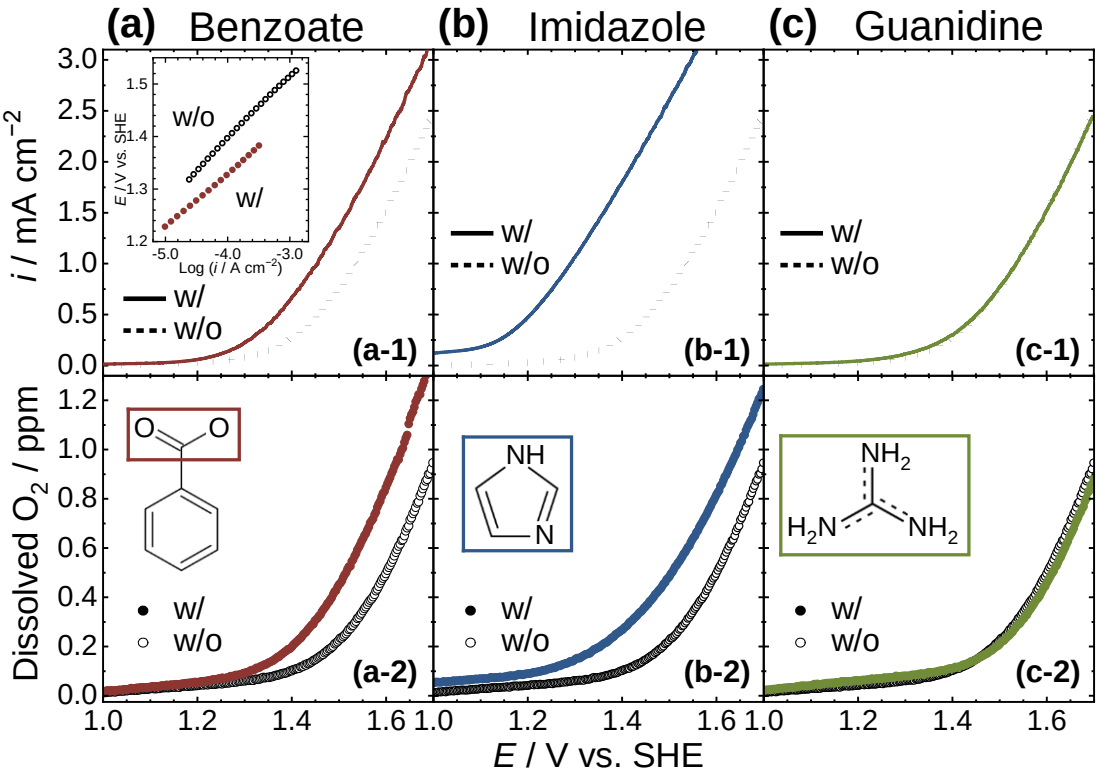

Figure 2.2 | Changes in anodic current density and dissolved oxygen concentration for α-MnO_2 electrodes by the addition of artificial amino-acid analogs (pH 7.5, scan rate: 1 mV s^{-1}, concentration of benzoate, imidazole (deprotonated form), and guanidine: 50 mM). Inset: Tafel plots (slope: 101.4 mV dec^{-1} (w/ benzoate), 120.7 mV dec^{-1} (w/o)).

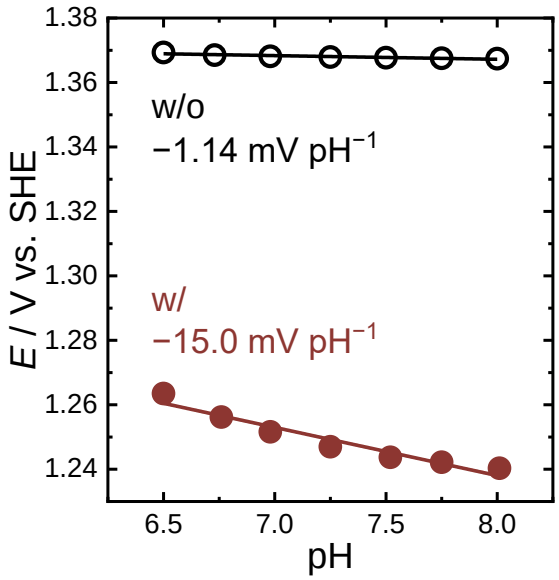

Figure 2.3 | pH dependence of potential at a constant current density (50 μA cm^{-2}) in the absence and presence of 50 mM of benzoate.

value of bases have to be intermediate between the pK_a of Mn^{3+}–OH_2 (0.7) and that of Mn^{2+}–OH_2 (10.6) to induce CPET,[23,31] benzoate is eligible to be a CPET inducer, as the pK_a is 4.2.[32]Furthermore, FT-IR measurement showed the formation of outer-sphere complexes of benzoate and the surface of α-MnO_2, a suitable configuration for the induction of CPET (Figure 2.4 and 2.5).

The effect of imidazole on the OER was also examined (Figure 2.2b). In the presence of imidazole, a 250-mV negative shift in the onset potential of the anodic current (E_{onset}), defined as the potential at a current density of 0.5 mA cm^{-2}, was observed for the α-MnO_2 electrode (Figure 2.2b-1). However, the magnitude of the onset potential shift of the O_2 production monitored by O_2 microsensor was only 130 mV (at 0.2 ppm), which was substantially smaller than the shift in E_{onset} (Figure 2.2b-2). The shift in the onset potential of the O_2 production was also smaller than that of E_{onset} when histidine was added to the electrolyte (Figure 2.6). The substantial difference in the potential shift for the onset of anodic current and O_2 production implied that the oxidation of imidazole and histidine proceeded in a more negative potential region than that for the OER.

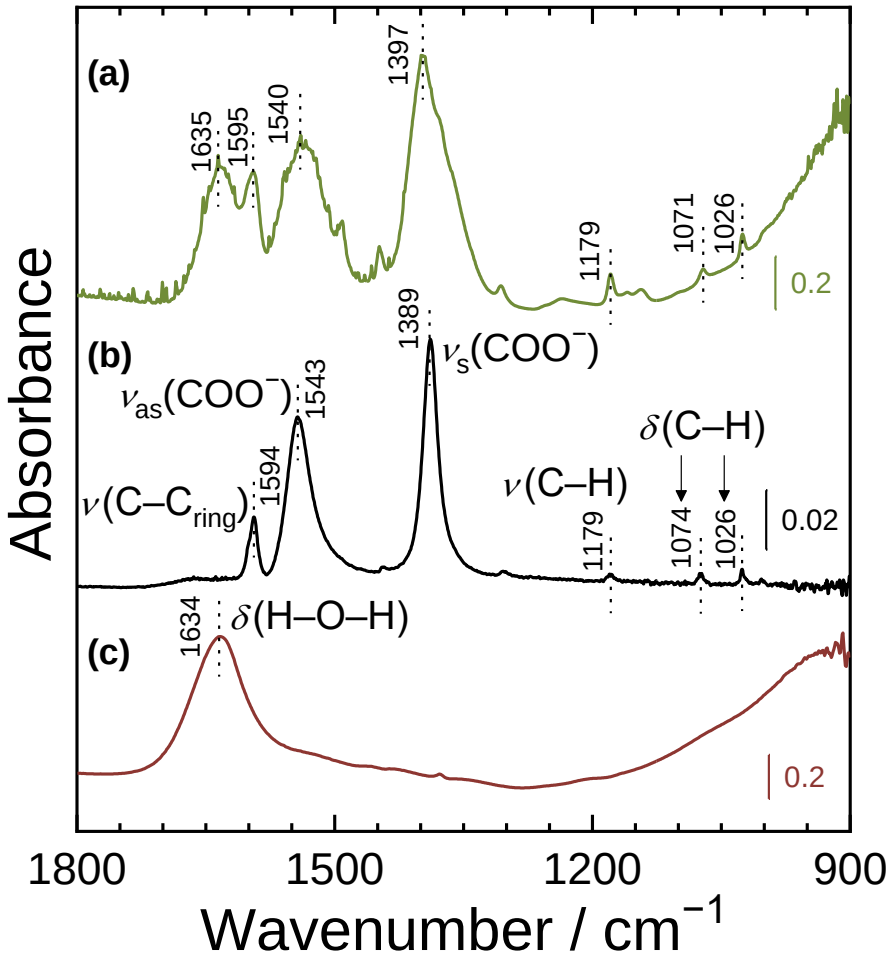

Figure 2.4 | FT-IR spectra of (a) α-MnO_2 after the immersion in the solution of 0.1 M deprotonated benzoate at pH 7.5 adjusted by NaOH for 12 hours, (b) the solution of 0.1 M deprotonated benzoate at pH 7.5 adjusted by NaOH, and (c) α-MnO_2. In (b), the observed peaks at 1388 cm^{-1} and 1541 cm^{-1} can be assigned to the symmetric and asymmetric stretching mode of COO^- ($\nu_s(COO^-)$ and $\nu_{as}(COO^-)$), respectively. The peak at 1594 cm^{-1} can be assigned to the stretching mode of C–C (aromatic ring) ($\nu(C–C_{ring})$).[33,34] The small peak at 1179 cm^{-1} was assigned to a C–H stretching mode, and those at 1071 cm^{-1} and 1026 cm^{-1} were assigned to C–H in-plane bending modes.[35] In (a), the band of $\nu_s(COO^-)$ shifted to higher frequency region, which indicated the chemisorption of benzoate on the surface of α-MnO_2.[33] The small shift (8 cm^{-1}), as well as broadening of the bands of $\nu_s(COO^-)$ and $\nu_{as}(COO^-)$, is in favor of the formation of outer-sphere complexes.[33] On the other hand, the positions of the bands from the aromatic ring were almost constant. Those results indicate that benzoate formed outer-sphere complexes with the surfaces of α-MnO_2, as shown in Figure 2.5, which is a suitable conformation for the induction of CPET.

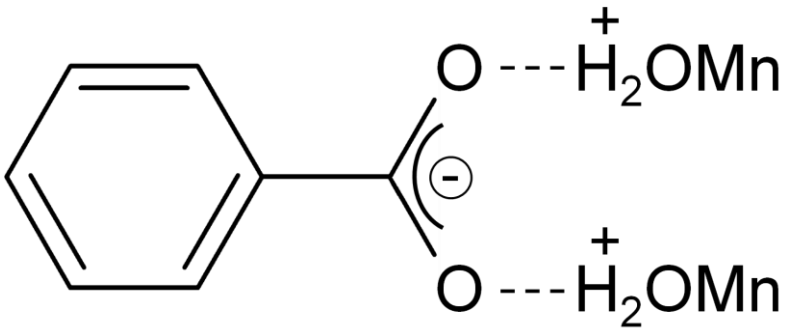

Figure 2.5 | Schematic representation of surface complexation of benzoate on the surface of α-MnO_2.[33]

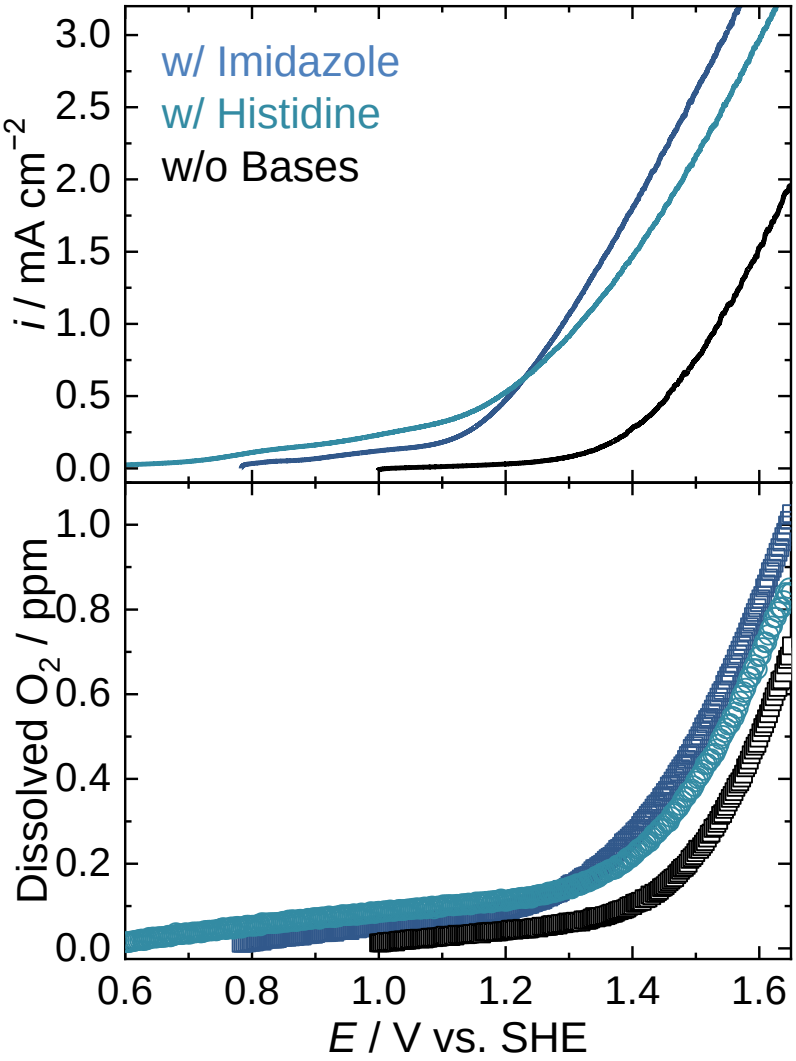

Figure 2.6 | Potential dependence of current density and dissolved amount of O_2 in the presence of imidazole or histidine (pH 7.5, scan rate: 1 mV s^{-1}, concentration of deprotonated imidazole ring: 50 mM).

To further examine the reason for this difference, *in-situ* EC-MS for the simultaneous monitoring of the anodic current and mass signals of volatile products, and UV–vis measurements were conducted.

During an anodic potential scan of α-MnO_2 in the presence of imidazole, increases in the ion current for oxygen (m/z = 32) were detected with a simultaneous production of carbon dioxide (m/z = 44) at the onset potential of approximately 1.25 V (vs. SHE) (Figure 2.7a-2 and a-3). No other volatile products, such as NO and NO_2, were detected in the EC-MS analysis. However, the onset potential of the anodic current was approximately 0.8 V, which was 250 mV more negative than that of the ion current for oxygen (Figure 2.2b and 2.7a). These results demonstrated that the coulombic efficiency for the OER between 0.8 and 1.25 V was determined to be zero. In the

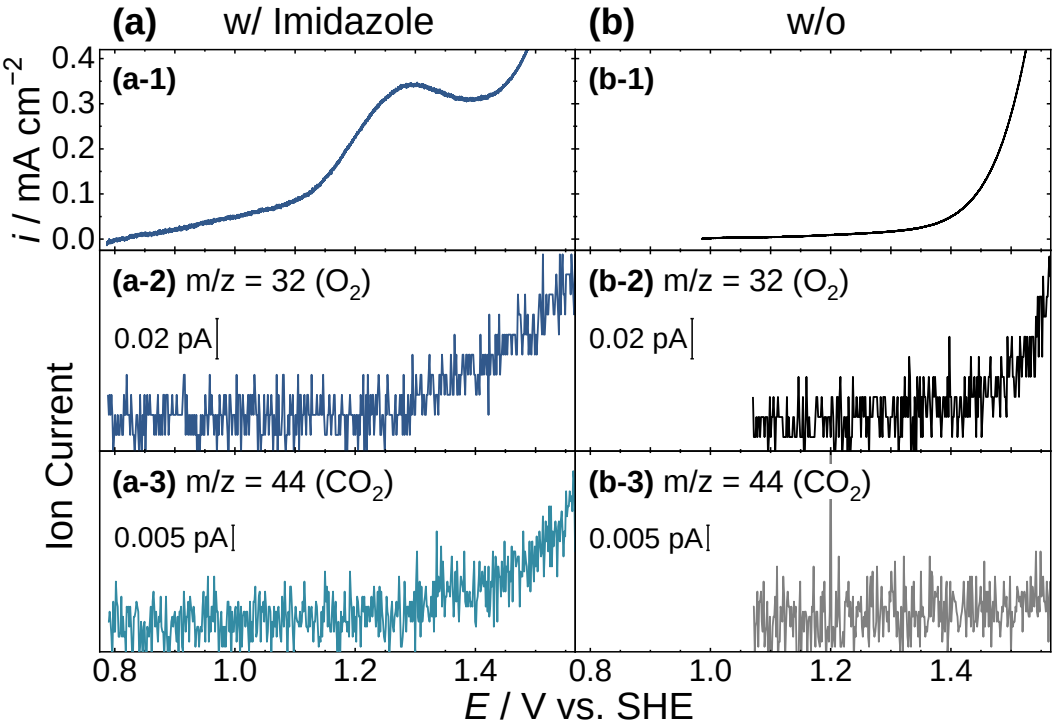

Figure 2.7 | (a-1, b-1) Current density and (a-2,3, b-2,3) mass signals during the anodic potential scan of α-MnO_2 electrodes before and after the addition of 50 mM of the deprotonated form of imidazole (pH 7.5, scan rate: 0.5 mV s^{-1}, unstirred).

absence of imidazole, the ion current for oxygen accompanied with anodic current and carbon dioxide was not detected (Figure 2.7b). Furthermore, a decrease in the time-dependent *in-situ* UV–vis absorption of α-MnO_2 electrodes in contact with the electrolyte supplemented with imidazole at resting potential, centered at 510 nm, was observed (Figure 2.8), with new FT-IR peaks assignable to oxidation products of imidazole (Figure 2.9), indicating that electrons injected from imidazole to α-MnO_2 were used to reduce Mn^{4+} to form soluble Mn^{2+} ions. These results are consistent with the expectation that, although imidazole enhanced OER, the oxidation of imidazole proceeded in a more negative potential region than that for the OER with the concurrent dissolution of Mn^{2+}.

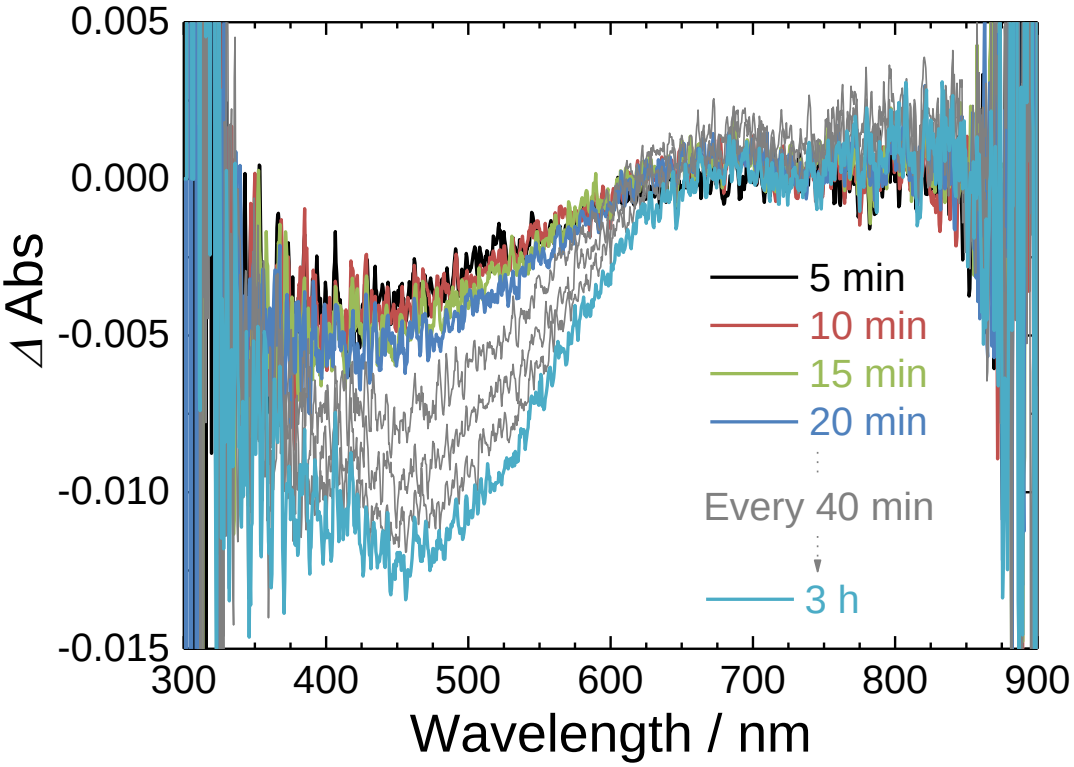

Figure 2.8 | Changes in the UV–vis spectra of an α-MnO_2 electrode in contact with the electrolyte which contained 500 mM deprotonated imidazole (pH 7.5) at rest potential. The spectrum immediately after the contact with the electrolyte was used as a reference.

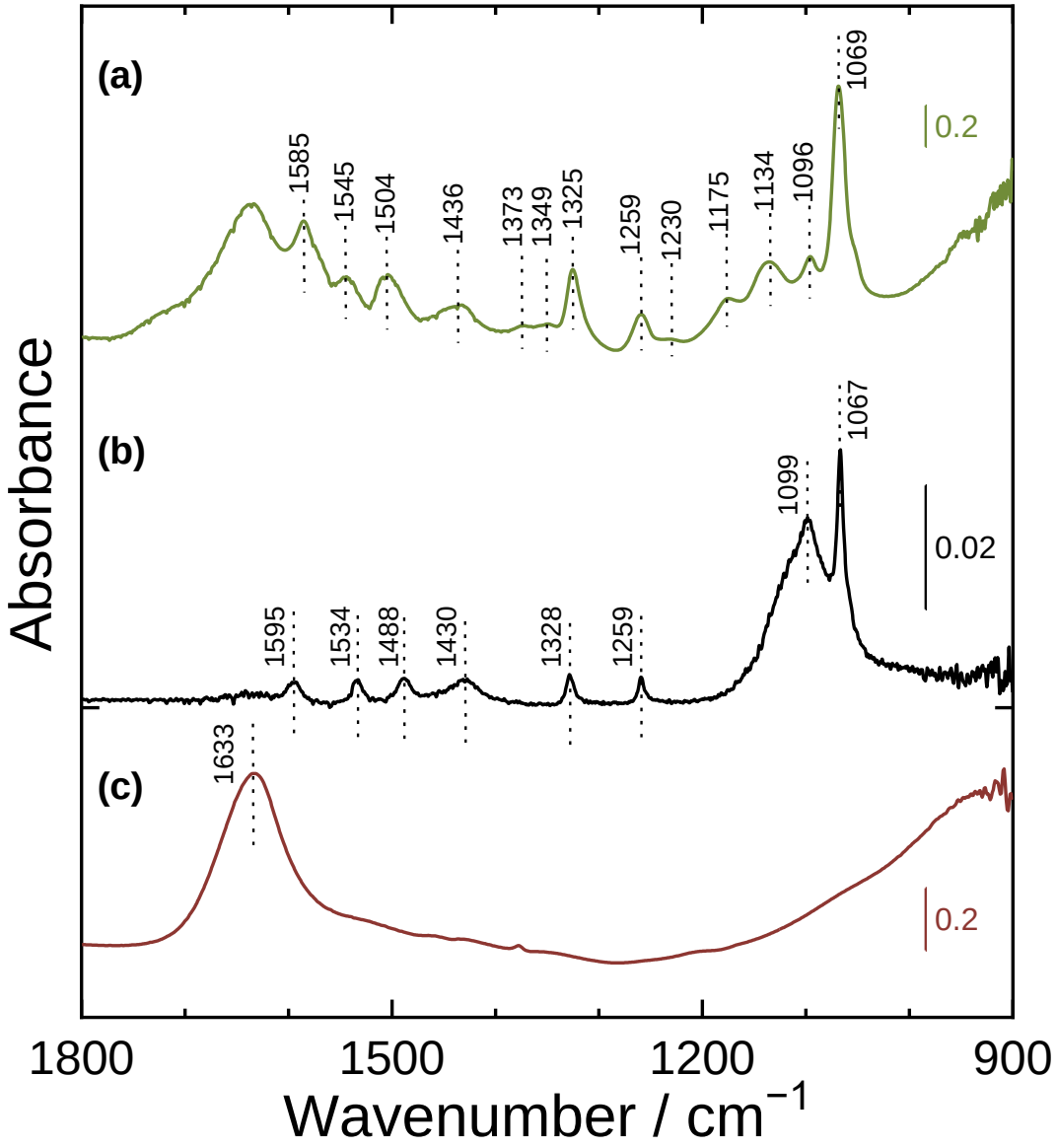

Figure 2.9 | FT-IR spectra of (a) α-MnO_2 after the immersion in the solution of 0.1 M deprotonated imidazole at pH 7.5 adjusted by H_2SO_4 for 12 hours, (b) the solution of 0.1 M deprotonated imidazole at pH 7.5 adjusted by H_2SO_4, and (c) α-MnO_2. The number of peaks increased after the interaction with α-MnO_2, compared to the spectra of the imidazole solution. The new peaks are regarded to be assignable to the oxidation products. The derivatives of urea or nitronate were shown as oxidation products of imidazolyl groups in the previous studies,[36–38] which can be the candidates for the products in the present cases.

In contrast to benzoate and imidazole, the addition of guanidine to the electrolyte resulted in a negligible difference in both the anodic current and OER (Figure 2.2c). This finding is consistent with the fact that the pK_a of guanidine is 13.6,[32] which exceeds the maximum permissible value to function as a CPET inducer. It also showed that the oxidation of guanidine was negligible in the potential range for the measurement.

The electrochemical analysis of the function of amino-acid analogs using the synthetic counterpart of PSII revealed that benzoate enhanced the OER activity by inducing CPET (Figure 2.2a and 2.3). Although imidazole also enhanced the OER activity, oxidation of imidazole and dissolution of α-MnO_2 severely competed with the OER (Figure 2.2b and 2.7), a property that is in sharp contrast with the stable existence of the histidine ligands, D1-His332, and the catalytic core of Mn_4 cluster in PSII (Figure 2.1a).

To better understand the reasons for the stability differences of the systems composed of imidazolyl group and α-MnO_2 or the Mn_4 cluster, pH-dependent energy diagrams of water and amino acid oxidation for these systems were constructed (Figure 2.10). The constructed diagrams include the equilibrium potential of the OER, potential of the α-MnO_2 electrodes at 10 μA cm^{-2} (E_{onset}') in the presence of imidazole or histidine measured in the present study, redox potential of the one-electron oxidation (E_1) of histidine in aqueous solution determined in a previous pulse radiolysis study,[39] and the reported E_1 values of tyrosine in aqueous solution,[40] the Mn_4 cluster ($E_1(S_{i+1}/S_i)$),[41,42] redox-active tyrosine residue D1-Tyr161 (Y_Z),[41–43] and P_{680}[7–9] in PSII. To the author's knowledge, the experimental E_1 value of imidazole has not been reported to date. However, this value can be estimated from the reported experimental value of vertical ionization energy (VIE).[44]

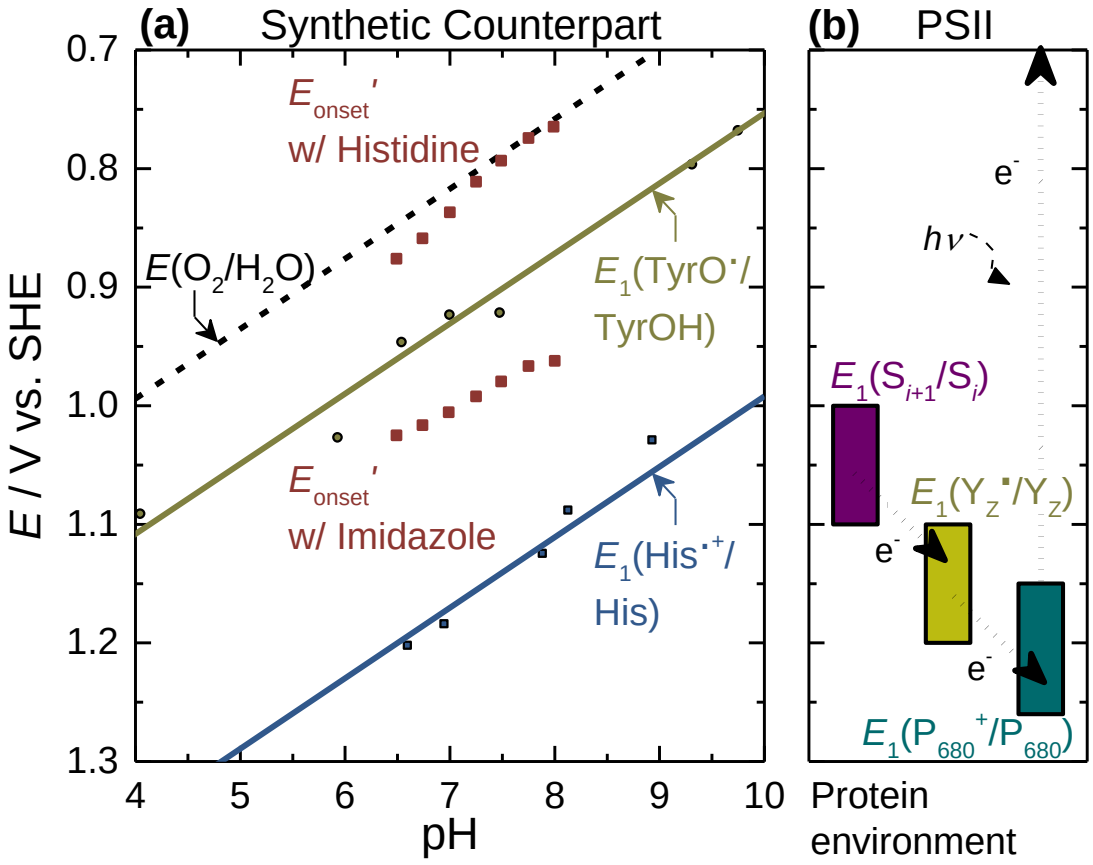

Figure 2.10 | Thermodynamic potential values related to the oxidation of imidazole and histidine (a) on α-MnO_2 and (b) the Mn_4 cluster. The presented values included those experimentally obtained in this study and reported in the literature.[7–9,39–43] (Potential vs. SHE was calculated using the reported potential of SHE vs. vacuum, +4.28 V.[45,46])

Details of this calculation of E_1 of imidazole are as follows.

Equilibrium Between Differently Protonated States of Imidazole and Imidazole Radicals

First, the equilibrium between differently protonated states of imidazole and imidazole radicals are summarized in Scheme 2.1.

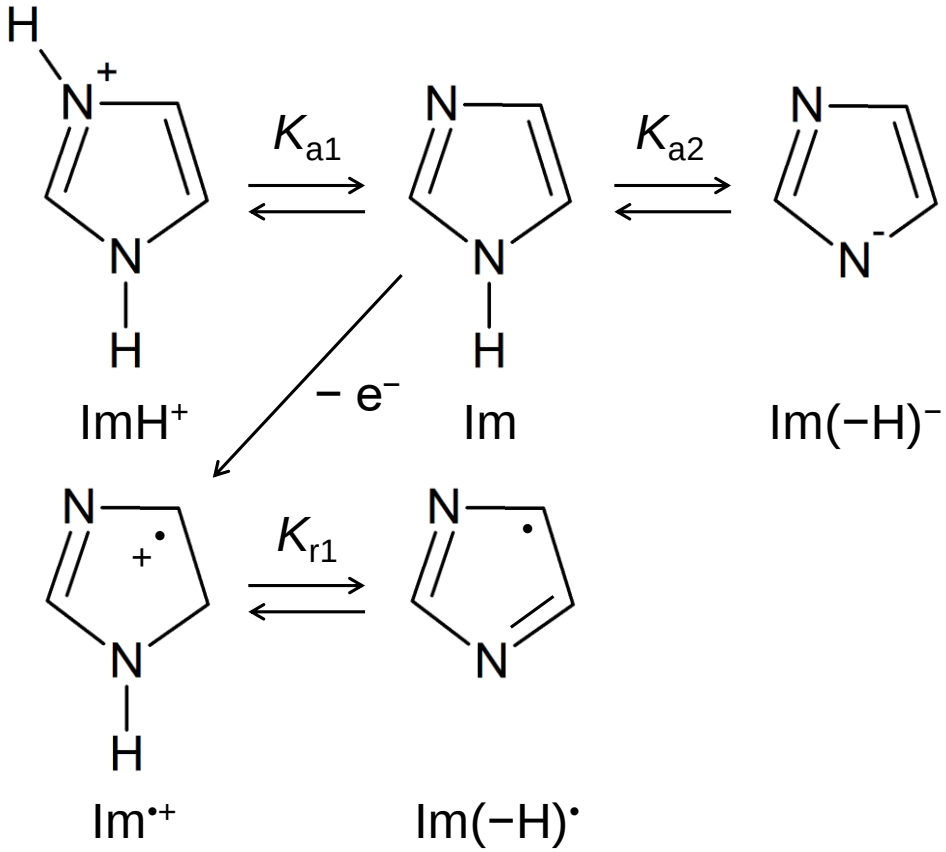

Scheme 2.1 | Protonation equilibrium of imidazole and imidazole radicals.

$ImH^{\bullet 2+}$, the protonated form of $Im^{\bullet +}$, is thermodynamically unstable and deprotonates, thus virtually does not exist. Equilibrium constants are given by following equations:

$$K_{a1} = \frac{[Im][H^+]}{[ImH^+]}, K_{a2} = \frac{[Im(-H)^-][H^+]}{[Im]}, K_{r1} = \frac{[Im(-H)^\bullet][H^+]}{[Im^{\bullet +}]} \quad (2.1)$$

pK_{a1} = 7.05 and pK_{a2} = 14.5;[47] pK_{r1} has not been reported to the author's knowledge.

Conversion of Vertical Ionization Energy to E_1

As mentioned above, experimental values of the E_1 of imidazole has not been reported so far to

the author's knowledge. However, an experimental value of the VIE of imidazole has been reported by a study using photoelectron spectroscopy of liquid microjet.[44] Thus, the standard E_1 ($E_1^\circ(\mathrm{Im}^{\bullet+}/\mathrm{Im})$) can be obtained by subtracting outer-sphere reorganization energy (λ) from VIE.

According to the report, the VIE of neutral imidazole (Im) is +3.98 V vs. SHE.[44] Here, VIE vs. SHE was calculated by using the reported potential of SHE vs. vacuum, +4.28 V.[45,46] λ is estimated to be smaller than 1 eV as for the reactions on electrodes in water with the diameter of the reactant larger than 2 Å.[48] Thus, $E_1^\circ(\mathrm{Im}^{\bullet+}/\mathrm{Im})$ can be estimated to be more positive than +2.98 V vs. SHE.

pH Dependence of E_1

Analysis of the pH dependence of E_1 requires consideration of the protonation equilibrium and can be estimated by reference to the method reported by Schroeder *et al.*[49]

Here, $[\mathrm{Im}]_{\mathrm{total}}$ and $[\mathrm{Im}^{\bullet}]_{\mathrm{total}}$ are defined as follows:

$$[\mathrm{Im}]_{\mathrm{total}} = [\mathrm{ImH}^+] + [\mathrm{Im}] + [\mathrm{Im}(-\mathrm{H})^-] = [\mathrm{Im}] \cdot \left(\frac{[\mathrm{H}^+]}{K_{\mathrm{a1}}} + 1 + \frac{K_{\mathrm{a2}}}{[\mathrm{H}^+]} \right) \tag{2.2}$$

$$[\mathrm{Im}^{\bullet}]_{\mathrm{total}} = [\mathrm{Im}^{\bullet+}] + [\mathrm{Im}(-\mathrm{H})^{\bullet}] = [\mathrm{Im}^{\bullet+}] \cdot \left(1 + \frac{K_{\mathrm{r1}}}{[\mathrm{H}^+]} \right) \tag{2.3}$$

Thus,

$$[\mathrm{Im}] = [\mathrm{Im}]_{\mathrm{total}} \cdot \frac{K_{\mathrm{a1}}[\mathrm{H}^+]}{[\mathrm{H}^+]^2 + K_{\mathrm{a1}}[\mathrm{H}^+] + K_{\mathrm{a1}}K_{\mathrm{a2}}} \tag{2.4}$$

$$[\mathrm{Im}^{\bullet+}] = [\mathrm{Im}^{\bullet}]_{\mathrm{total}} \cdot \frac{[\mathrm{H}^+]}{[\mathrm{H}^+] + K_{\mathrm{r1}}} \tag{2.5}$$

Thus, a Nernst equation for E_1 can be written as follows:

$$E_1 = E_1^{\circ}(\mathrm{Im}^{\bullet+}/\mathrm{Im}) + \frac{RT}{F}\ln\left(\frac{[\mathrm{Im}^{\bullet+}]}{[\mathrm{Im}]}\right) \quad (2.6)$$

$$= E_1^{\circ}(\mathrm{Im}^{\bullet+}/\mathrm{Im}) + \frac{RT}{F}\ln\left(\frac{1}{K_{a1}}\cdot\frac{[\mathrm{H}^+]^2 + K_{a1}[\mathrm{H}^+] + K_{a1}K_{a2}}{[\mathrm{H}^+] + K_{r1}}\right) \quad (2.7)$$

Note that $[\mathrm{Im}]_{total}$ equals to $[\mathrm{Im}^{\bullet}]_{total}$ at E_1. By substitution of the pK values, E_1 at the standard condition at pH 7.5 can be calculated as follows:

$$E_1 \text{ / V vs. SHE} = E_1^{\circ}(\mathrm{Im}^{\bullet+}/\mathrm{Im}) \text{ / V vs. SHE} - 0.4359 - 0.05916\log_{10}(10^{-7.5} + K_{r1}) \quad (2.8)$$

Here, $E_1^{\circ}(\mathrm{Im}^{\bullet+}/\mathrm{Im})$ corresponds to the E_1 estimated from the VIE. Therefore, for E_1 to be more negative than E_{onset} (@ 75 μA cm^{-2}) in the presence of imidazole at pH 7.5, even when λ = 1 eV, pK_{r1} have to be less than −27.6. pK_{r1} has not been reported to the author's knowledge, but considering that the corresponding pK value of histidine is 5–7,[39] it can be safely estimated that pK_{r1} is larger than −27.6. Thus, E_{onset} (@ 75 μA cm^{-2}) (Figure 2.10a) can be estimated to be well more negative than E_1.

Based on the pH-dependent energy diagram, it was found that E_1 of histidine is approximately 300-mV more positive than E_{onset}' in the presence of histidine (Figure 2.10a) at pHs ranging from 6 to 8. E_1 of imidazole was also estimated to be more positive than E_{onset}' in the presence of imidazole, suggesting that the one-electron oxidation reaction of histidine and imidazole is thermodynamically unfavorable on α-MnO_2 at neutral pH. As E_{onset}' in the presence of histidine and imidazole showed pH dependence, it appears that the experimentally observed decomposition of histidine and imidazole on α-MnO_2 (Figure 2.2b, 2.6, and 2.7) is a consequence of a proton-

coupled multi-electron oxidation reaction, which results in the simultaneous dissolution of Mn^{2+} (Figure 2.8).

Then, how is the oxidation of imidazolyl groups effectively prevented in PSII? In PSII, a potential cascade exists between P_{680} and the Mn_4 cluster, with Y_Z serving as an intermediate (Figure 2.10b). In addition, the E_1 values of aromatic amino acids such as tryptophan and tyrosine are predicted to be more positive in protein environments compared to aqueous solutions because of the low dielectric constant of the former (~3–5 in PSII)[50] and the lack of effective protonic contact with the bulk solution which allows deprotonation.[43,44] Consistent with this prediction, the E_1 value of Y_Z was found to be approximately 100–200-mV more positive than that of tyrosine in aqueous solution, as shown in Figure 2.10a. If the same mechanism holds true for the E_1 of imidazolyl groups in protein environments, the generation of transient histidine radicals *via* the one-electron oxidation of D1-His332 (Figure 2.1a) may also be thermodynamically unfavorable.

The present study also revealed that benzoate functions as an efficient and stable activator of the OER catalyzed by α-MnO_2 at neutral pH (Figure 2.2a). In PSII, six of the seven direct ligands of the Mn_4 cluster are carboxyl groups (Figure 2.1a).[1] Also, the carboxyl group of D1-Asp61 has been considered to act as a proton acceptor in the CPET in Kok cycle. This exclusive utilization of the carboxyl group is a distinct feature of this enzyme from others. For example, the ORR, the reverse reaction of the OER, is catalyzed by Cu and Fe coordinated by thiol, imidazolyl groups, or porphyrin nitrogen, but not by carboxyl groups.[51,52] Therefore, it appears that, in the course of evolution, the carboxyl residues were adapted by PSII because of their high durability against self-oxidation during the OER. The introduction of carboxyl groups represents an intriguing strategy to develop stable Mn-based OER catalysts that are highly active under neutral conditions.

2.4 Conclusions

In summary, the effects and the stability of the organic compounds in a synthetic counterpart of PSII have been analyzed. The comparison of energy diagram of the OER catalyzed by PSII and the synthetic counterpart suggested that imidazolyl groups are oxidized at the surface of α-MnO_2 to generate soluble Mn^{2+} ions *via* a proton-coupled multi-electron oxidation pathway, while both single and multi-electron oxidation reactions of D1-His332 are effectively inhibited in PSII. In addition, the presence of carboxyl groups, which is abundant around the Mn_4 cluster,[1] were found to stably facilitate the OER activity of α-MnO_2 by inducing the CPET reaction. These findings are expected to provide a new design rationale of organic ligands, which is crucial for the development of functional analogs of the Mn_4 cluster for efficient and stable water splitting at neutral pH.

References of Chapter 2

1. Y. Umena, K. Kawakami, J.-R. Shen and N. Kamiya, Crystal structure of oxygen-evolving photosystem II at a resolution of 1.9 Å. *Nature* **2011**, *473*, 55–61.
2. P. J. Nixon and B. A. Diner, Aspartate 170 of the photosystem II reaction center polypeptide D1 is involved in the assembly of the oxygen-evolving manganese cluster. *Biochemistry* **1992**, *31*, 942–948.
3. R. J. Debus, K. A. Campbell, D. P. Pham, A. M. A. Hays and R. D. Britt, Glutamate 189 of the D1 polypeptide modulates the magnetic and redox properties of the manganese cluster and tyrosine Y_Z in photosystem II. *Biochemistry* **2000**, *39*, 6275–6287.
4. H. A. Chu, A. P. Nguyen and R. J. Debus, Amino acid residues that influence the binding of manganese or calcium to photosystem II. 2. The carboxy-terminal domain of the D1 polypeptide. *Biochemistry* **1995**, *34*, 5859–5882.
5. H. J. Hwang, P. Dilbeck, R. J. Debus and R. L. Burnap, Mutation of arginine 357 of the CP43 protein of photosystem II severely impairs the catalytic S-state cycle of the H_2O oxidation complex. *Biochemistry* **2007**, *46*, 11987–11997.
6. D. R. Weinberg, C. J. Gagliardi, J. F. Hull, C. F. Murphy, C. A. Kent, B. C. Westlake, A. Paul, D. H. Ess, D. G. McCafferty and T. J. Meyer, Proton-coupled electron transfer. *Chem. Rev.* **2012**, *112*, 4016–4093.
7. F. Rappaport, M. Guergova-Kuras, P. J. Nixon, B. A. Diner and J. Lavergne, Kinetics and pathways of charge recombination in photosystem II. *Biochemistry* **2002**, *41*, 8518–8527.
8. M. Grabolle and H. Dau, Energetics of primary and secondary electron transfer in Photosystem II membrane particles of spinach revisited on basis of recombination-fluorescence measurements. *Biochim. Biophys. Acta, Bioenerg.* **2005**, *1708*, 209–218.

9. T. Shibamoto, Y. Kato, M. Sugiura and T. Watanabe, Redox potential of the primary plastoquinone electron acceptor Q_A in photosystem II from *Thermosynechococcus elongatus* determined by spectroelectrochemistry. *Biochemistry* **2009**, *48*, 10682–10684.

10. J. Yano and V. Yachandra, Mn_4Ca cluster in photosynthesis: Where and how water is oxidized to dioxygen. *Chem. Rev.* **2014**, *114*, 4175–4205.

11. N. Cox and J. Messinger, Reflections on substrate water and dioxygen formation. *Biochim. Biophys. Acta, Bioenerg.* **2013**, *1827*, 1020–1030.

12. A. Boussac, J.-L. Zimmermann, A. W. Rutherford and J. Lavergne, Histidine oxidation in the oxygen-evolving photosystem-II enzyme. *Nature* **1990**, *347*, 303–306.

13. B. J. Hallahan, J. H. A. Nugent, J. T. Warden and M. C. W. Evans, Investigation of the origin of the "S3" EPR signal from the oxygen-evolving complex of photosystem 2: the role of tyrosine Z. *Biochemistry* **1992**, *31*, 4562–4573.

14. A. Boussac and A. W. Rutherford, The origin of the split S_3 EPR signal in Ca^{2+}-depleted photosystem II: Histidine versus tyrosine. *Biochemistry* **1992**, *31*, 7441–7445.

15. J. Stubbe and W. A. van der Donk, Protein radicals in enzyme catalysis. *Chem. Rev.* **1998**, 98, 705–762.

16. M. L. Gilchrist, Jr., J. A. Ball, D. W. Randall and R. D. Britt, Proximity of the manganese cluster of photosystem II to the redox-active tyrosine Y_Z. *Proc. Natl. Acad. Sci. U. S. A.* **1995**, *92*, 9545–9549.

17. X.-S. Tang, D. W. Randall, D. A. Force, B. A. Diner and R. D. Britt, Manganese-tyrosine interaction in the photosystem II oxygen-evolving complex. *J. Am. Chem. Soc.* **1996**, *118*, 7638–7639.

18. N. Cox, M. Retegan, F. Neese, D. A. Pantazis, A. Boussac and W. Lubitz, Electronic

structure of the oxygen-evolving complex in photosystem II prior to O–O bond formation. *Science* **2014**, *345*, 804–808.

19. M. J. Russell and A. J. Hall, presented in part at Sixth International Congress on Carbon Dioxide Utilization, Breckenridge, Colorado, U. S. A., September **2001**.
20. K. Sauer and V. K. Yachandra, A possible evolutionary origin for the Mn_4 cluster of the photosynthetic water oxidation complex from natural MnO_2 precipitates in the early ocean. *Proc. Natl. Acad. Sci. U. S. A.* **2002**, *99*, 8631–8636.
21. R. M. McKenzie, The synthesis of birnessite, cryptomelane, and some other oxides and hydroxides of manganese. *Mineral. Mag.* **1971**, *38*, 493–502.
22. M. Singh, D. N. Thanh, P. Ulbrich, N. Strnadová and F. Štěpánek, Synthesis, characterization and study of arsenate adsorption from aqueous solution by α- and δ-phase manganese dioxide nanoadsorbents. *J. Solid State Chem.* **2010**, *183*, 2979–2986.
23. A. Yamaguchi, R. Inuzuka, T. Takashima, T. Hayashi, K. Hashimoto and R. Nakamura, Regulating proton-coupled electron transfer for efficient water splitting by manganese oxides at neutral pH. *Nat. Commun.* **2014**, *5*, 4256.
24. A. K. Covington, M. Paabo, R. A. Robinson and R. G. Bates, Use of the glass electrode in deuterium oxide and the relation between the standardized pD (pa_D) scale and the operational pH in heavy water. *Anal. Chem.* **1968**, *40*, 700–706.
25. K. Kamiya, K. Hashimoto and S. Nakanishi, Graphene defects as active catalytic sites that are superior to platinum catalysts in electrochemical nitrate reduction. *ChemElectroChem* **2014**, *1*, 858–862.
26. A. H. Wonders, T. H. M. Housmans, V. Rosca and M. T. M. Koper, On-line mass spectrometry system for measurements at single-crystal electrodes in hanging meniscus configuration. *J. Appl. Electrochem.* **2006**, *36*, 1215–1221.

27. E. Gileadi, *Electrode kinetics for chemists, chemical engineers, and materials scientists*. Wiley-VCH, New York, U. S. A., **1993**.

28. J. O'M. Bockris, Kinetics of activation controlled consecutive electrochemical reactions: Anodic evolution of oxygen. *J. Chem. Phys.* **1956**, *24*, 817–827.

29. T. Takashima, K. Hashimoto and R. Nakamura, Mechanisms of pH-dependent activity for water oxidation to molecular oxygen by MnO_2 electrocatalysts. *J. Am. Chem. Soc.* **2012**, *134*, 1519–1527.

30. T. Takashima, A. Yamaguchi, K. Hashimoto, H. Irie and R. Nakamura, In situ UV-vis absorption spectra of intermediate species for oxygen-evolution reaction on the surface of MnO_2 in neutral and alkaline media. *Electrochemistry* **2014**, *82*, 325–327.

31. W. P. Jencks, Requirements for general acid–base catalysis of complex reactions. *J. Am. Chem. Soc.* **1972**, *94*, 4731–4732.

32. W. M. Haynes, *CRC handbook of chemistry and physics*. CRC Press, Boca Raton, Florida, U. S. A., **2014**.

33. K. D. Dobson and A. J. McQuillan, In situ infrared spectroscopic analysis of the adsorption of aromatic carboxylic acids to TiO_2, ZrO_2, Al_2O_3, and Ta_2O_5 from aqueous solutions. *Spectrochim. Acta, Part A* **2000**, *56*, 557–565.

34. M. R. Das and S. Mahiuddin, Kinetics and adsorption behaviour of benzoate and phthalate at the α-alumina-water interface: Influence of functionality. *Colloids Surf., A* **2005**, *264*, 90–100.

35. S. Tunesi and M. A. Anderson, Surface effects in photochemistry: an in situ cylindrical internal reflection-Fourier transform infrared investigation of the effect of ring substituents on chemisorption onto titania ceramic membranes. *Langmuir* **1992**, *8*, 487–495.

36. K. Uchida and S. Kawakishi, Selective oxidation of imidazole ring in histidine residues by

the ascorbic acid – copper ion system. *Biochem. Biophys. Res. Commun.* **1986**, *138*, 659–665.

37. K. Uchida and S. Kawakishi, Ascorbate-mediated specific oxidation of the imidazole ring in a histidine derivative. *Bioinorg. Chem.* **1989**, *17*, 330–343.

38. X. Xing, X. Zhu, H. Li, Y. Jiang and J. Ni, Electrochemical oxidation of nitrogen-heterocyclic compounds at boron-doped diamond electrode. *Chemosphere* **2012**, *86*, 368–375.

39. S. Navaratnam and B. J. Parsons, Reduction potential of histidine free radicals: A pulse radiolysis study. *J. Chem. Soc., Faraday Trans.* **1998**, *94*, 2577–2581.

40. A. Harriman, Further comments on the redox potentials of tryptophan and tyrosine. *J. Phys. Chem.* **1987**, *91*, 6102–6104.

41. D. J. Vinyard, G. M. Ananyev and G. C. Dismukes, Photosystem II: The reaction center of oxygenic photosynthesis. *Annu. Rev. Biochem.* **2013**, *82*, 577–606.

42. H. Dau and I. Zaharieva, Principles, efficiency, and blueprint character of solar-energy conversion in photosynthetic water oxidation. *Acc. Chem. Res.* **2009**, *42*, 1861–1870.

43. M. H. V. Huynh and T. J. Meyer, Proton-coupled electron transfer. *Chem. Rev.* **2007**, *107*, 5004–5064.

44. B. Jagoda-Cwiklik, P. Slavíček, L. Cwiklik, D. Nolting, B. Winter and P. Jungwirth, Ionization of imidazole in the gas phase, microhydrated environments, and in aqueous solution. *J. Phys. Chem. A* **2008**, *112*, 3499–3505.

45. C. P. Kelly, C. J. Cramer and D. G. Truhlar, Aqueous solvation free energies of ions and ion-water clusters based on an accurate value for the absolute aqueous solvation free energy of the proton. *J. Phys. Chem. B* **2006**, *110*, 16066–16081.

46. A. A. Isse and A. Gennaro, Absolute potential of the standard hydrogen electrode and the

problem of interconversion of potentials in different solvents. *J. Phys. Chem. B* **2010**, *114*, 7894–7899.

47. H. Walba and R. W. Isensee, Acidity constants of some arylimidazoles and their cations. *J. Org. Chem.* **1961**, *26*, 2789–2791.

48. G. J. Kavarmos, *Fundamentals of photoinduced electron transfer*. VCH, Weinheim, New York, U. S. A., **1993**.

49. C. A. Schroeder, E. Pluhařová, R. Seidel, W. P. Schroeder, M. Faubel, P. Slavíček, B. Winter, P. Jungwirth and S. E. Bradforth, Oxidation half-reaction of aqueous nucleosides and nucleotides via photoelectron spectroscopy augmented by ab initio calculations. *J. Am. Chem. Soc.* **2015**, *137*, 201–209.

50. P. E. M. Siegbahn, Water oxidation mechanism in photosystem II, including oxidations, proton release pathways, O–O bond formation and O_2 release. *Biochim. Biophys. Acta, Bioenerg.* **2013**, *1827*, 1003–1019.

51. S. Yoshikawa and A. Shimada, Reaction mechanism of cytochrome *c* oxidase. *Chem. Rev.* **2015**, *115*, 1936–1989.

52. S. A. Roberts, A. Weichsel, G. Grass, K. Thakali, J. T. Hazzard, G. Tollin, C. Rensing and W. R. Montfort, Crystal structure and electron transfer kinetics of CueO, a multicopper oxidase required for copper homeostasis in *Escherichia coli*. *Proc. Natl. Acad. Sci. U. S. A.* **2002**, *99*, 2766–2771.

Chapter 3.

Mechanistic Investigation of Highly-Active Manganese Oxide Nanoparticle Water Oxidation Catalysts

3.1 Introduction

In this Chapter, maximization of the multi-electron-transfer OER activity of Mn oxides by the introduction of structural distortion to the Mn oxide crystals themselves was investigated.

In Chapter 2, it was found that the introduction of organic acid ligands can be a viable strategy to stably facilitate the OER activity of Mn oxides. However, if the stabilization of Mn^{3+} can be achieved only by the consideration of crystal structures, the selectivity problems will no longer exist. Also, it is noted again that, if charge accumulation processes become no longer the RDS, it will be important to optimize the energetics related to the bonding structure changes according to the existing theories.

The comparison of the OER activity of Mn oxides with different bulk crystal structures in neutral conditions was conducted.[1,2] However, Stahl *et al.* reported that the OER activity trend at neutral pH is different in an electrochemical condition from that in a photochemical condition using $[Ru(bpy)_3]^{2+}$ as the photo-sensitizer and $S_2O_8^{2-}$ as the electron acceptor, suggesting that the comparison of Mn oxides with different crystal structures is not straightforward.[2] Nevertheless, Dismukes *et al.* reported their successful identification of corner-shared $Mn^{3+}O_6$ sites with D_{3d} ligand-field symmetry as the site responsible for the OER activity.[3] This report is in harmony with the reports by Takashima *et al.* about the importance of Mn^{3+}, and also with the report about the importance of layer vacancies by Suib *et al.*[4] and the one about 3.45 Å Mn–Mn distances by Dau *et al.*[3,5]

Also, phosphorous-derived Mn catalysts were investigated by Nam *et al.* as OER catalysts. The phosphorous-derived Mn catalysts had asymmetric ligand field geometry around the Mn atoms and displayed superior performance to oxide catalysts.[6] The reason for the higher OER activity was assessed by measuring the applied inner pressure and local pair distribution functions of the Mn^{3+} states. Computational analysis revealed that, although high inner pressure was required for the increased catalytic activity, Jahn-Teller distortion occurred freely at the Mn^{3+} sites in the Mn^{2+}–O rocksalt structure. Namely, the activity enhancement was explained by the stabilization of Mn^{3+} by structural flexibility introduced into the ligand field of the Mn atoms.[6]

Nam *et al.* also developed sub-10-nm-sized partially-oxidized Mn oxide NPs, which exhibited higher activity at neutral pH than Co–phosphate (Co–Pi) amorphous films.[7] Additionally, a clear dependency of the onset potential for the OER on the particle size was observed, and the activity of the nanosized Mn oxide compounds was superior to bulk counterparts.[7,8]

However, the reason for the enhanced activity of sub-10-nm-sized Mn oxide NPs, which may lead to a new design principle of Mn-based OER catalysts, was not clear. Here, it was anticipated that Mn^{3+} can be generated at lower potential in Mn oxide NPs than in bulk counterparts because there are Mn atoms with a distorted ligand field because of the large ratio of the number of the surface atoms to the total atoms, getting rid of the degenerated e_g orbitals.

To understand the effects and determine the OER mechanism catalyzed by nanosized Mn oxides, *in-situ* spectroscopic and electrokinetic analyses were comprehensively conducted. Specifically, from the EPR, *in-situ* XANES, UV–vis, and Raman analysis, a new catalytic cycle different from that of conventional bulk Mn oxides was demonstrated.

3.2 Experimental Methods

3.2.1 Materials and Basic Characterization

Materials

$Mn(CH_3COO)_3 \cdot 2H_2O$ (99%), 1-octadecene (90%), myristic acid ($CH_3(CH_2)_{12}COOH$) (99%), decanol ($CH_3(CH_2)_9OH$), $Na_2HPO_4 \cdot 7H_2O$ (ACS reagent, 98.0–102.0%), and $NaH_2PO_4 \cdot 2H_2O$ (99.0%) were purchased from Sigma Aldrich and used as received without further purification. glass coated with fluorine-doped tin oxide (FTO, TEC-8) with the surface resistivity of 15 Ω sq^{-1} was manufactured by Pilkington Company.

Synthesis of the Manganese Oxide Nanoparticles

The MnO NPs were synthesized by one of the conventional thermal decomposition methods, the hot injection method.[7] The first step to synthesize monodisperse 10-nm-sized MnO NPs was to make two types of solutions; one was 1 mmol of $Mn(CH_3COO)_3$ and 2 mmol of myristic acid in 20 mL of octadecene and the other was the mixture of 3 mmol of decanol and 1 mL of octadecene. These two separate mixtures were degassed at 110 ℃ for 2 hours with vigorous stirring. After 2 hours of degassing, the solution of $Mn(CH_3COO)_3$ and myristic acid was heated up to 295 ℃ under argon atmosphere. When the temperature reached 295 ℃, the mixture of decanol and octadecene was injected rapidly into the solution of $Mn(CH_3COO)_3$ and myristic acid to induce the burst nucleation along with super-saturation. The mixture was maintained at 295 ℃ for 30 minutes. During the reaction, the color changes from clear yellow to dark brown. The dark brown solution was then cooled to room temperature.

Preparation of Electrodes

After the synthesis of the solution with the MnO NPs, the solution, acetone, and toluene were mixed in the volume ratio of 1:1:1 and centrifuged to obtain the precipitate of the MnO NPs. Purification step was repeated several times by re-inserting equivalent amount of acetone and toluene. After this purification step, the precipitate was dispersed in hexane. Then the 40μL of MnO NPs solution was spin-coated onto the FTO substrates at the spin rate of 2000 rpm and the holding time of 10 seconds. The thickness of the MnO NP film spin-coated on the FTO substrates was controlled by the volume ratio of the initial dark brown MnO NP solution to hexane. To eliminate the surfactant (myristic acid) on the surface of the MnO NPs, which can inhibit the access of water molecules to active sites, the spin-coated film on the FTO substrates were dipped in a diluted NH_4OH solution for 1 hour and annealed at 250 ℃ for 1 hour.

Scanning Electron Microscopy

The morphology of the MnO NPs on the FTO substrates was characterized by high-resolution scanning electron microscopy (SEM) (Supra 55VP, Carl Zeiss). After deposition of the MnO NPs, the substrate was gently rinsed in deionized water at least 3 times and dried with nitrogen gas. Images were taken with an acceleration voltage of 2 kV, and EDX spectra with a 15 kV.

Transmission Electron Microscopy

TEM images and selected area electron diffraction (SAED) patterns were obtained using a high-resolution transmission electron microscope (JEM-3000F, JEOL) with the acceleration voltage of 300 kV. To prepare the samples for TEM, the MnO NPs dispersed in hexane were dropped on the TEM grid and dried in air.

3.2.2 Electrochemical Measurement

General Conditions

All electrochemical experiments were conducted in a three-electrode system. Ag/AgCl/3 M NaCl and Pt were used as a reference electrode and a counter electrode, respectively. Electrochemical tests were carried out at room temperature using a potentiostat. The electrode potential versus Ag/AgCl/3 M NaCl was converted to the SHE scale, using the following equation: E(SHE) = E(Ag/AgCl/3 M NaCl) + 0.197 V. Additionally, overpotential values were calculated by the difference between the iR-corrected potential ($V = V_{applied} - iR$) and the thermodynamic potential of water oxidation at a specified pH. 500 mM phosphate buffer (pH 7) was used as the electrolyte.

Cyclic Voltammetry

Prior to every electrochemical experiment, the solution resistance was measured. All the data were iR-compensated.

3.2.3 Electron Paramagnetic Resonance Measurement

EPR measurement was performed using a Bruker EMX/Plus spectrometer equipped with a dual mode cavity (ER 4116DM). The temperature was controlled using a liquid He quartz cryostat (ESR900, Oxford Instruments) with a controller of temperature and gas flow (ITC503, Oxford Instruments). The experimental conditions were as follows. Microwave frequency: 9.64 GHz (perpendicular mode), 9.4 GHz (parallel mode). Modulation amplitude: 10 G. Modulation frequency: 100 kHz. Microwave power: 0.94 mW (perpendicular mode), 5.0 mW (parallel mode) Temperature: 5.7 K. 10 scans were added for each spectrum. All the samples were loaded on the FTO substrates (2 cm × 3 cm). After each bulk electrolysis at designed potentials, catalysts were

collected by a blade and then transferred to EPR tube immediately. Finally, the EPR tube was frozen and stored at 77 K in liquid nitrogen immediately.

3.2.4 *In-situ* Spectroscopic Measurement

In-situ XAS

In-situ Mn K-edge XAS spectra of the MnO electrocatalyst, XANES, and EXAFS, were collected on the BL10C beam line (WEXAFS) at the Pohang Light Source (PLS-II) with top-up mode operation under a ring current of 350 mA at 3.0 GeV. From the high-intensity X-ray photons of the multipole wiggler source, monochromatic X-ray beams could be obtained using a liquid-nitrogen-cooled double-crystal monochromator (Bruker ASC) with the available *in-situ* exchange in the vacuum between a Si(111) and Si(311) crystal pair. The Si(111) crystal pair was used for Mn K-edge XAS measurement (absorption edge energy: 6539 eV). Applied voltage-dependent Mn K-edge XAS data during the OER was recorded using a home-made electrochemical cell for *in-situ* measurement with polyimide film windows, in fluorescence mode with a passivated implanted planner silicon detector. Higher-order harmonic contaminations were eliminated by detuning to reduce the incident X-ray intensity by ~30%. Energy calibration was simultaneously carried out for each measurement with reference Mn foil placed in front of the third ion chamber. The data reductions of the experimental spectra to normalized XANES and Fourier-transformed radial distribution functions were performed through the standard EXAFS procedure.

In-situ UV–vis Spectroscopy

In-situ UV–vis absorption spectra were obtained in diffuse transmission mode using a UV–vis spectrometer (UV-2550, Shimazu) equipped with a multi-purpose large-sample compartment and

a built-in integrating sphere (MPC-2200, Shimadzu). For *in-situ* acquisition of spectra, an electrode mounted in an electrochemical cell was placed in front of the integrating sphere to collect diffused transmission light.

In-situ Raman Spectroscopy

In-situ Raman spectra were obtained using a Raman microscope (SENTERRA, Bruker) and a tailor-made electrochemical cell. For the measurement, 532-nm laser was irradiated through an optical window and the electrolyte onto the surface of working electrodes.

3.3 Results and Discussion

The synthesis of the MnO NPs and preparation of electrodes were performed following a previously reported method.[7] As shown in Figure 3.1a and b, monodispersed 10-nm-sized MnO NPs were successfully synthesized and loaded onto FTO substrates. The thickness of the MnO NP films ranged from 70 to 600 nm (Figure 3.1c–f) and was precisely controlled using spin coating.

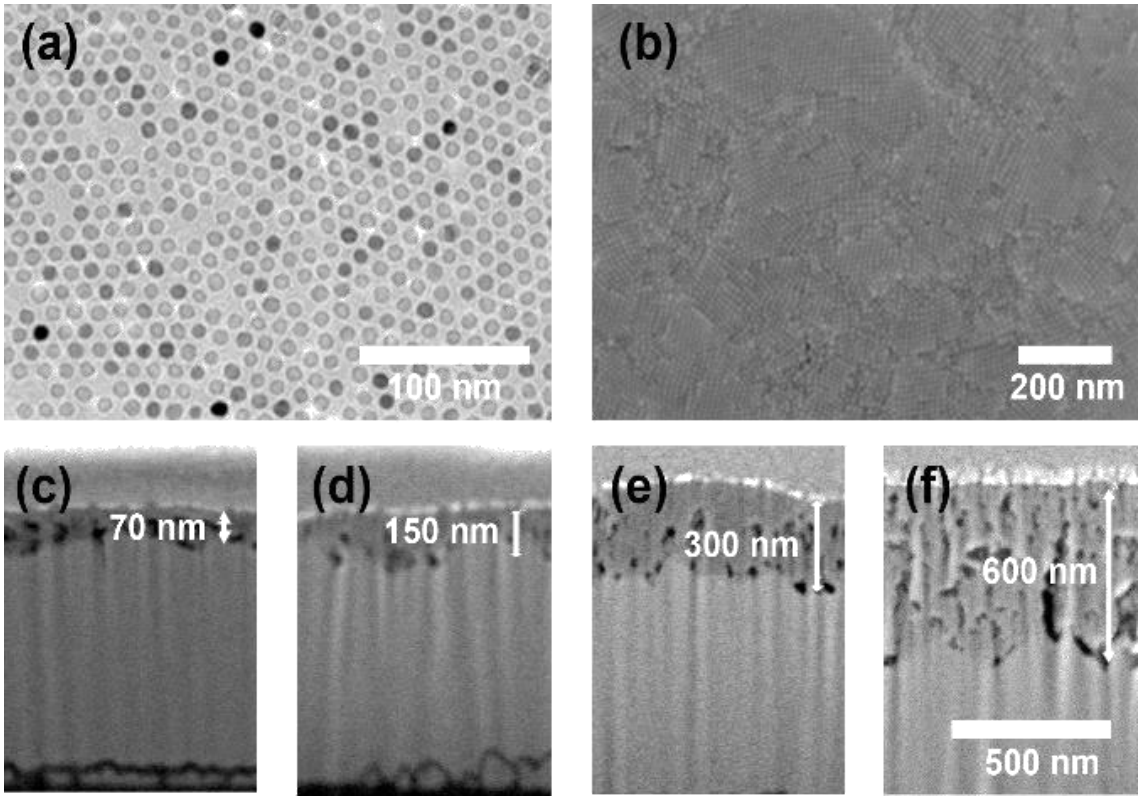

Figure 3.1 | Electron microscopic images of the MnO NP films. (a) TEM image of synthesized MnO NPs and (b) plane and (c–f) cross-sectional SEM images of the MnO NP films on FTO substrates.

The electrode kinetics of the OER by the MnO NPs were analyzed using various electrochemical techniques. Thickness-dependent OER activity was evaluated by cyclic voltammetry (CV) in 0.5 M phosphate buffer at pH 7. To minimize the (potential) contribution of non-Faradaic current, all CV curves were polarization-corrected.[9] As shown in Figure 3.2a, the overpotential at the current density of 5 mA cm^{-2} was 610, 560, 530, and 550 mV for the 70-, 150-, 300-, and 600-nm-thick films, respectively. It was found that the 300-nm-thick films exhibited the highest OER performance at 5 mA cm^{-2} and that, as the film thickness exceeded 300 nm, the catalytic activity was markedly reduced. The decrease in catalytic activity for the 600-nm film was attributed to the increased charge transport limitations, which were more dominant than the increase in active sites and resulted in the saturation of the catalytic current.

Tafel plots for each of the prepared films were obtained from the polarization-corrected CV curves. The Tafel slopes measured using 70-, 150-, 300-, and 600-nm-thick electrodes were 82.6, 75.5, 70.1, and 78.2 mV dec^{-1}, respectively (Figure 3.2b). For the electrochemical OER, the current-potential relationship was described by Equation 3.1, where i_0, α, F, E°, and b are the exchange current density, transfer coefficient, Faraday constant, thermodynamic equilibrium potential, and Tafel slope, respectively. Additionally, the Tafel slope (b) can be expressed as being inversely related to the transfer coefficient (Equation 3.2).[10,11]

$$i = i_0 \exp\left\{-\frac{a(E - E^{\circ})F}{RT}\right\} \tag{3.1}$$

$$b = \left(\frac{\partial E}{\partial \log i}\right) = \frac{2.3RT}{aF} \tag{3.2}$$

The Tafel slopes of 70–80 mV dec^{-1} for the prepared MnO NP films corresponded to 2.3 RT/F, which indicates that the transfer coefficient was 1 and that a reversible one-electron transfer process occurred prior to the RDS.[11–13]

The pH dependence of the catalytic activity of the MnO NPs was further examined under neutral conditions (Figure 3.2c and 3.3). The potentials at the current density of 1 mA cm^{-2} were measured at from pH 6.5 to 8.0 for each film thickness. As shown in Figure 3.2c, a linear relationship between pH and the measured potential was observed. The slopes were estimated to be −84.1, −73.8, −71.8, and −76.8 mV pH^{-1} for the 70-, 150-, 300-, and 600-nm-thick MnO NP films, respectively. As was observed for the Tafel slopes, the slopes had similar values of approximately 70–80 mV pH^{-1} regardless of the film thickness. In electrochemical rate law, the reaction order of proton is defined as $-(\partial \log j/\partial \mathrm{pH})_{E,T,P}$. Thus, using the values of the Tafel slopes and pH-dependent potential changes, the reaction order of proton can be derived from the following partial differential equation:[10,11]

$$\left(\frac{\partial E}{\partial \mathrm{pH}}\right)_{j,T,P} = -\left(\frac{\partial E}{\partial \log j}\right)_{\mathrm{pH},T,P}\left(\frac{\partial \log j}{\partial \mathrm{pH}}\right)_{E,T,P} \tag{3.3}$$

As shown in Figure 3.2e, the proton reaction order for each thickness of the film was maintained as −1, which indicated inverse first-order dependence of the reaction rate on the proton activity (Figure 3.2e). The dependence of the current density on the phosphate concentration was also evaluated at various water oxidizing potentials. A zeroth-order dependence on the phosphate concentration was observed at each applied potential (Figure 3.2d). Based on the experimental results of the electrokinetic analyses, the overall electrochemical rate law for the OER by the MnO NPs was derived, as follows:[10]

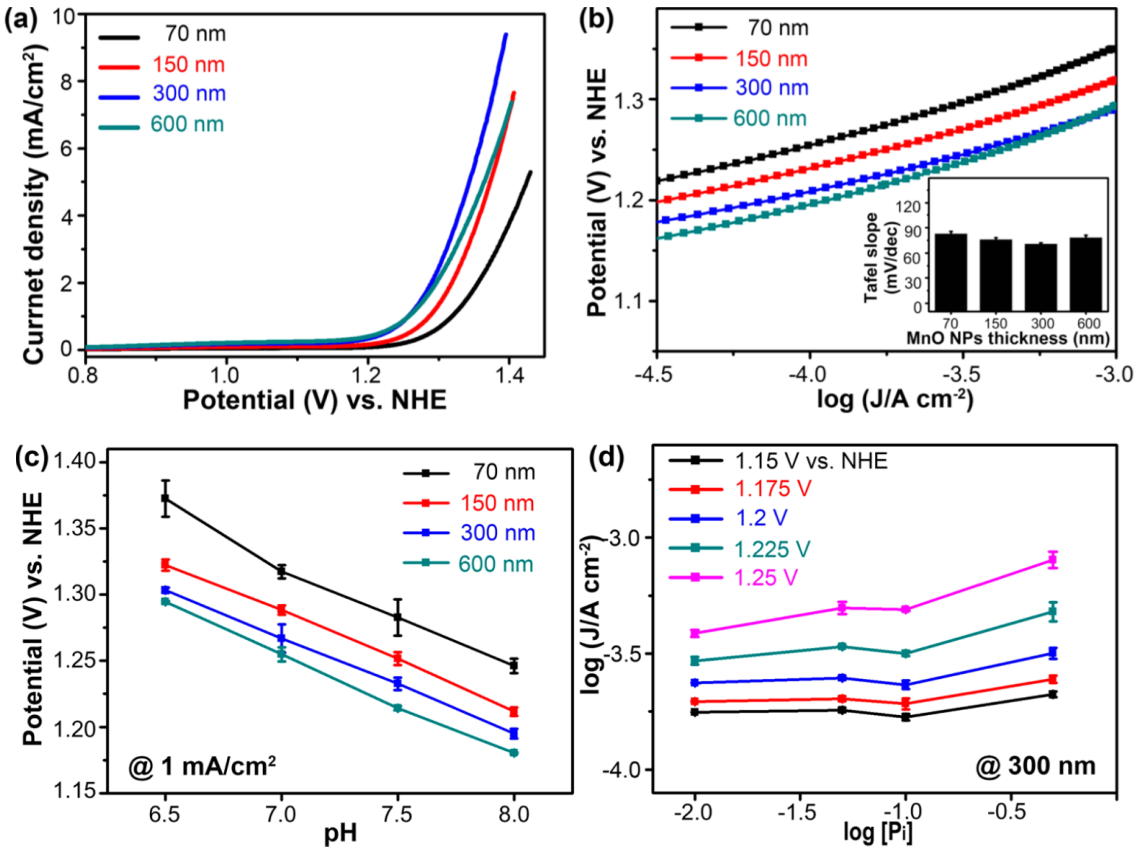

Figure 3.2 | Electrokinetic analysis of the MnO NP films. (a) Polarization-corrected CV curves, (b) Tafel plots near the onset potential, (c) pH dependency over a neutral pH range, and (d) dependency of current density on phosphate concentration.

Table 3.1 | Summary for the estimated proton reaction orders of the MnO NP films of various thickness.

	pH dependence of overpotential / mV pH^{-1}	Tafel slope / mV dec^{-1}	Reaction order for proton
70 nm	−84.1	82.6	−1.02
150 nm	−73.8	75.5	−0.98
300 nm	−71.8	70.1	−1.02
600 nm	−76.8	78.2	−0.98

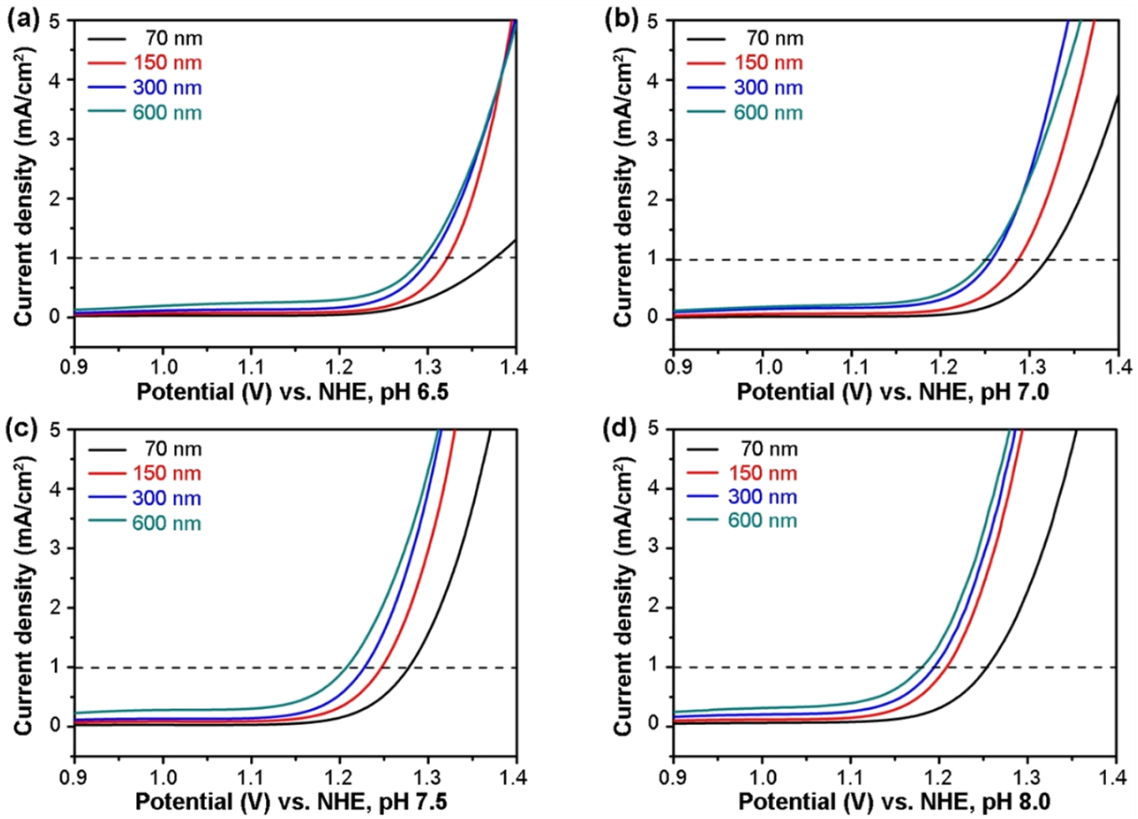

Figure 3.3 | Polarization-corrected CV curves for the MnO NP films of various thicknesses. (a) pH 6.5, (b) pH 7, (c) pH 7.5, and (d) pH 8.

$$j = k_0(a_{H^+})^{-1}\exp\left(\frac{FE}{RT}\right) \tag{3.4}$$

Equation 3.4 is consistent with a mechanistic sequence involving a quasi-equilibrium reversible $1e^-/1H^+$ transfer step followed by the RDS.[10] Notably, the electrochemical behavior of the MnO NPs under neutral conditions is clearly distinct from previously reported Mn-based catalysts, which typically exhibit Tafel slopes of 100–120 mV dec^{-1} at neutral pH. For example, commercially available micron-sized Mn oxide compounds, MnO_2, Mn_2O_3, and Mn_3O_4, show Tafel slopes of 120 mV dec^{-1} and do not exhibit pH dependency.[6] This is also true in the results in Chapter 2. Similar electrochemical data was obtained for the phosphorous-containing materials

$Mn_3(PO_4)_2 \cdot 3H_2O$ and $Li_2MnP_2O_7$, which showed Tafel slopes of ~120 mV dec^{-1}.[6,14] Moreover, amorphized Mn oxides also show Tafel slopes of ~120 mV dec^{-1}.[15]

Theoretically, a Tafel slope of 120 mV dec^{-1} means that the transfer coefficient (α) in Equation 3.2 is equal to 1/2, which indicates that one-electron oxidation was predicted to be the RDS without a quasi-equilibrium step. Consistent with this speculation, the RDS in the OER by Mn oxides was experimentally identified by *in-situ* spectroscopic analysis as the redox process from Mn^{2+} to Mn^{3+}.[16,17] Therefore, the distinctive electrokinetic behavior of the MnO NPs may be the reason for their superior OER activity compared to previously reported Mn catalysts. In addition, the data obtained here in the analysis of electrokinetics did not change as the film thickness increased, indicating that the established electrochemical law can be commonly applied to the reaction kinetics of the MnO NPs irrespective of film thickness. For this reason, 300-nm-thick MnO NP films were used for further mechanistic studies.

In the CV curves, unique redox characteristics of the MnO NPs were observed. Specifically, two distinct redox waves appeared at 0.68 and 1.07 V vs. SHE, and both redox waves displayed pH-dependent shifts between pH 7 and 8 (Figure 3.4a). The peak positions of the first and second redox waves shifted at the rate of −77 and −61 mV pH^{-1}, respectively. As these values are similar to 59 mV dec^{-1}, stepwise proton-coupled oxidations likely occurred before and during the OER. The pH-dependent behavior of the MnO NPs was analogous to that of Co–Pi catalysts under neutral conditions.[18,19] The redox and onset potentials for the OER catalyzed by Co–Pi are shifted negatively at increasing pH. The sequential Co redox waves exhibit a similar pH dependency as those of the MnO NPs.[18,19]

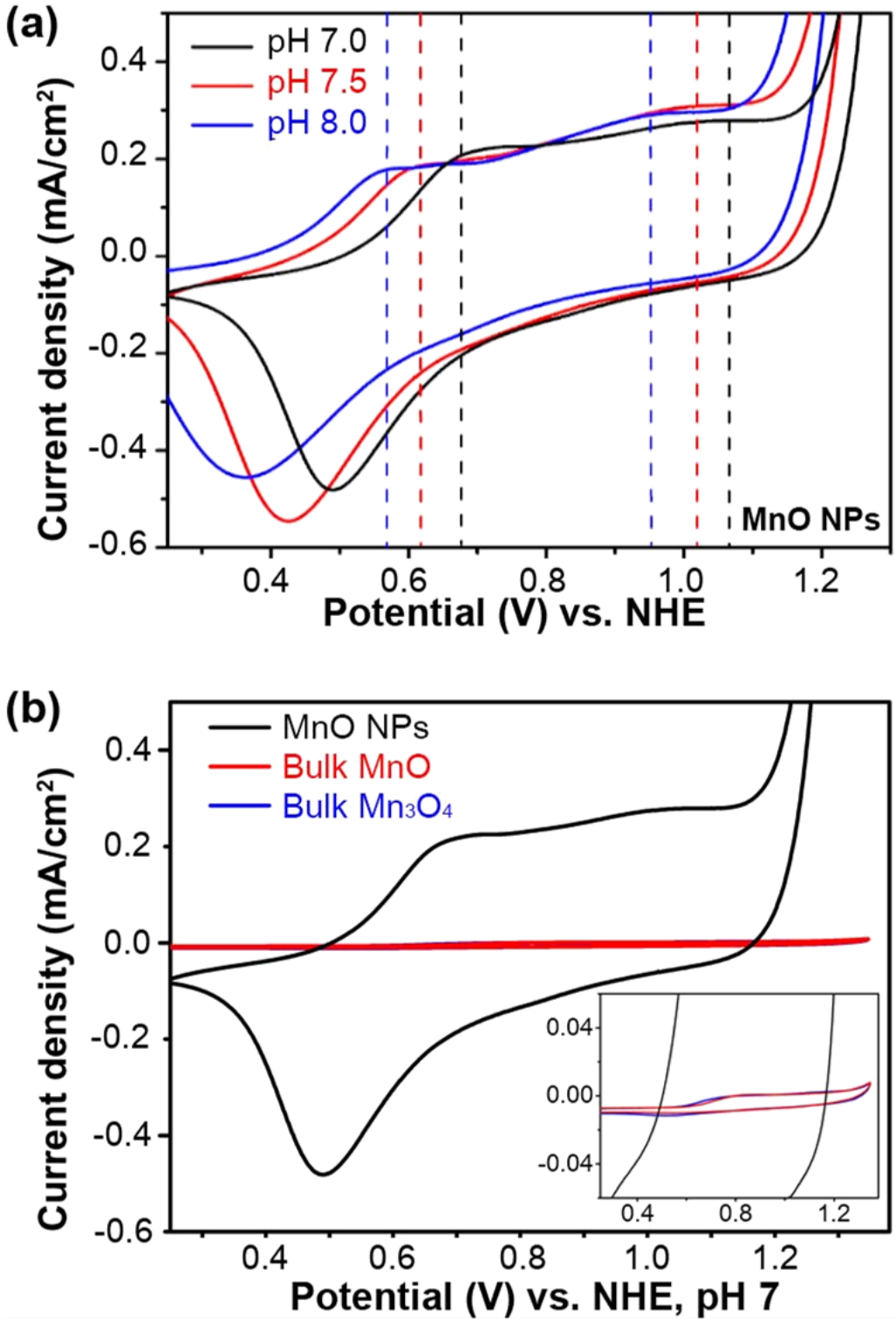

Figure 3.4 | Comparison of the CV curves of the MnO NPs and bulk Mn oxide compounds. (a) pH-dependent redox peak shift in the CV curve of the MnO NPs and (b) comparison of the redox behavior between bulk Mn_3O_4, bulk MnO, and the MnO NPs.

In addition to the redox waves, the onset of Faradaic OER current, which was initiated immediately after the second redox process, was also shifted (Figure 3.4a). In contrast, the bulk Mn oxides, MnO and Mn_3O_4, exhibited only non-Faradaic current of several μA cm^{-2} (Figure 3.4b). These electrochemical behaviors were consistent with the previous study reporting that the onset potential of the OER by conventional Mn oxides, such as MnO_2, remains unchanged at pH < 9.[16] Therefore, the sequential proton-coupled redox reactions appear to be specific for the MnO NPs.

To shed light on the redox chemistry of the MnO NPs, spectroscopic analyses were performed to detect reaction intermediates. Continuous wave EPR spectroscopy was utilized to monitor the Mn oxidation state of the MnO NPs. The perpendicular and parallel mode EPR spectra of the MnO NPs at the four applied potentials (0.4, 0.75, 1.1, and 1.3 V vs. SHE) are presented in Figure 3.5a. The EPR spectrum of the as-prepared MnO NPs exhibited characteristic Mn^{2+} (S = 5/2, g_{eff} ~ 2) and Mn^{3+} (S = 2, g_{eff} ~ 8.2) signals with a six-line ^{55}Mn (I = 5/2, 100% abundance) hyperfine splitting in the perpendicular and parallel modes, respectively.

Next, the intensity of the Mn^{2+}/Mn^{3+} spectra on the MnO NPs above and below the Mn redox potentials was quantitatively compared. At potentials near the first redox wave, the Mn^{2+} signals continuously decreased, whereas the Mn^{3+} signals were enhanced (Figure 3.5b). The observed spectral changes and obtained electrochemical data imply that the first redox wave corresponds to Mn^{2+}–OH_2 → Mn^{3+}–OH.[20] The protonation states of the surface species on the Mn active sites was estimated based on the pK_a values of the hydroxyl groups on Mn^{2+} and Mn^{3+} reported as 10.6 and 0.7, respectively.[20,21] At potentials above the second redox wave, the Mn^{2+} signals were no longer detected and the Mn^{3+} signals were slightly decreased (Figure 3.5b). According to a previous EPR study, Mn^{5+} species in a Mn complex can be detected by the signals at g ~ 8.5 in

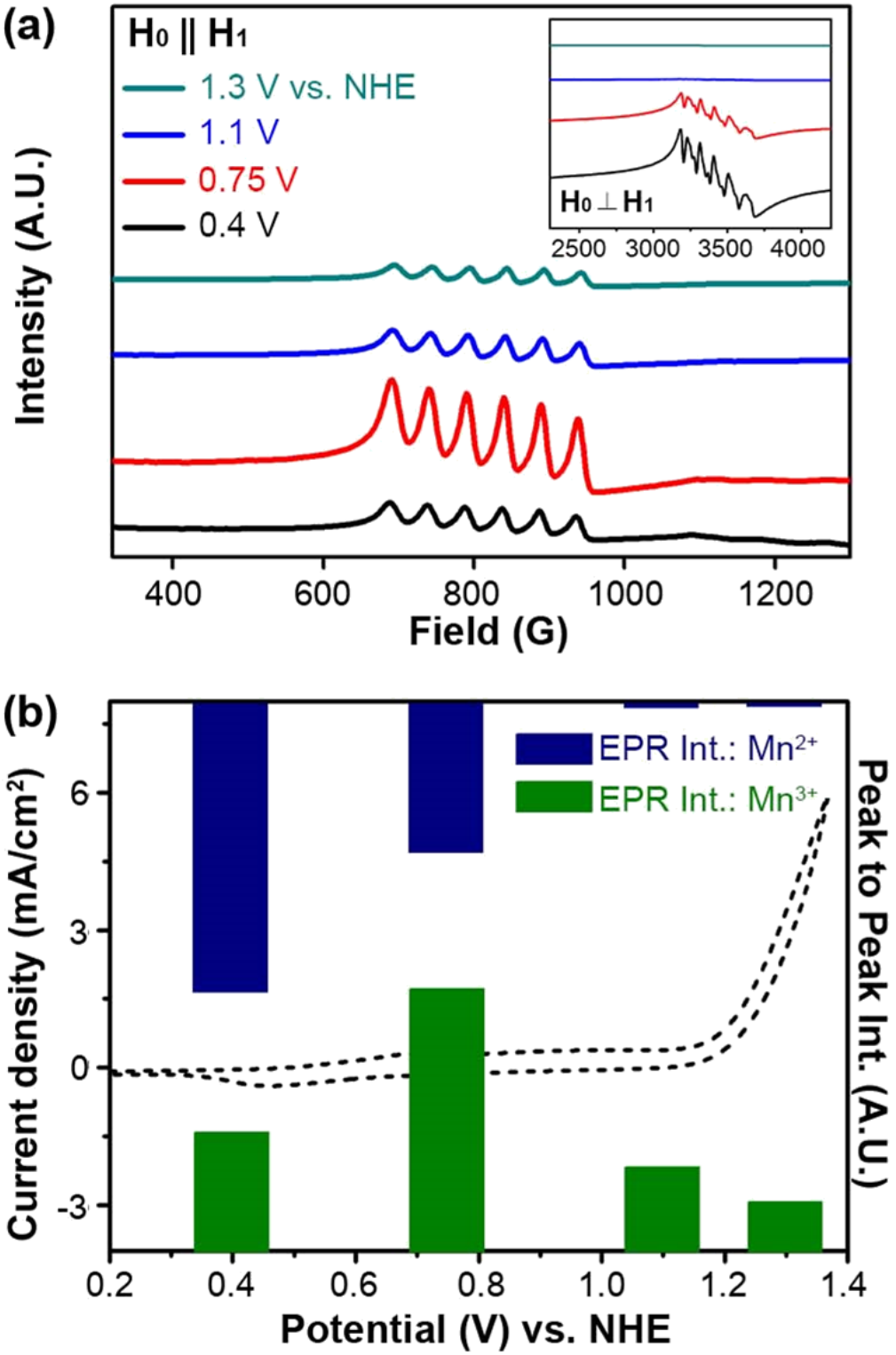

Figure 3.5 | Mn valency change during water oxidation catalysis measured by EPR spectroscopy. (a) Parallel mode X-band continuous wave EPR spectra (Inset: perpendicular mode continuous wave EPR spectra); (b) peak to peak EPR intensity.

the parallel mode;[22] however, such signals were not observed in the present study. In addition, although Mn^{4+} species displayed an EPR signal at g ~ 4.3 in the perpendicular mode, it was difficult to directly capture Mn^{4+} species because of the difficulty of determining the accurate zero field splitting value and rapid decay of reaction intermediates.[23,24] Thus, the present results indirectly support the conclusion that higher Mn valency is generated during catalysis.

The existence of Mn^{4+} or Mn^{5+} species during catalysis was further supported by the results of *in-situ* XANES analysis. For the analysis, pre-electrolysis was conducted at constant potentials to achieve a catalytic steady state. As expected, a clear positive shift was observed in the Mn K-edge spectra with an increase in the applied potential. The average Mn oxidation state was calculated using the spectra of the reference Mn oxide compounds (Figure 3.6, right inset). The oxidation states in the absence of an applied potential (or at the initial state) had average values of approximately 2.7, indicating that the valency of Mn was a mixture of Mn^{2+} and Mn^{3+}. At 0.4 V vs. SHE, the average oxidation state was slightly reduced. This decline was attributed to the partial reduction of Mn on the surface of the MnO NPs, in accordance with the negative current observed at 0.4 V vs. NHE in the CV curves (Figure 3.4a). Over the open circuit potential, a positive shift was observed in the Mn K-edge spectra. The Mn oxidation states were estimated to be 3.21 and 3.46 at 1.3 and 1.4 V vs. SHE, respectively (Figure 3.6).

The unique redox change from Mn^{2+} to Mn^{4+} *via* the formation of Mn^{3+} was verified by *in-situ* Raman spectroscopy. Raman spectra of the MnO NPs measured during electrolysis at constant potentials are shown in Figure 3.7. In the initial state, characteristic Mn^{2+}–O stretching vibration (A_g) and Mn^{3+}–O stretching (E_g) modes were observed as broad shoulder bands around 640 and 575 cm^{-1}, respectively.[25,26] As the applied potential increased to 1.05 V vs. NHE, which was the

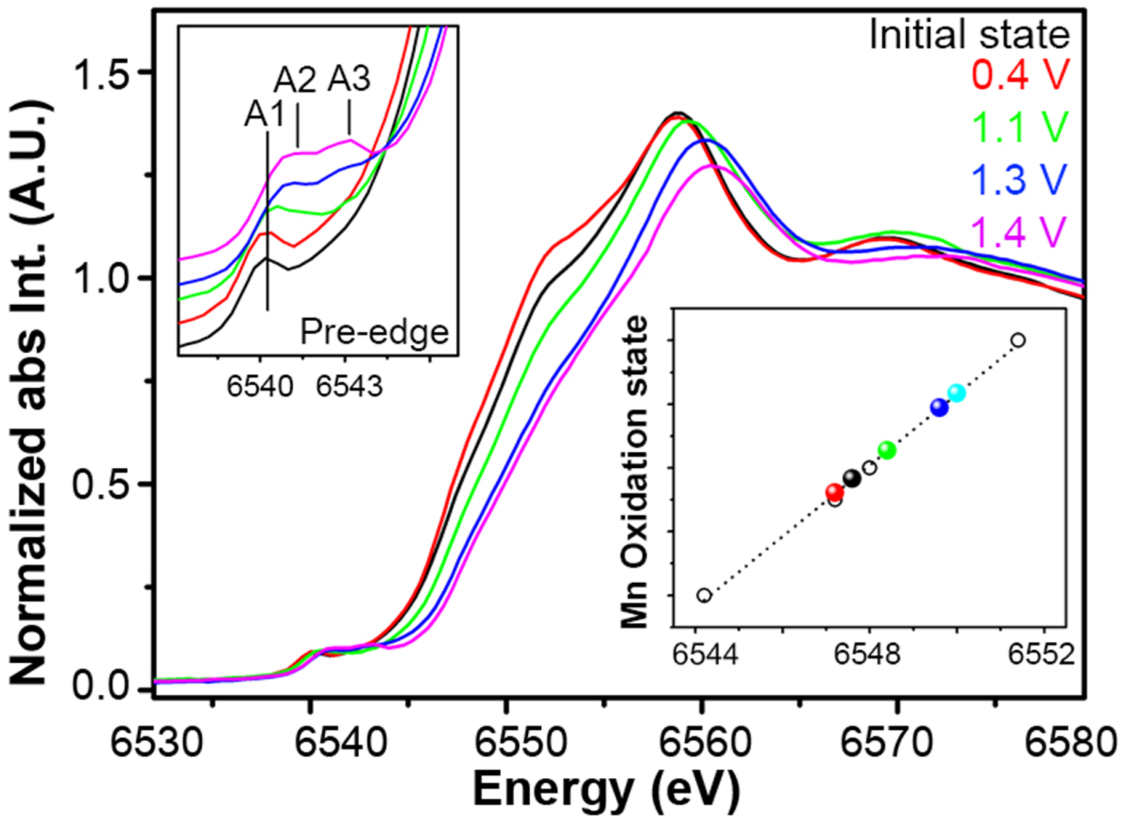

Figure 3.6 | Mn K-edge XANES spectra, and the average oxidation state of Mn demonstrating oxidation of Mn to higher valency. Inset: enlarged view of the pre-edge region (left) and estimated average oxidation state of Mn (right).

potential at which the OER was initiated, new Raman peaks appeared at approximately 555 and 480 cm^{-1}, with a corresponding decrease in intensity of the Mn^{3+}-related bands.[25,27] In addition, the Raman shift values and relative intensities of the generated peaks were well matched with the stretching vibration of Mn^{4+}–O species.[25] The reversibility of the Raman spectra was also confirmed (Figure 3.8). These observations therefore further demonstrated that the MnO NPs undergo a sequential redox change to form active Mn^{4+} species.

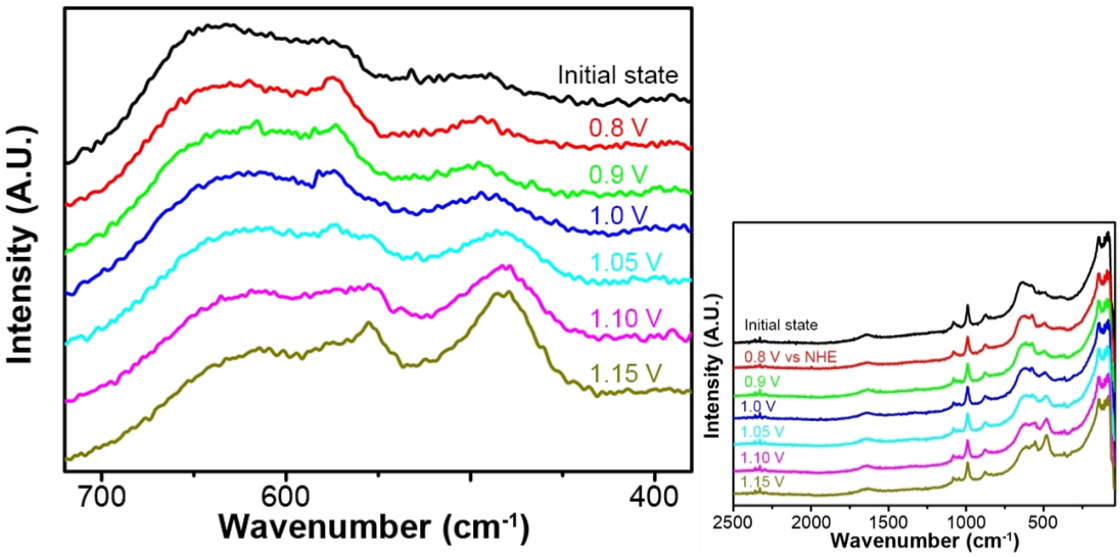

Figure 3.7 | *In-situ* Raman spectra of the MnO NPs. All spectra were collected during bulk electrolysis at the indicated potentials. Left: enlarged view. Right: overall data.

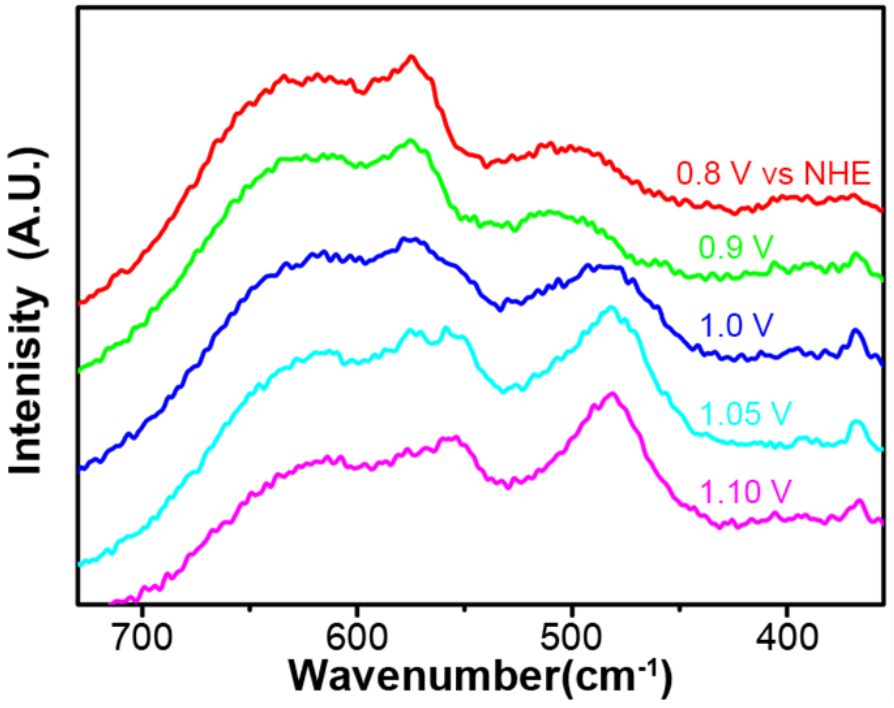

Figure 3.8 | *In-situ* Raman spectra of the MnO NPs in the reverse scan (at decreasing potentials). All spectra were collected during bulk electrolysis at the indicated potentials. Spectral changes in Figure 3.7 exhibited reversibility. Broad shoulder bands at around 640 and 575 cm^{-1} were observed again and peaks at approximately 555 and 480 cm^{-1} assigned to the stretching vibration of Mn^{4+}–O species disappeared.

The generated reaction intermediates were further identified by *in-situ* diffuse transmission UV–vis analysis. Spectral changes of the MnO NP electrodes caused by the catalytic reaction were monitored at pH 7 between 0.8 and 1.3 V vs. SHE in 0.1 V increments. To evaluate the Mn species formed on the surface of the MnO NPs, differential spectra at each potential by subtraction of the spectra obtained at 0.8 V were additionally obtained (Figure 3.9a and 3.10). Initially, the MnO NPs exhibited two bands in the UV regions at approximately 350 and 380 nm, corresponding to $O^{2-} \rightarrow Mn^{2+}$ and $O^{2-} \rightarrow Mn^{3+}$ ligand-to-metal charge transfer, respectively, along with several weak peaks originating from d-d transitions in the visible region.[28] As shown in Figure 3.9a, upon increasing the applied potentials at 0.1 V increments, two distinct absorption bands in the regions of 400 nm (ΔAbs_{400}) and 600 nm (ΔAbs_{600}) were identified. ΔAbs_{400} showed relatively sharp features, whereas ΔAbs_{600} had a broad and wide shoulder.

The origins of the observed redox peaks were assigned based on the peak characteristics and results of previous studies. Mn^{3+} in Mn_3O_4 nanoparticles reportedly exhibit $O^{2-} \rightarrow Mn^{2+}$ (210–250 nm) and $O^{2-} \rightarrow Mn^{3+}$ (350–390 nm) charge transfer transitions and d-d crystal field transitions in the range of 550–700 nm.[29–31] In contrast, Mn^{4+} species in MnO_2 exhibit a broad peak in the region of 400 nm and shoulder peaks at approximately 575 and 700 nm.[32] The *in-situ* UV–vis spectral changes for the MnO NPs, in which a continuous peak between 350–500 nm and a broad shoulder between 500–700 nm were observed, are nearly identical to those previously reported for Mn^{4+} species in MnO_2 nanocrystals.[33,34] Although no distinct peak was observed for Mn^{5+}, the possibility for the formation of Mn^{5+} species during catalysis could not be excluded. However, most Mn^{5+} species described in the literature exhibit two distinct peaks in the range of 350 and 520 nm.[35] Therefore, ΔAbs_{400} and ΔAbs_{600} likely correspond to Mn^{4+} species, rather than Mn^{3+} or Mn^{5+} species.

The formation of Mn^{4+} species was also further supported by the results of XANES, EPR and Raman spectral analyses, as described above. Taken together, the findings from the present analyses by the measurement of CV, EPR, XANES and Raman (Figure 3.9a and 3.10) and previous studies examining Mn oxide compounds indicate that ΔAbs_{400} corresponds to the ligand-to-metal charge transfer band of Mn^{4+} species.[27,36] Furthermore, ΔAbs_{600} can be assigned to the d-d transition band of Mn^{4+}. Because d-d transition of the octahedral system is Laporte forbidden according to the selection rule, the d-d transition band of Mn^{4+}–O species intrinsically exhibits broad peak characteristics with low intensity.[37,38]

ΔAbs_{400}, ΔAbs_{600}, and the current density were plotted against applied potentials to the MnO NPs (Figure 3.9c and d). The intensity of the two absorption peaks was strongly correlated with the onset of the OER. Moreover, the reversibility of the Mn species was also demonstrated. A gradual decline of the peak intensity was detected as the potential was reversed (Figure 3.11). In contrast, no spectral changes at the same potential range were observed for the bulk MnO compounds (Figure 3.9b and 3.12). In addition, no peak changes were detected for the MnO NPs when the *in-situ* experiments were conducted in an organic electrolyte, $(TBA)ClO_4$ in $CHCl_3$ (Figure 3.13), a finding that was consistent with a previous study.[16] Therefore, it is considered that the observed spectral changes resulted from the formation of Mn^{4+}=O species in the presence of water.

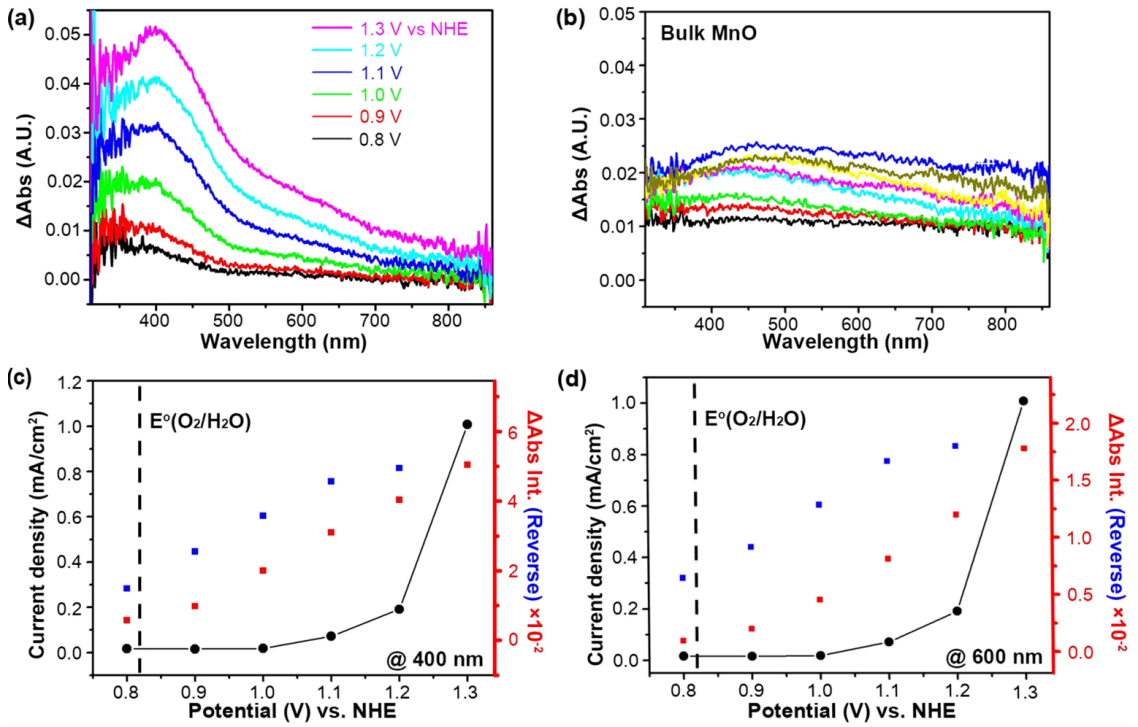

Figure 3.9 | *In-situ* UV–vis spectra of MnO. (a) Difference spectra of the MnO NPs based on the applied potential, (b) Difference spectra of bulk MnO, and (c, d) Potential dependence of the current density (solid line) and the differential absorbance at 400 and 600 nm for the MnO NPs, respectively.

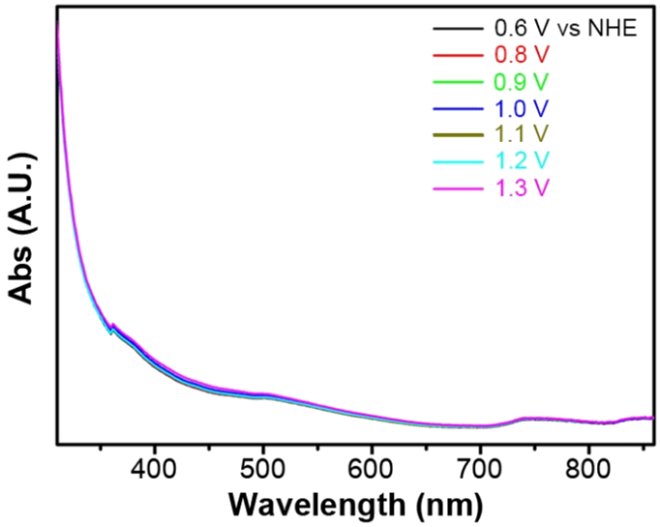

Figure 3.10 | Diffuse transmission UV–vis absorption spectra of the MnO NPs film at increasing potentials. The spectrum measured at 0.6 V vs SHE was used as a reference spectrum to display changes in the UV–vis spectrum (Figure 3.9a).

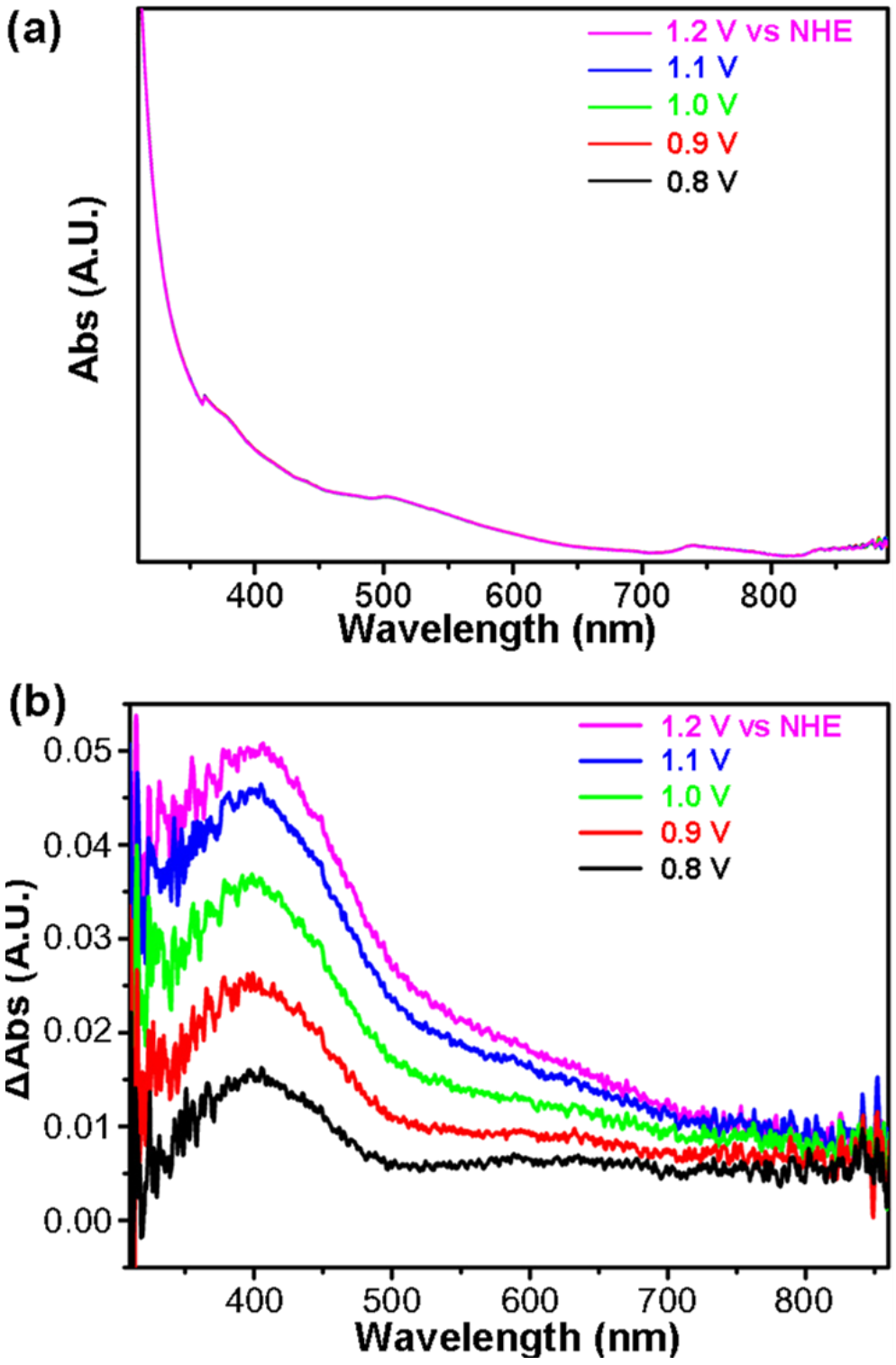

Figure 3.11 | (a) *In-situ* diffuse transmission UV–vis absorption spectra of the MnO NP film. (b) Changes in the UV–vis spectrum of the MnO NPs at decreasing potentials from 1.2 to 0.8 V vs. SHE. The spectra indicate that ΔAbs_{400} and ΔAbs_{600} bands assigned to Mn^{4+}=O species exhibit reversibility.

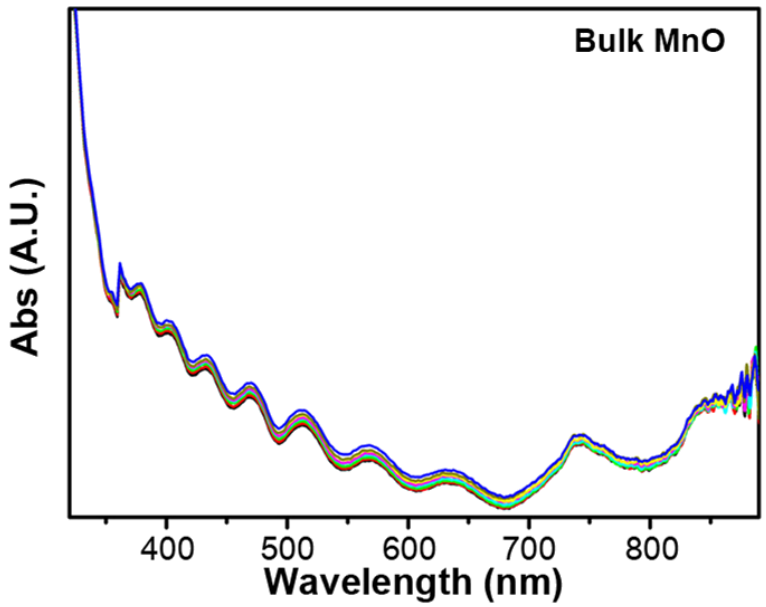

Figure 3.12 | Diffuse transmission UV–vis absorption spectra of bulk MnO at increasing potentials (0.6, 0.8, 0.9, 1.0, 1.1, 1.2, 1.3, and 1.4 V vs SHE) at pH 7. The spectrum measured at 0.6 V vs SHE was used as the reference spectrum to display changes in the UV–vis spectra (Figure 3.9b).

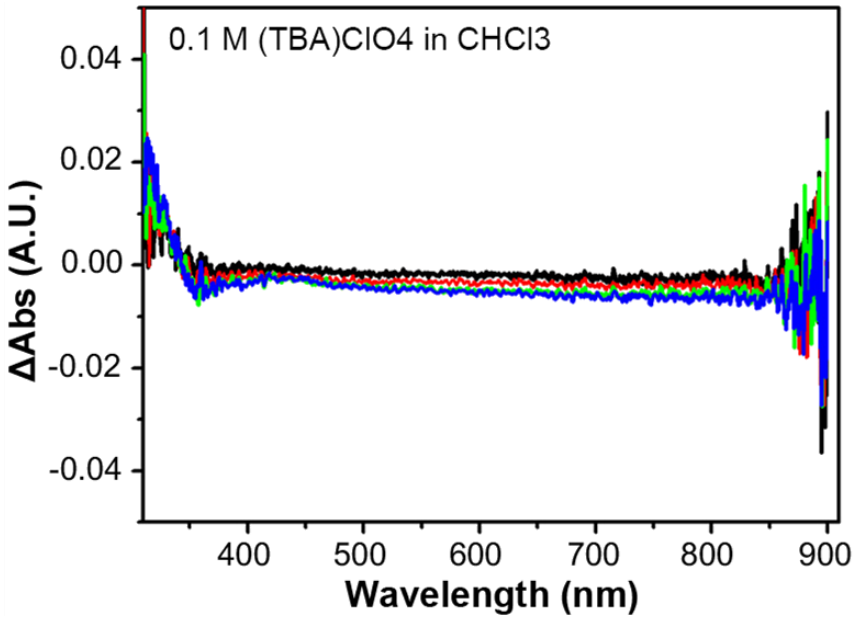

Figure 3.13 | Changes in the i*n-situ* UV–vis spectrum of the MnO NPs film electrode at increasing potentials (1.2, 1.1, 1.0 0.9 and 0.8 V vs. SHE) in a 0.1 M (TBA)ClO_4 in $CHCl_3$ solution. No peak was observed. The *in-situ* UV–vis spectra indicate that ΔAbs_{400} and ΔAbs_{600} in Figure 3.9a are related to the presence of water molecules.

Formation of Mn^{4+}=O can be observed in pre-edge XANES spectra at high anodic potential as shown in Figure 3.6. As the potential increased up to 1.4 V vs. SHE, a new park around 6543 eV (marked as A3) distinctly emerged. According to previous studies,[39,40] this abnormal feature can be attributed to the formation of Mn^{4+}=O. Additionally, potential-dependent EXAFS data also provided the evidence of Mn^{4+}=O formation. The bond length of octahedral Mn–O was 1.79 Å at the initial state and low potential (Figure 3.14). At 1.4 V vs. SHE, the Mn–O bond became shortened to 1.70 Å, which accorded with the characteristic bonding lengths of Mn=O in previous reports.[39,41,42] Taken together, evidence for the generation of the Mn^{4+}=O species has been observed.

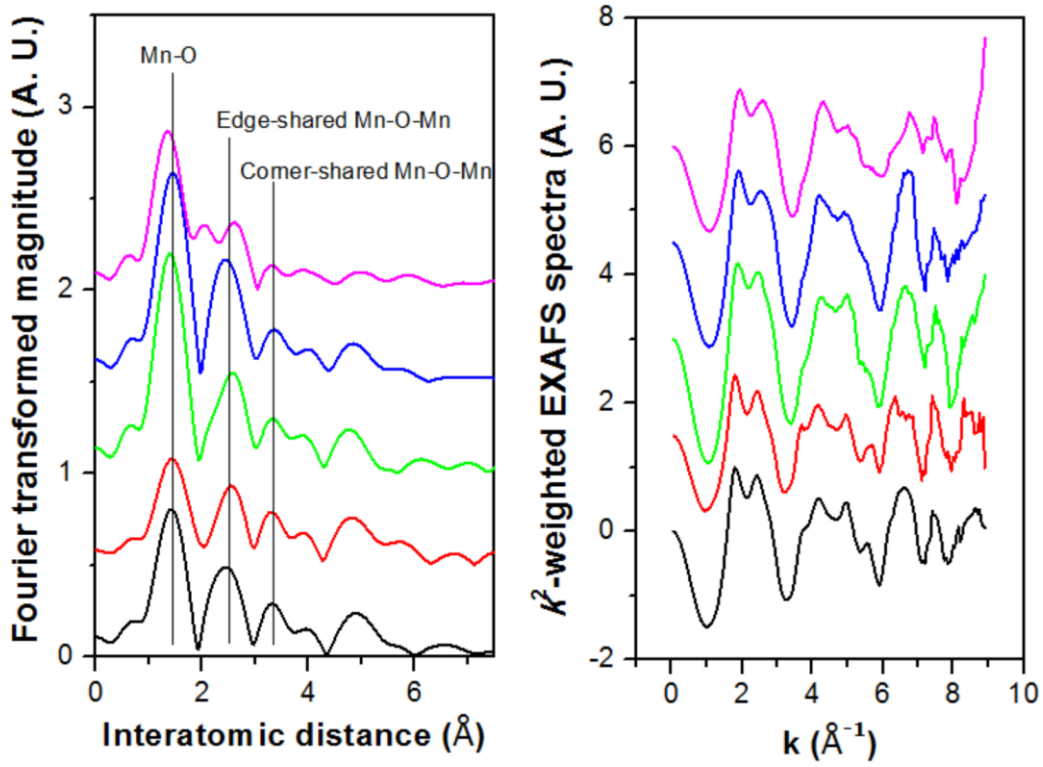

Figure 3.14 | Potential dependence of (a) Fourier-transformed and (b) K2-weighted EXAFS spectra of the MnO NPs. Initial state (red), 0.4 V (green), 1.1 V (blue), 1.3 V (cyan), and 1.4 V (purple) vs. SHE.

The present electrokinetic and spectroscopic analyses led to a proposal of the scheme of the overall redox process for the Mn species on the MnO NPs during the OER (Scheme 3.1). The observed redox behavior and the pH-dependent shifts in the CV curves (Figure 3.4a), combined with the results of the EPR measurement (Figure 3.5), suggest that Mn^{2+}–OH_2 surface species are oxidized to Mn^{3+}–OH during the first redox wave. Furthermore, the analysis of electrokinetics (Figure 3.2, Table 3.1) and *in-situ* UV–vis spectra (Figure 3.9–3.11) revealed that a concerted one-proton and one-electron oxidation reaction, Mn^{3+}–OH → Mn^{4+}=O, occurred as a quasi-equilibrium step before the RDS. The results of *in-situ* Raman spectroscopy (Figure 3.7 and 3.8) further confirmed the stepwise oxidation of Mn^{2+} to Mn^{4+} *via* the formation of Mn^{3+}.

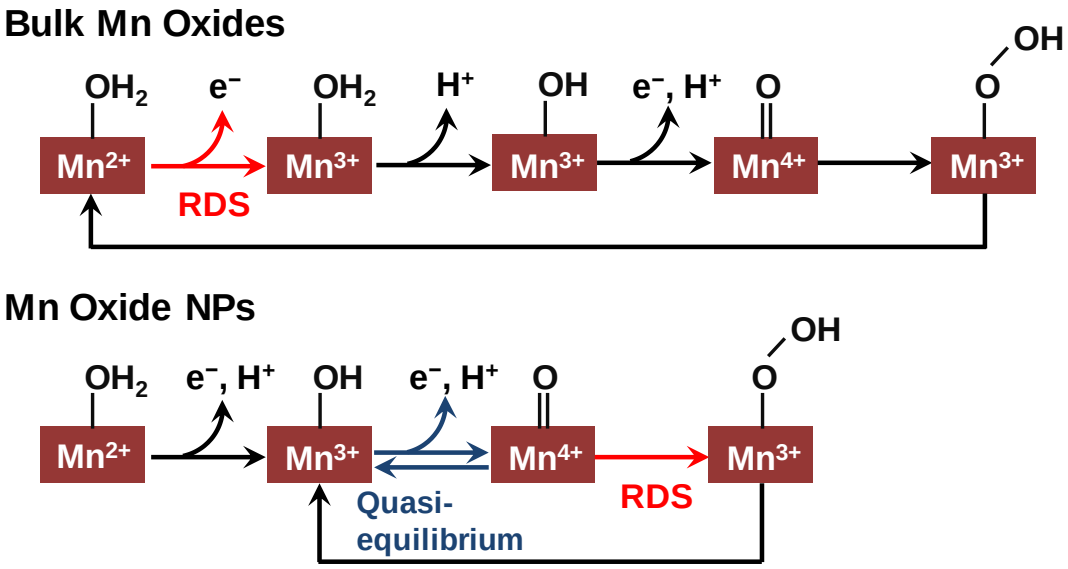

Scheme 3.1 | Proposed water oxidation mechanisms of conventional Mn catalysts (top) and the monodisperse 10 nm-sized MnO NPs (bottom). Each model represents the terminated surface active species including Mn atoms and bound reaction species.

Finally, the proposed mechanistic schemes of the MnO NPs and conventional Mn catalysts were compared (Scheme 3.1). As stated above, the RDS for conventional Mn catalysts is a one-electron oxidation reaction, Mn^{2+}–OH_2 $\rightarrow$ Mn^{3+}–OH_2, which proceeds without a quasi-equilibrium step. Experimental data for the zeroth reaction order of proton and the transfer coefficient value of 1/2 also support this claim. After formation of Mn^{3+}–OH_2, sequential deprotonation processes are expected to occur, based on the pK_a value of Mn^{3+} species.[20] In contrast, for the 10-nm-sized MnO NPs, the formation of Mn^{3+} species is no longer the RDS. Rather, CPET proceeds as a quasi-equilibrium step to produce Mn^{4+}=O intermediates. The reaction mechanism proposed here is displayed based on the spectroscopic and electrokinetic evidence of Mn^{4+}=O assuming the acid–base mechanism (Scheme 3.1). However, it is noted that O–O bond formation after the step of the generation of Mn^{4+}=O can be modified or further interpreted based on direct-coupling mechanisms,[43–45] radical-involved acid–base mechanisms,[46] or mechanisms involving lattice oxygen.[47]

From this comparative study, it was demonstrated that the improved catalytic property of the MnO NPs can be explained by the unique reaction mechanism. Stabilization of Mn^{3+} intermediates in the MnO NPs appears to alter the RDS.

Based on the results of *in-situ* electrochemical Raman spectroscopy (Figure 3.7 and 3.8) and the comparison to the previous reports, the vibration modes of Mn^{2+}, Mn^{3+}, and Mn^{4+} detected this time are similar to those of Mn–O bonds in MnO,[25] α-Mn_2O_3,[48] and λ-MnO_2,[25] respectively (Scheme 3.2). The dynamic changes in the bond structures and resulting asymmetry in the ligand field which can get rid of the degeneracy of e_g orbitals may be the reason for the stabilization of Mn^{3+}. The present results demonstrated that it is possible for the OER activity of Mn oxides to be substantially improved by the stabilization of Mn^{3+} in the case of oxide crystals whose structure can dynamically change and accommodate distortion.

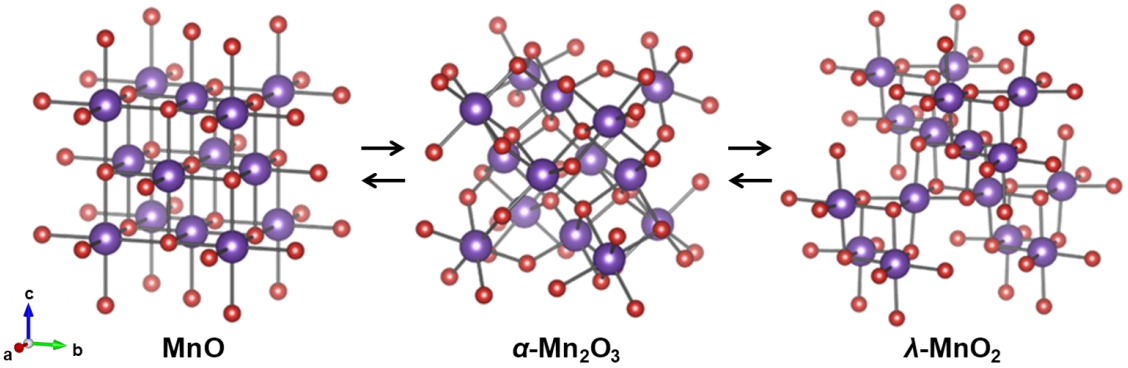

Scheme 3.2 | Schematic image of surface bonding structure changes of the MnO NPs based on the results of *in-situ* electrochemical Raman spectroscopy (Figure 3.7 and 3.8).

3.4 Conclusions

In conclusion, the electrochemical OER mechanism catalyzed by the MnO NPs was investigated and it was revealed that this material exhibits exceptionally high OER activity in neutral conditions. Comprehensive electrochemical and *in-situ* spectroscopic analyses demonstrated that the nanosized Mn oxide electrocatalyst was mechanistically distinct from conventional Mn oxide catalysts. Specifically, $1H^+/1e^-$ CPET occurs as a quasi-equilibrium step, followed by a chemical RDS. The sequential oxidation of Mn and the generation of Mn^{4+}=O species were directly monitored by various spectroscopic analyses, including EPR, *in-situ* XANES, UV–vis, and Raman spectroscopy, by virtue of the high surface-area-to-volume ratio of the MnO NPs. The unique OER mechanism of the MnO NPs is expected to attribute to the high OER activity of this material at neutral pH, and to be because of the ability of the NPs to accommodate distortion in the crystal structure.

References of Chapter 3

1. D. M. Robinson, Y. B. Go, M. Mui, G. Gardner, Z. Zhang, D. Mastrogiovanni, E. Garfunkel, J. Li, M. Greenblatt and G. C. Dismukes, Photochemical water oxidation by crystalline polymorphs of manganese oxides: Structural requirements for catalysis. *J. Am. Chem. Soc.* **2013**, *135*, 3494–3501.
2. R. Pokhrel, M. K. Goetz, S. E. Shaner, X. Wu and S. S. Stahl, The "best catalyst" for water oxidation depends on the oxidation method employed: A case study of manganese oxides. *J. Am. Chem. Soc.* **2015**, *137*, 8384–8387.
3. P. F. Smith, B. J. Deibert, S. Kaushik, G. Gardner, S. Hwang, H. Wang, J. F. Al-Sharab, E. Garfunkel, L. Fabris, J. Li and G. C. Dismukes, Coordination geometry and oxidation state requirements of corner-sharing MnO_6 octahedra for water oxidation catalysis: An investigation of manganite (γ-MnOOH). *ACS Catal.* **2016**, *6*, 2089–2099.
4. A. Iyer, J. Del-Pilar, C. K. King'ondu, E. Kissel, H. F. Garces, H. Huang, A. M. El-Sawy, P. K. Dutta and S. L. Suib, Water oxidation catalysis using amorphous manganese oxides, octahedral molecular sieves (OMS-2), and octahedral layered (OL-1) manganese oxide structures. *J. Phys. Chem. C* **2012**, *116*, 6474–6483.
5. I. Zaharieva, P. Chernev, M. Risch, K. Klingan, M. Kohlhoff, A. Fischer and H. Dau, Electrosynthesis, functional, and structural characterization of a water-oxidizing manganese oxide. *Energy Environ. Sci.* **2012**, *5*, 7081–7089.
6. K. Jin, J. Park, J. Lee, K. D. Yang, G. K. Pradhan, U. Sim, D. Jeong, H. L. Jang, S. Park, D. Kim, N.-E. Sung, S. H. Kim, S. Han and K. T. Nam, Hydrated manganese(II) phosphate ($Mn_3(PO_4)_2 \cdot 3H_2O$) as a water oxidation catalyst. *J. Am. Chem. Soc.* **2014**, *136*, 7435–7443.
7. K. Jin, A. Chu, J. Park, D. Jeong, S. E. Jerng, U. Sim, H.-Y. Jeong, C. W. Lee, Y-S. Park, K. D. Yang, G. K. Pradhan, D. Kim, N.-E. Sung, S. H. Kim and K. T. Nam, Partially oxidized

sub-10 nm MnO nanocrystals with high activity for water oxidation catalysis. *Sci. Rep.* **2015**, *5*, 10279.

8. D. Jeong, K. Jin, S. E. Jerng, H. Seo, D. Kim, S. H. Nahm, S. H. Kim and K. T. Nam, Mn_5O_8 nanoparticles as efficient water oxidation catalysts at neutral pH. *ACS Catal.* **2015**, *5*, 4624–4628.
9. S. W. Lee, C. Carlton, M. Risch, Y. Surendranath, S. Chen, S. Furutsuki, A. Yamada, D. G. Nocera and Y. Shao-Horn, The nature of lithium battery materials under oxygen evolution reaction conditions. *J. Am. Chem. Soc.* **2012**, *134*, 16959–16962.
10. A. J. Bard and L. Faulkner, *Electrochemical techniques: Fundamentals and applications*. Wiley and Sons, New York, U. S. A., **1980**.
11. R. L. Doyle, I. J. Godwin, M. P. Brandon and M. E. G. Lyons, Redox and electrochemical water splitting catalytic properties of hydrated metal oxide modified electrodes. *Phys. Chem. Chem. Phys.* **2013**, *15*, 13737–13783.
12. Y. Surendranath, M. W. Kanan and D. G. Nocera, Mechanistic studies of the oxygen evolution reaction by a cobalt-phosphate catalyst at neutral pH. *J. Am. Chem. Soc.* **2010**, *132*, 16501–16509.
13. T. Shinagawa, A. T. Garcia-Esparza and K. Takanabe, Insight on Tafel slopes from a microkinetic analysis of aqueous electrocatalysis for energy conversion. *Sci. Rep.* **2015**, *5*, 13801.
14. J. Park, H. Kim, K. Jin, B. J. Lee, Y.-S. Park, H. Kim, I. Park, K. D. Yang, H.-Y. Jeong, J. Kim, K. T. Hong, H. W. Jang, K. Kang and K. T. Nam, A new water oxidation catalyst: Lithium manganese pyrophosphate with tunable Mn valency. *J. Am. Chem. Soc.* **2014**, *136*, 4201–4211.
15. M. Huynh, C. Shi, S. J. Billinge and D. G. Nocera, Nature of activated manganese oxide for

oxygen evolution. *J. Am. Chem. Soc*. **2015**, *137*, 14887–14904.

16. T. Takashima, K. Hashimoto and R. Nakamura, Inhibition of charge disproportionation of MnO_2 electrocatalysts for efficient water oxidation under neutral conditions. *J. Am. Chem. Soc.* **2012**, *134*, 18153–18156.
17. T. Takashima, A. Yamaguchi, K. Hashimoto, H. Irie and R. Nakamura, In situ UV-vis absorption spectra of intermediate species for oxygen-evolution reaction on the surface of MnO_2 in neutral and alkaline media. *Electrochemistry* **2014**, *82*, 325–327.
18. D. K. Bediako, C. Costentin, E. C. Jones, D. G. Nocera and J.-M. Savéant, Proton-electron transport and transfer in electrocatalytic films. Application to a cobalt-based O_2-evolution catalyst. *J. Am. Chem. Soc.* **2013**, *135*, 10492–10502.
19. C. Costentin, T. R. Porter and J.-M. Savéant, Conduction and reactivity in heterogeneous-molecular catalysis: New insights in water oxidation catalysis by phosphate cobalt oxide films. *J. Am. Chem. Soc.* **2016**, *138*, 5615–2622.
20. A. Yamaguchi, R. Inuzuka, T. Takashima, T. Hayashi, K. Hashimoto and R. Nakamura, Regulating proton-coupled electron transfer for efficient water splitting by manganese oxides at neutral pH. *Nat. Commun.* **2014**, *5*, 4256.
21. S. J. Hawkes, All positive ions give acid solutions in water. *J. Chem. Educ.* **1996**, *73*, 516.
22. R. Gupta, T. Taguchi, B. Lassalle-Kaiser, E. L. Bominaar, J. Yano, M. P. Hendrich and A. S. Borovik, High-spin Mn-oxo complexes and their relevance to the oxygen-evolving complex within photosystem II. *Proc. Natl. Acad. Sci. U. S. A.* **2015**, *112*, 5319–5324.
23. M. Zlatar, M. Gruden, O. Y. Vassilyeva, E. A. Buvaylo, A. Ponomarev, S. Zvyagin, J. Wosnitza, J. Krzystek, P. Garcia-Fernandez and C. Duboc, Origin of the zero-field splitting in mononuclear octahedral Mn^{IV} complexes: A combined experimental and theoretical investigation. *Inorg. Chem*. **2016**, *55*, 1192–1201.

24. S. H. Kim, H. Park, M. S. Seo, M. Kubo, T. Ogura, J. Klajn, D. T. Gryko, J. S. Valentine and W. Nam, Reversible O–O bond cleavage and formation between Mn(IV)-peroxo and Mn(V)-oxo corroles. *J. Am. Chem. Soc.* **2010**, *132*, 14030–14032.

25. C. Julien, M. Massot, R. Baddour-Hadjean, S. Franger, S. Bach and J. P. Pereira-Ramos, Raman spectra of birnessite manganese dioxides. *Solid State Ionics* **2003**, *159*, 345–356.

26. D. P. Dubal, D. S. Dhawale, R. R. Salunkhe, S. M. Pawar and C. D. Lokhande, A novel chemical synthesis and characterization of Mn_3O_4 thin films for supercapacitor application. *Appl. Surf. Sci*. **2010**, *256*, 4411–4416.

27. X. Hao, J. Zhao, Y. Li, Y. Zhao, D. Ma and L. Li, Mild aqueous synthesis of octahedral Mn_3O_4 nanocrystals with varied oxidation states. *Colloids Surf., A* **2011**, *374*, 42–47.

28. C. F. Wells and G. Davies, A spectrophotometric investigation of the aquomanganese(III) ion in perchlorate media. *J. Chem. Soc. A*, **1967**, *0*, 1858–1861.

29. W. Yu, C. Zhou, D. Tong and T. Xu, Aerobic oxidation of 4-*tert*-butyltoluene over cobalt and manganese supported hexagonal mesoporous silicas as heterogeneous catalysts. *J. Mol. Catal. A: Chem.* **2012**, *365*, 194–202.

30. S. Chen, J. Zhu, X. Wu, Q. Han and X. Wang, Graphene oxide−MnO_2 nanocomposites for supercapacitors. *ACS Nano* **2010**, *4*, 2822–2830.

31. R. Al-Oweini, A. Sartorel, B. S. Bassil, M. Natali, S. Berardi, F. Scandola, U. Kortz and M. Bonchio, Photocatalytic water oxidation by a mixed-valent $Mn^{III}_3Mn^{IV}O_3$ manganese oxo core that mimics the natural oxygen-evolving center. *Angew. Chem., Int. Ed.* **2014**, *53*, 11182–11185.

32. N. Sakai, Y. Ebina, K. Takada and T. Sasaki, Photocurrent generation from semiconducting manganese oxide nanosheets in response to visible light. *J. Phys. Chem. B.* **2005**, *109*, 9651–9655.

33. Y. Omomo, T. Sasaki, L. Wang and M. Watanabe, Redoxable nanosheet crystallites of MnO_2 derived via delamination of a layered manganese oxide. *J. Am. Chem. Soc.* **2003**, *125*, 3568–3575.

34. C. N. Butterfield, A. V. Soldatova, S.-W. Lee, T. G. Spiro and B. M. Tebo, Mn(II,III) oxidation and MnO_2 mineralization by an expressed bacterial multicopper oxidase. *Proc. Natl. Acad. Sci. U. S. A.* **2013**, *110*, 11731–11735.

35. S. Hong, Y.-M. Lee, M. Sankaralingam, A. K. Vardhaman, Y. J. Park, K.-B. Cho, T. Ogura, R. Sarangi, S. Fukuzumi and W. Nam, A manganese(V)-oxo complex: Synthesis by dioxygen activation and enhancement of its oxidizing power by binding scandium ion. *J. Am. Chem. Soc.* **2016**, *138*, 8523–8532.

36. M. Siebecker, A. S. Madison and G. W. Luther, Reduction kinetics of polymeric (soluble) manganese (IV) oxide (MnO_2) by ferrous iron (Fe^{2+}). *Aquat. Geochem.* **2015**, *21*, 143–158.

37. A. B. P. Lever, *Inorganic electronic spectroscopy*. Elsevier, Amsterdam, The Netherlands, **1984**.

38. J. E. Huheey, E. A. Keiter, R. L. Keiter and O. K. Medhi, *Inorganic chemistry: Principles of structure and reactivity*. Pearson Education, London, U. K., **2006**.

39. D. F. Leto and T. A. Jackson, Mn K-Edge X-ray absorption studies of oxo- and hydroxo-manganese(IV) complexes: experimental and theoretical insights into pre-edge properties. *Inorg. Chem.* **2014**, *53*, 6179–6194.

40. T.-C. Weng, W.-Y. Hsieh, E. S. Uffelman, S. W. Gordon-Wylie, T. J. Collins, V. L. Pecoraro and J. E. Penner-Hahn, XANES evidence against a manganyl species in the S_3 state of the oxygen-evolving complex. *J. Am. Chem. Soc.* **2004**, *126*, 8070–8071.

41. T. Kurahashi, A. Kikuchi, T. Tosha, Y. Shiro, T. Kitagawa and H. Fujii, Transient intermediates from Mn(salen) with sterically hindered mesityl groups: Interconversion

between Mn^{IV}-phenolate and Mn^{III}-phenoxyl radicals as an origin for unique reactivity. *Inorg. Chem.* **2008**, *47*, 1674–1686.

42. X. Wu, M. S. Seo, K. M. Davis, Y.-M. Lee, J. Chen, K.-B. Cho, Y. N. Pushkar, and W. Nam, A highly reactive mononuclear non-heme manganese(IV)-oxo complex that can activate the strong C-H bonds of alkanes. *J. Am. Chem. Soc.* **2011**, *133*, 20088–20091.
43. L. Duan, F. Bozoglian, S. Mandal, B. Stewart, T. Privalov, A. Llobet and L. Sun, A molecular ruthenium catalyst with water-oxidation activity comparable to that of photosystem II. *Nat. Chem.* **2012**, *4*, 418–423.
44. K. Ray, F. Heims, M. Schwalbe and W. Nam, High-valent metal-oxo intermediates in energy demanding processes: from dioxygen reduction to water splitting. *Curr. Opin. Chem. Biol.* **2015**, *25*, 159–171.
45. C. Casadevall, Z. Codolà, M. Costas and J. Lloret-Fillol, Spectroscopic, electrochemical and computational characterisation of Ru species involved in catalytic water oxidation: Evidence for a [Ru^{V}(O)(Py_2^{Me}tacn)] intermediate. *Chem. - Eur. J.* **2016**, *22*, 10111–10126.
46. M. Huynh, D. K. Bediako and D. G. Nocera, A functionally stable manganese oxide oxygen evolution catalyst in acid. *J. Am. Chem. Soc.* **2014**, *136*, 6002–6010.
47. J. T. Mefford, X. Rong, A. M. Abakumov, W. G. Hardin, S. Dai, A. M. Kolpak, K. P. Johnston and K. J. Stevenson, Water electrolysis on $La_{1-x}Sr_xCoO_{3-\delta}$ perovskite electrocatalysts. *Nat. Commun.* **2016**, *7*, 11053.
48. M-C. Bernard, A. H.-L. Goff, B. V. Thi and S. C. de Torresi, Electrochromic reactions in manganese oxides I. Raman analysis. *J. Electrochem. Soc.* **1993**, *140*, 3065–3070.

Chapter 4.

Application of Manganese Oxide Water Oxidation Catalysts to Polymer Exchange Membrane (PEM) Electrolyzers

4.1 Introduction

In Chapter 2 and 3, it was revealed that the multi-electron-transfer ability of Mn oxide OER catalysts can be enhanced by the design of ligands or particle diameters. For the industrial application of the enhanced OER activity, however, it is required to consider the requirement for or the environment around the OER catalysts in industry. The importance of the evaluation of Mn oxide OER catalysts in specific target conditions was also proposed by Stahl *et al.*[1]

So far, three types of electrolyzers have been mainly developed: alkaline electrolyzers,[2] PEM electrolyzers,[3] and solid oxide electrolyzers.[4,5] Among them, PEM electrolyzers possess advantages as the energy conversion systems from renewable to chemical energy including high voltage efficiency, rapid response to input changes, high current density, usage of non-corrosive liquid, and relatively low working temperature (< 100 ℃).[3] These advantages are directly or indirectly related to currently standard PEMs with low gas permeation rate and high proton conductivity, typically composed of perfluorinated sulfonic acid polymers.[3,6] However, because of the corrosive acidic environment for catalysts provided by PEMs, noble metal OER catalysts have been used for PEM electrolyzers.

One strategy to address this problem of the acidic environment is to use alkaline exchange membranes (AEMs).[7–9] However, although there has recently been significant progress in the development of AEMs,[7] the ionic conductivity and stability of AEMs still need to be largely improved to rival those of PEMs such as Nafion. It is also to be noted that the lower mobility of

OH^- than that of H^+ is an intrinsic problem for AEMs.[6,10] If low-cost OER catalysts which can function in acidic environment can be developed, the above-mentioned advantages of PEM electrolyzers can be utilized to develop low-cost and efficient systems for the production of chemical fuels by renewable energy.

Therefore, low-cost OER catalysts applicable in acidic environment have been desired and investigated. Because surface pH on the anode easily turns acidic during the OER even in the presence of buffer species,[11,12] OER catalysts functional in acidic conditions are also relevant and beneficial to normal liquid-electrolyte-based electrolyzers at neutral pH utilizing abundant and safe water sources. However, most of the studies for the development of the catalysts for the OER in acidic conditions have been focused on materials containing Ir or Ru[13–17] and how to decrease their noble metal content.[14,16,18–24] The increase of activity per amount of noble metal has already been achieved, for example, by using mixed oxides with less expensive metals such as Ni,[18,19] W,[20] or tin (Sn),[21] or nanostructuring.[14,22–24] Only very recently, several examples of earth-abundant OER catalysts which can operate at acidic pH have been reported. Especially, Mn-based materials are considered as interesting substitutes to Ir-based or Ru-based catalysts since, even in acidic conditions, there is a possibility for Mn oxide phases to be preserved without dissolution to Mn^{2+} at anodic potential while keeping their function as OER catalysts.[25] Nocera *et al.* reported that, in acidic conditions (pH = 0.1), an electrodeposited Mn oxide can functionally stably catalyze the OER by virtue of the oxidative electrodeposition of the dissolved Mn ions.[25] Stephens *et al.* reported that Ti atoms on a Mn oxide can mitigate the dissolution in acidic conditions (pH 1) without large decrease of the OER activity.[26] Fluorine-doped copper Mn oxide was developed by Patel *et al.* which showed excellent activity and stability for the OER in 0.5 M H_2SO_4 aqueous solution.[27] In addition to these Mn-oxide-based catalysts, Co–Fe cyanide,[28] Janus Co/CoP nanoparticles,[29] MoS_2, TaS_2,[30] Co_3O_4,[31] and barium salt of a Co-phosphotungstate polyanion[32]

were very recently introduced as catalysts for the OER in acidic conditions. They maintained their activity for hours in acid. Nocera *et al.* also reported that electrodeposition of Co oxide (CoO_x) OER catalysts in the presence of Mn or Fe and lead (Pb) ions to obtain $CoMnO_x$ or $CoFePbO_x$ can enhance the stability of CoO_x in acid while maintaining the activity.[33] Lewis *et al.* reported Ni–Mn antimonate as a stable OER catalyst in aqueous 1.0 M H_2SO_4.[34] Although the works represent significant progress in the development of acid-stable earth-abundant OER catalysts, further study will be required to develop the PEM electrolyzers with non-noble-metal-based OER catalysts which are economically suitable for the large-scale conversion of renewable energy. Importantly, the evaluation of the OER catalysts in PEM electrolyzers has not been conducted so far in the case of earth-abundant OER catalysts.

Also, it is noted that the sulfonic acid groups typically exist around the catalysts in PEM electrolyzers. The sulfonic acid groups may also be able to contribute to the enhancement of the OER activity of Mn oxides by coordination or the management of proton transfer.

Herein, Mn oxide samples have been evaluated as OER catalysts in an acidic aqueous solution and, for the first time, in PEM electrolyzers. Through the evaluation of six samples synthesized by industrial methods, it was demonstrated that, although the OER activity of the samples was different in an acidic aqueous solution, they can readily show a comparable OER activity to Pt/C in PEM electrolyzers. Pt/C is used in relatively cheap PEM electrolyzers, although the OER activity is lower than Ir-based or Ru-based OER catalysts. Impressively, even when PEM electrolyzers with Pt/C OER catalysts are used, by connecting them to solar cells, Sugiyama and Fujii *et al.* demonstrated an STH energy conversion efficiency of as high as 24.4%.[35]

4.2 Experimental Methods

4.2.1 Synthesis of Manganese Oxides

#1, α-MnO_2: Electrodeposition of the Mn oxide was conducted with the aqueous solution containing 0.502 M of $MnSO_4$ and 3.0 M of $(NH_4)_2SO_4$ as the electrolyte at 8 mA cm^{-2}, 96 °C, for 25 hours, while maintaining the concentration of NH_4^+ and SO_4^{2-} to be 3.0 M and 0.31 M, respectively, by continuous supply of the solution of $MnSO_4$ and $(NH_4)_2SO_4$. The deposit was ground, washed with water, and dried to obtain the final sample.

#2, β-MnO_2: Electrodeposition of the Mn oxide on a Ti anode was conducted in a bath with a H_2SO_4–$MnSO_4$ mixture at 7 mA cm^{-2}, 96 °C, for 10 days, while maintaining the concentration of SO_4^{2-} to be 0.33 M by continuous addition of 0.85 M $MnSO_4$ aqueous solution. The resultant deposit was ground until the average diameter of secondary particles became 40 μm, washed by water, neutralized, and dried by flash drying. The sample was obtained by calcination of the dried sample at 420 °C for 36 hours.

#3, δ-MnO_2: 2.5 L of 0.100 M $KMnO_4$, 2.50 M of H_2SO_4 aqueous solution was added to 1 L of the solution containing 0.552 M of Mn ion and 2.55 M of SO_4^{2-} (an acidic $MnSO_4$ solution), followed by stirring at 30 °C for 24 hours. After separated by filtration, the black deposit was washed by dispersing it in 500 mL of pure water for one hour for two times. The washed deposit was dispersed again in 500 mL of pure water and neutralized by addition of 1 M NaOH until the pH of the slurry became 5.6. The final sample was obtained after the filtration and drying.

#4, Mn_3O_4: 1.05 M NaOH aqueous solution was added to aqueous 0.63 M $MnSO_4$ while providing aeration. The resultant precipitate was used as the sample.

#5, γ-MnO_2, electrolytic Mn dioxide (EMD): During the flash drying in the synthesis of sample #2, fine powders generated by overgrinding was collected by a bag filter of a dust collector and used as the sample.

#6, γ-MnO_2, chemical Mn dioxide (CMD): 1.05 M NaOH aqueous solution was added to aqueous 0.63 M $MnSO_4$ while providing aeration. 45 g of the resultant precipitate was immersed in 240 g of 3 M H_2SO_4, followed by stirring at 60 °C for 24 hours. After the black deposit was separated by filtration, it was washed by dispersion in 500 mL of pure water for one hour for two times. The washed deposit was dispersed again in 500 mL of pure water and neutralized by addition of 1 M NaOH until the pH of the slurry became 5.9. The final sample was obtained after filtration and drying.

4.2.2 Characterization of Physical Properties of Samples

Crystal structures were identified by XRD.

The average valency of Mn was measured by titration and the evaluation of purity. First, 0.200 g of a Mn oxide sample was dissolved in the mixture of 10 mL of 0.3 M $(COOH)_2$ and 20 mL of 9 M H_2SO_4 at 70 °C. The solution was titrated by 0.6328 mM $KMnO_4$. The purity of Mn^{4+} was calculated by the following equation:

$$\text{Purity of } Mn^{4+} (\%) = (B - A) \times 2.1735 \quad (4.1)$$

where A and B are the volume of 0.6328 mM $KMnO_4$ in mL required for blank test and the titration, respectively. The purity of total Mn was measured by inductively coupled plasma atomic

emission spectroscopy (ICP-AES). Finally, average Mn valency was calculated by the following equation:

$$\text{Average valency of Mn} = \text{Purity of } Mn^{4+}\ (\%) \times 63.19 / \text{Purity of total Mn } (\%) \times 2 \qquad (4.2)$$

The diameter of the primary and secondary particles was evaluated by SEM observation (S-4800, Hitachi) and a laser-based particle size analyzer (Microtrac HRA, Honeywell), respectively. For the measurement of the diameter of the secondary particles, 0.5 g of the sample in 50 mL of pure water, sonicated for 10 seconds, was used. 1.33 and 2.20 were used as the refractive index of pure water and Mn oxide, respectively.

Brunauer–Emmett–Teller (BET) surface area was measured by the flowing gas method using an automatic analyzer (FlowSorb III, Shimadzu), using nitrogen gas and the single point method. The sample was heated at 150 ℃ for 40 minutes for degassing before the measurement.

4.2.3 Preparation of Electrodes

The working electrodes with or without Nafion ionomer for the measurement in three-electrode systems were fabricated as follows.

Particulate Mn oxide film electrodes without Nafion were prepared by a spray-coating method onto FTO substrates, as previously described.[36] The amount of deposited Mn oxides was ~0.14 mg cm^{-2}. 75 mg of the sample was ground in an agate mortar for 5 minutes and suspended in 100 mL of highly pure Milli-Q water (18 MΩ cm^{-1}) by a sonicator (Q700, QSonica). The suspension was sprayed by a spray gun (ST-6, Fuso Seiki Co., Ltd.) onto a clean conducting FTO-coated

glass substrate (SPD Laboratory, Inc.) heated at 200 ℃. The electrodes were gently washed with the highly pure Milli-Q water and calcined in air for 4 hours at 500 ℃.

The electrodes for the evaluation of the catalysts in the presence of Nafion ionomer were prepared, referring to a typical method for the evaluation of catalysts for PEM-based devices.[37] γ-MnO_2 (#5, EMD) was first blended with carbon black (Vulcan XC-72) with a weight ratio of one to nine in an agar mortar. The mixture was then transferred in a container with 50 mL of ethanol and zirconia balls (0.3 mm in diameter) and subjected to ball milling for 24 hours at 40 rpm. After that, the zirconia balls were removed using a sieve to obtain a slurry containing the γ-MnO_2 (#5, EMD), carbon black, and ethanol. The weight ratio of the γ-MnO_2 (#5, EMD) and carbon black in the resultant slurry was 9.9 to 90.1. By using the slurry, Ir/C (20 wt% Ir on Vulcan XC-72, Premetek), or Pt/C (20 wt% Pt on Vulcan XC-72, Fuel Cell Earth), 1.5 mL of catalyst inks containing 3 mg of the catalyst (Mn oxide, Ir, or Pt) and 50 μL of 10 wt% Nafion solution (#527106, Sigma-Aldrich) were then prepared. Finally, 7 μL of the ink was dropped on a glassy carbon rotating disk electrode (RDE) (diameter: 5 mm) (HR2-D1-GC5, Hokuto Denko) and dried in air, for the subsequent use as the working electrode.

4.2.4 Electrochemical Measurement

Electrochemical measurement in three-electrode systems was conducted using a potentiostat (HZ-7000, Hokuto Denko). A Pt wire and Ag/AgCl/saturated KCl were used as the counter and reference electrode, respectively. Considering that neutral pure water is usually electrolyzed in PEM electrolyzers, neutral electrolyte, 0.5 M Na_2SO_4 aqueous solution (pH 7.5 adjusted by NaOH and H_2SO_4), was used for the evaluation of Nafion-containing working electrodes. The RDE was rotated at 1600 rpm. Ohmic resistance was corrected based on the resistance before the

measurement. Charging current was subtracted from LSV curves. Tafel plots were made by plotting steady-state current at each potential. The highest potential was kept for 1500 seconds to avoid the effect of pseudo-capacitance. At other potentials, the steady-state current was measured after 240 seconds.

4.2.5 PEM Electrolysis

The anodes for the PEM electrolyzers were prepared as follows. Slurries containing a Mn oxide sample, carbon black, and ethanol were prepared in the same way as described above. The weight ratio of the Mn oxide sample to the total weight of the Mn oxide and the carbon black was 5.9%, 11.2%, 10.3%, 5.8%, 11.6%, and 11.1% for the samples #1 to #6, respectively. By using the slurry, Ir/C (20 wt% Ir on Vulcan XC-72, Premetek), or Pt/C (20 wt% Pt on Vulcan XC-72, Fuel Cell Earth), 1.5 mL of catalyst inks containing 15 mg of the total amount of catalyst (Mn oxide, Ir, or Pt) and carbon black and 50 μL of 10 wt% Nafion solution (#527106, Sigma-Aldrich) were then prepared. Finally, 500 μL of the ink was coated on a carbon paper (TGP-H-060, Toray) and dried in air, for the subsequent use as the anode. The cathode was prepared in the same way with the anode using Pt/C as the catalyst for the HER. The Nafion 117 membrane was washed and protonated by boiling it in 3% H_2O_2 aqueous solution, pure water, 1 M H_2SO_4 aqueous solution, and pure water, for one hour each. The pretreated Nafion 117 membrane was then sandwiched between the catalyst-coated side of the anode and the cathode and connected by a hot press at 135 ℃ and mold clamping force of 600 kg for 10 minutes. The membrane electrode assembly thus obtained was incorporated into the chassis of a PEM electrolyzer (3036, FC-R&D) and used as a two-electrode system for subsequent electrochemical measurement.

4.3 Results and Discussion

By different types of industrial methods through either chemical procedures (to produce CMDs) or electrochemical procedures (to produce EMDs), six types (#1–6) of Mn oxides were synthesized.[38] The physical properties of the Mn oxides were comprehensively analyzed. The crystal structure of samples was analyzed by XRD (Figure 4.1). The samples #1–4 were assigned to α-MnO_2, β-MnO_2, δ-MnO_2, and Mn_3O_4, respectively. Samples #5 and #6 was identified as γ-MnO_2, and, because γ-MnO_2 is a crystal structure with controllable parameters their crystal structure was intensively analyzed. The XRD spectrum showed that the sample #5 is γ-MnO_2 which is extensively twined in the ramsdellite 021/061 planes, the typical structure of the EMD prepared with high current densities.[39] The peaks at 2θ = 22.0°, 37.0°, 42.4°, 56.2°, and 67.2° were assigned to (110) of orthorhombic ramsdellite Pbnm structure and (100), (101), (102), and (110) of the pseudo-hexagonal cell.[39] The structure of γ-MnO_2 is expressed as a random intergrowth of pyrolusite (De Wolff disorder) (with 1x1 tunnels) in the ramsdellite matrix (with 1x2 tunnels). The ratio of pyrolusite domains calculated by Chabre and Pannetier's method was 0.35.[39] The ratio of microtwinning and pyrolusite domains in the sample #6 was calculated by the same method,[39] and the result was 0.44 and 0.33, respectively. Those values are in the typical range for CMD samples.[39]

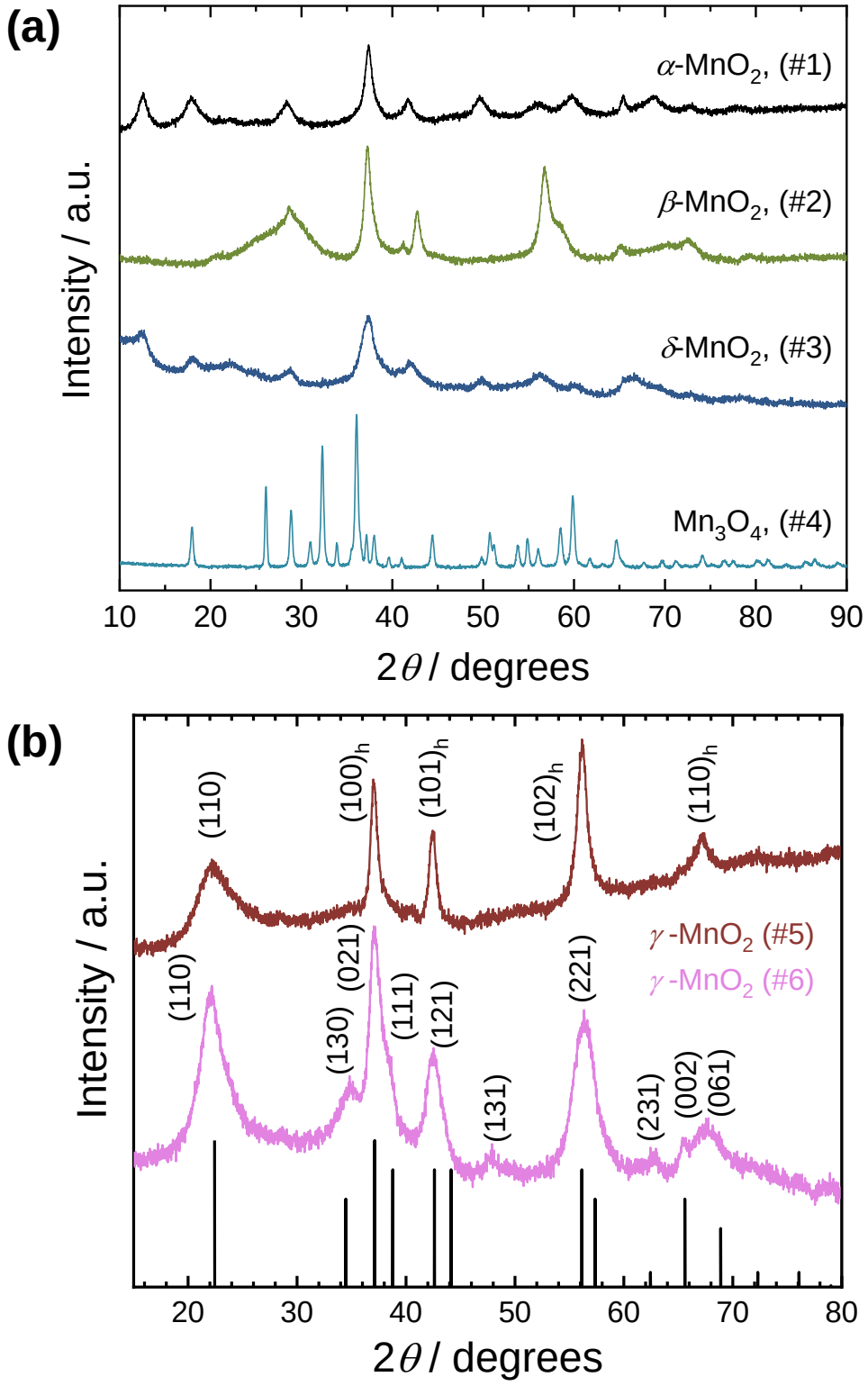

Figure 4.1 | XRD patterns of the six Mn oxides synthesized by industrial methods and evaluated herein: (a) #1 (α-MnO_2), #2 (β-MnO_2), #3 (δ-MnO_2), and #4 (Mn_3O_4); (b) #5 (γ-MnO_2, EMD), and #6 (γ-MnO_2, CMD). A standard XRD pattern of γ-MnO_2 (JCPDS No.14-0644) is also presented as a reference.

SEM images revealed the morphology and distribution of the sample particles, from which the Krumbein diameter was calculated (Figure 4.2). Nanowire morphology of the samples #3 and #6 was evident (Figure 4.2c and f), and the aspect ratio of the samples #1, #2, and #5 was smaller (Figure 4.2a, b, and e). The sample #4 was a mixture of NPs and nanorods (Figure 4.2d). The morphology of the carbon black and its mixture with Mn oxides in the case of γ-MnO_2 (#5, EMD) was also evaluated by SEM measurement. Figure 4.3 shows the SEM image of the carbon black and the mixture of the γ-MnO_2 (#5, EMD) and the carbon black, respectively. The γ-MnO_2 (#5, EMD) was the aggregation of rod-like primary particles with an average diameter of 23 nm (Figure 4.2e and Table 4.1). The average diameter of the secondary particles measured by a laser-based particle size analyzer was 0.6 μm (Table 4.1). On the other hand, the carbon black had a smoother surface than that of the γ-MnO_2 (#5, EMD), and the average diameter of the primary particles was 50 nm (Figure 4.3a and Table 4.1). After the mixture, small γ-MnO_2 (#5, EMD) particles were found among smoother and larger carbon black particles (Figure 4.3b). The change in the diameter of secondary particles also suggested that the smaller γ-MnO_2 (#5, EMD) particles are decorated around the carbon black to form a composite.

Including the result of the measurement of the average diameter of secondary particles, BET surface area, and bulk density, and the result of the analysis of physical properties of the samples are summarized in Table 4.1.

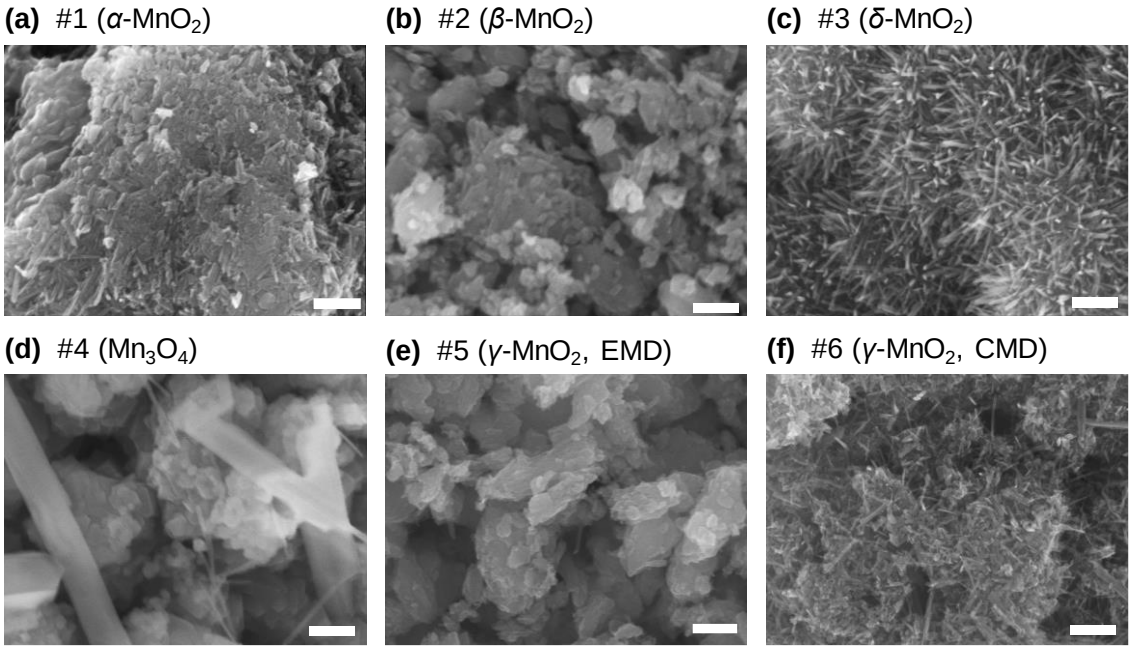

Figure 4.2 | SEM images of the six Mn oxides synthesized by industrial methods and evaluated herein: (a) #1 (α-MnO_2), (b) #2 (β-MnO_2), (c) #3 (δ-MnO_2), (d) #4 (Mn_3O_4), (e) #5 (γ-MnO_2, EMD), (f) #6 (γ-MnO_2, CMD) (scale bar: 200 nm).

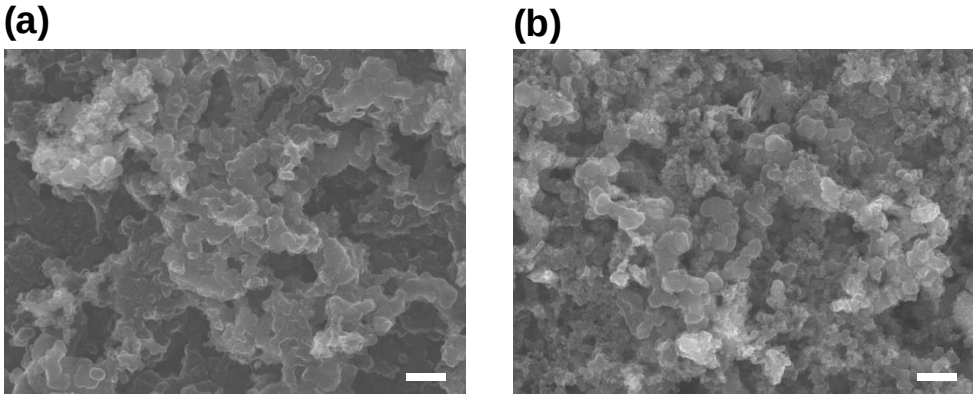

Figure 4.3 | SEM images of (a) the carbon black and (b) the mixture of γ-MnO_2 (#5, EMD) and the carbon black (scale bar: 200 nm)

Table 4.1 | Physical properties and OER activity in acidic aqueous solution of six types of Mn oxides used synthesized by industrial methods and evaluated herein.

		Physical properties								Activity	
	Synthesis method[a]	Avg. Mn Valency	Crys-tal struc-ture	Diameter of primary particles / nm			Avg. diameter of second-ary particles / μm	BET surface area / m^2 g^{-1}	Bulk density / g cm^{-3}	Current density at 1.7 V vs. RHE[b] / mA cm^{-2}	Over-potential at 0.5 mA cm^{-2} / V
				Avg. length of short axes	Avg. length of long axes	Avg.					
#1	Elec.	3.92	α	16	80	48	22	95	1.4	0.764	0.451
#2	Elec.-Cal.	3.99	β	20	60	40	40	13.6	2.2	0.191	0.516
#3	Chem.	3.86	δ	16	150	83	9.7	230	0.5	0.075	0.583
#4	Chem.	2.67	Mn_3O_4	40	50	45	9	5.9	2.0	—	0.7
#5	Elec.	3.94	γ	12	34	23	0.6	40	1.5	0.222	0.520
#6	Chem.	3.94	γ	9	45	27	10	255	0.7	0.937	0.437

[a] Chem.: chemical method (CMD); Elec.: electrochemical method (EMD); Elec.-Cal.: electrochemical method followed by calcination.

[b] RHE: reversible hydrogen electrode.

The samples were evaluated in PEM electrolyzers and compared with standard Ir/C or Pt/C (20 wt% metal on carbon black Vulcan XC-72) catalysts. As shown in Figure 4.4, surprisingly, all the Mn oxide samples showed comparable activity to that of Pt/C, which is used as the catalyst for the OER in relatively cheap PEM electrolyzers.[35,40] Although the voltage at 2 mA cm^{-2} is 190 mV larger than that with Ir, the γ-MnO_2 synthesized by an electrochemical method (#5, EMD) showed highest current density among the Mn oxide samples in the conditions evaluated herein.

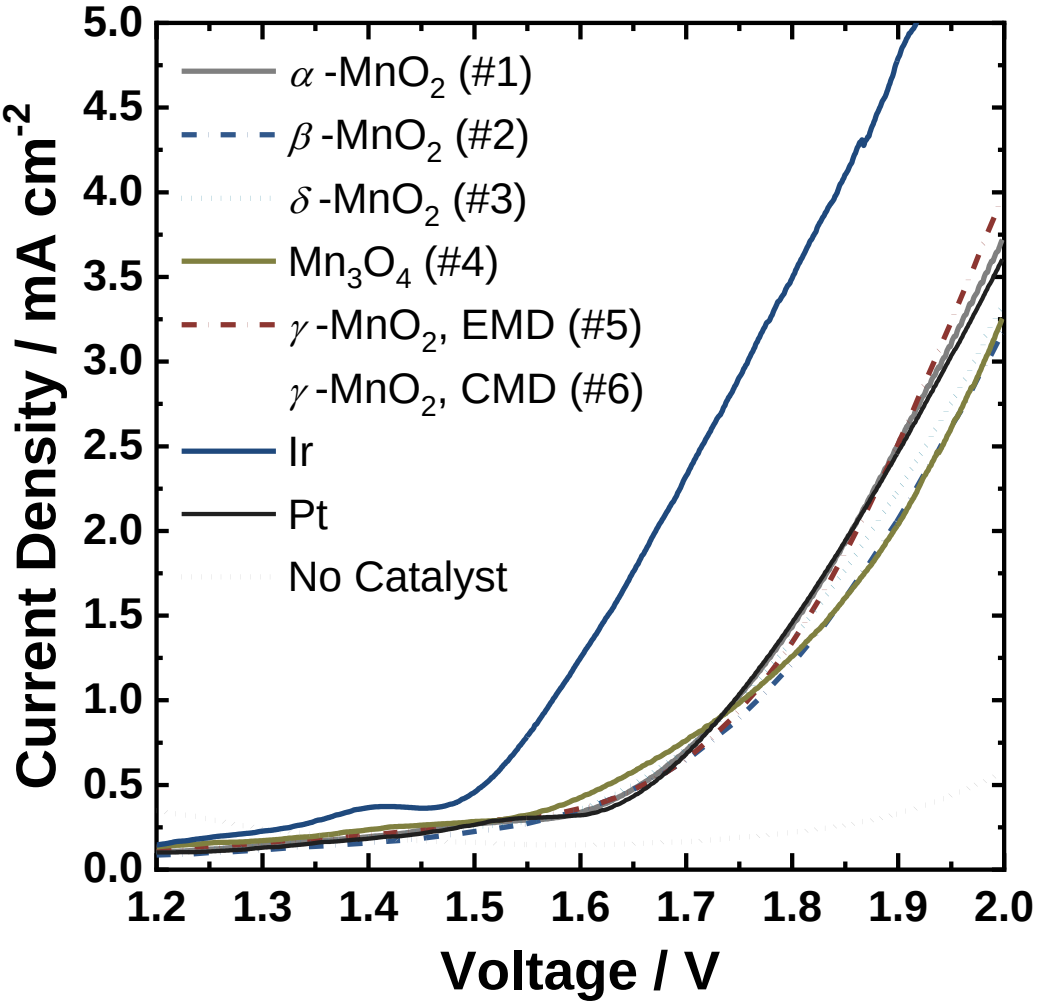

Figure 4.4 | Current density-voltage curves of PEM electrolyzers with the industrial Mn oxide samples, Ir, and Pt for the OER catalysts. (scan rate: 5 mV s^{-1}).

Using Ir, Pt, and γ-MnO_2 EMD (#5), the activity was further evaluated using a three-electrode system based on LSV curves and the slope of Tafel plots, referring a typical procedure to evaluate catalysts in the presence of Nafion ionomer.[37]

The comparable of the γ-MnO_2 EMD (#5) and Pt was confirmed by LSV curves measured using the three-electrode system (Figure 4.5a). The difference in overpotential at 5 mV cm^{-2} was 36 mV, although the difference in overpotential at 5 mV cm^{-2} between γ-MnO_2 EMD (#5) and Ir was 250 mV (Figure 4.5a).

The slopes of Tafel plots were 220 mV dec^{-1}, 104 mV dec^{-1}, and 181 mV dec^{-1} for γ-MnO_2, EMD (#5), Ir/C, and Pt/C, respectively, as shown in Figure 4.5b. Though the slope is larger in the case of γ-MnO_2, EMD (#5) than the case of Pt, comparable current density at a certain constant potential was also confirmed in the measurement of the Tafel plots.

The typical values of Tafel slopes for the OER on MnO_2 and IrO_2 in neutral aqueous electrolyte are 120 mV dec^{-1} (Figure 2.2)[25] and 30–60 mV dec^{-1},[14,41] respectively. The higher slope values in the presence of Nafion ionomer may reflect slower diffusion of reaction species and a decrease of the local pH around the catalysts. The Tafel slope much larger than 120 mV dec^{-1}, which indicates that single electron transfer with a very high symmetry factor, β, or a chemical process occurring from the resting state of the catalyst is the turnover-limiting step,[42] was reported in the case of the OER catalyzed by a Mn oxide in acidic conditions.[25] Because the one-electron oxidation of Mn^{2+} to Mn^{3+} was turnover-limiting in the OER by Mn oxides when Mn^{3+} disproportionates to Mn^{2+} to Mn^{4+}, it is expected that the turnover-limiting step in this case is the one-electron oxidation of Mn^{2+} with a very high value of β. The Tafel slopes previously observed in the case of the OER by Pt catalysts were also larger than 120 mV dec^{-1}, probably due to the formation of surface oxide layers.[14]

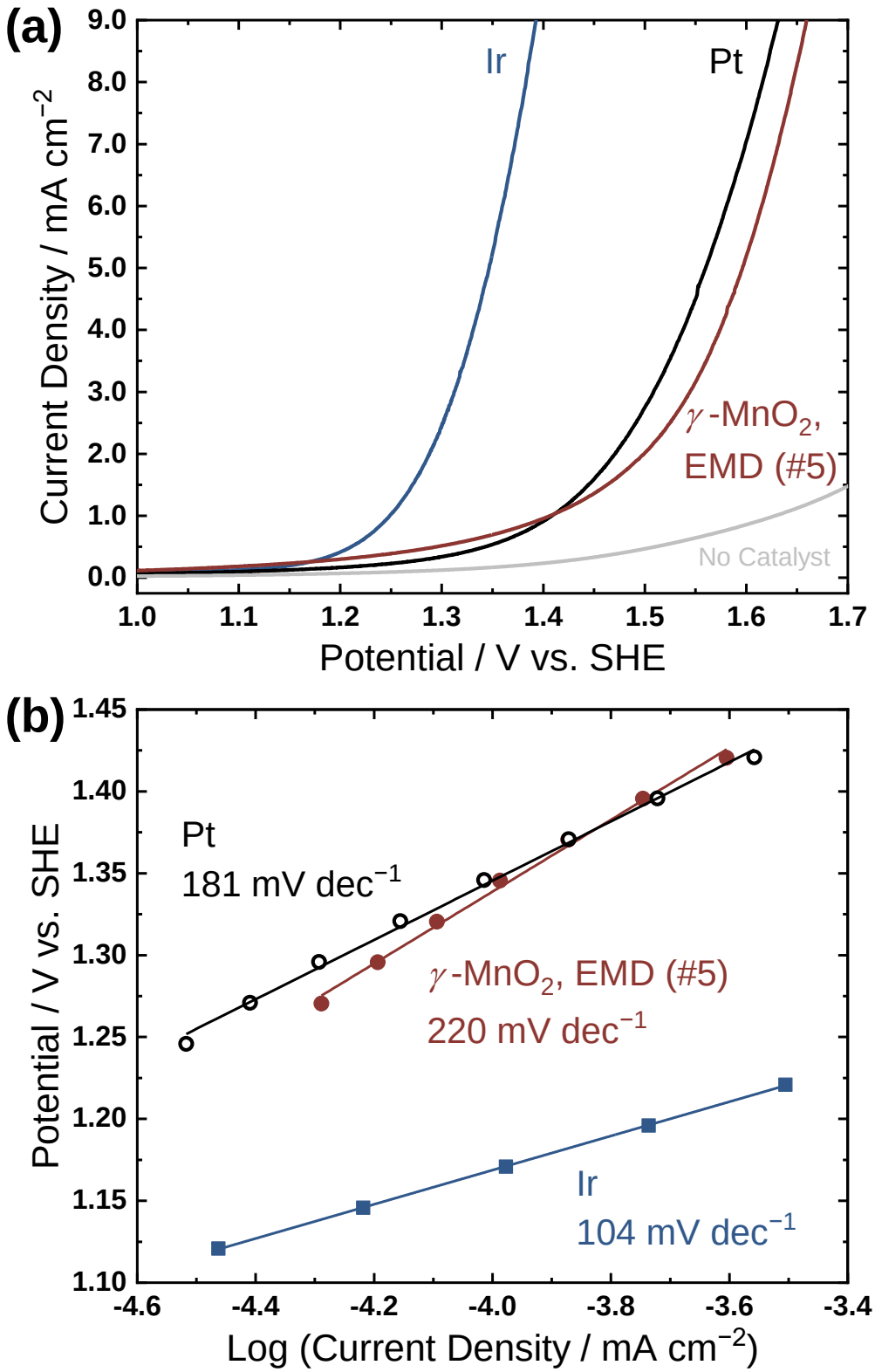

Figure 4.5 | (a) LSV curves (scan rate: 5 mV s^{-1}) and (b) Tafel plots of electrodes loaded with γ-MnO_2 (#5, EMD), Ir, or Pt in the presence of Nafion ionomer.

However, it is noted that the activity of the Mn oxide samples differed from each other when the evaluation of the OER activity was conducted in an acidic aqueous solution, in a similar way to previous studies for finding a suitable earth-abundant catalyst for PEM electrolyzers.[26,27,29,30,34] The OER activity evaluated by LSV is shown in Figure 4.6, and the current density at 1.7 V vs. RHE and overpotential at 0.5 mA cm^{-2} are summarized in Table 4.1.

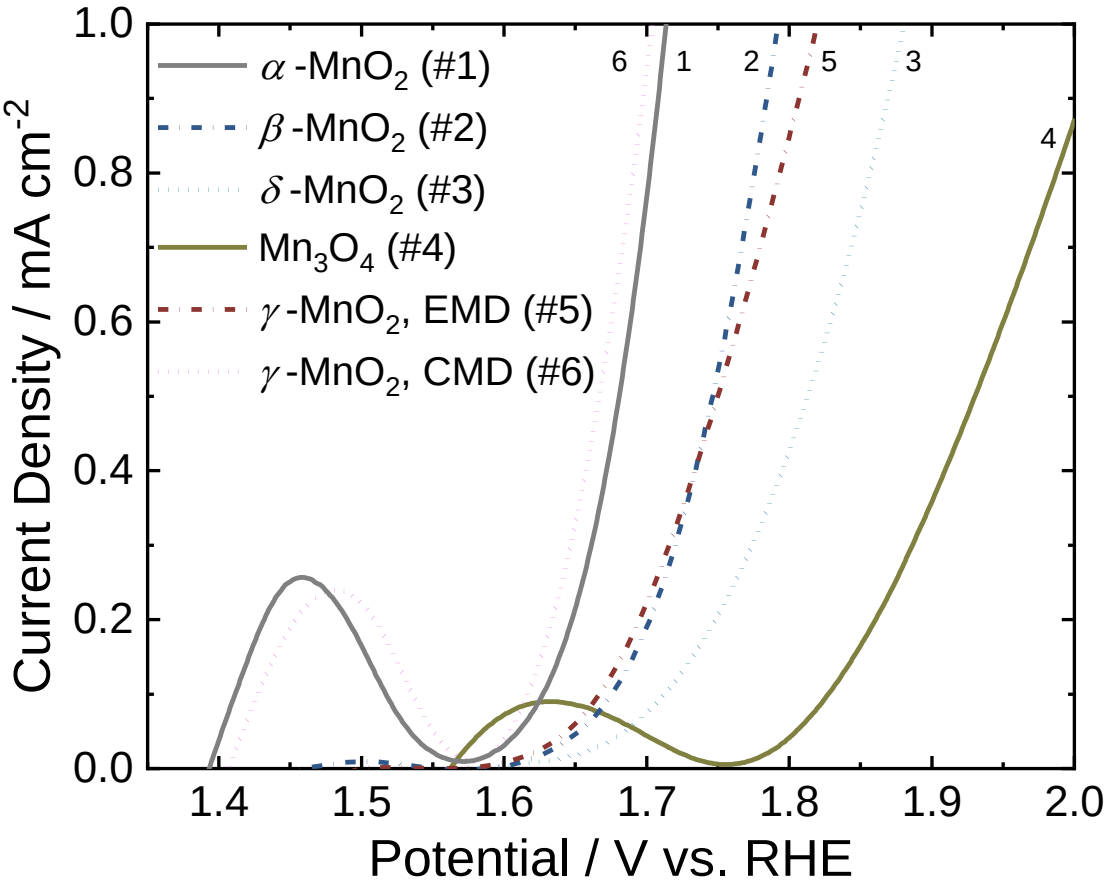

Figure 4.6 | (a) LSV curves of the industrial Mn oxide samples in 0.5 M Na_2SO_4 aqueous solution (pH 0.2 adjusted by addition of H_2SO_4) (scan rate: 10 mV s^{-1}).

In this study, six types of Mn oxides synthesized by industrial methods have been evaluated searching for an OER catalyst functional in PEM electrolyzers. As a result, it was demonstrated that the Mn oxides can exhibit comparable OER activity to that of Pt/C in PEM electrolyzers (Figure 4.4). As previously mentioned, 24.4% STH energy conversion efficiency was achieved by Sugiyama and Fujii *et al.* using PEM electrolyzers which use Pt/C for both the OER and the HER connected with solar cells.[35] Furthermore, many kinds of non-noble-metal-based catalysts for the HER which show comparable activity to that of Pt/C have been reported.[43] Thus, the present study suggests that STH energy conversion efficiency similar to the value demonstrated by Sugiyama and Fujii *et al.* may be able to be achieved using a PEM electrolyzer without noble metal catalysts.

It was also shown that the activity trends of the examined Mn oxide OER catalysts in an acidic aqueous electrolyte and in PEM electrolyzers were different (Figure 4.4 and 4.6). The presence of Nafion ionomer also affected the Tafel slope (Figure 4.5b). These results suggested that it is not enough to evaluate OER catalysts in an acidic aqueous electrolyte if one aims to find a suitable catalyst for PEM electrolyzers. This time, the OER catalysts which showed different activity in an aqueous acidic electrolyte showed similar activity in PEM electrolyzers. This result may indicate that the surface of Mn oxide samples became similar when contacted with Nafion ionomer.

For further development and realization of a system suitable for practical uses, two important issues remain: stability and further improvement of the activity. Considering the report by Nocera *et al.* about functionally stable OER catalysis by a Mn oxide[3] and the fact that, especially, the γ-MnO_2 (#5) is expected to be stable in acid in a certain condition since it was produced as the EMD in an acidic bath, it is expected that there is a condition where the catalyst can stably work. Investigation for such a condition is currently underway. As for the activity, the Mn oxide samples

were simply mechanically mixed with carbon black in this study but still showed comparable activity to that of Pt/C. Thus, it is expected that there is much room for improvement such as (electro)chemically growing a Mn oxide on the surface of carbon black. The large Tafel slope and the overpotential may also be able to be decreased by the stabilization of Mn^{3+}, which was proven successful in enhancing the OER activity in neutral aqueous solution.

4.4 Conclusions

In summary, it was discovered that the Mn oxide samples can readily show comparable activity for the OER to that of Pt/C in PEM electrolyzers. Also, it was demonstrated that the activity trends of the Mn oxides in an acidic aqueous electrolyte and in PEM electrolyzers are different, which indicate the importance of the evaluation of OER catalysts in PEM electrolyzers. The finding in this study demonstrates that Mn oxides are promising candidates for low-cost OER catalysts for PEM electrolyzers, the possibility of further improvement of the activity, and a way to the realization of non-noble-metal-free PEM electrolyzers for STH energy conversion with high efficiency.

References of Chapter 4

1. R. Pokhrel, M. K. Goetz, S. E. Shaner, X. Wu and S. S. Stahl, The “best catalyst” for water oxidation depends on the oxidation method employed: A case study of manganese oxides. *J. Am. Chem. Soc.* **2015**, *137*, 8384–8387.
2. K. Zeng and D. Zhang, Recent progress in alkaline water electrolysis for hydrogen production and applications. *Prog. Energy Combust. Sci.* **2010**, *36*, 307–326.
3. M. Carmo, D. L. Fritz, J. Mergel and D. Stolten, A comprehensive review on PEM water electrolysis. *Int. J. Hydrogen Energy* **2013**, *38*, 4901–4934.
4. M. A. Laguna-Bercero, Recent advances in high temperature electrolysis using solid oxide fuel cells. *J. Power Sources* **2012**, *203*, 4–16.
5. L. Bi, S. Boulfrad and E. Traversa, Steam electrolysis by solid oxide electrolysis cells (SOECs) with proton-conducting oxides. *Chem. Soc. Rev.* **2014**, *43*, 8255–8270.
6. T. Reier, H. N. Nong, D. Teschner, R. Schlögl and P. Strasser, Electrocatalytic oxygen evolution reaction in acidic environments – reaction mechanisms and catalysts. *Adv. Energy Mater.* **2016**, *7*, 1601275.
7. J. R. Varcoe, P. Atanassov, D. R. Dekel, A. M. Herring, M. A. Hickner, P. A. Kohl, A. R. Kucernak, W. E. Mustain, K. Nijmeijer, K. Scott, T. Xu and L. Zhuang, Anion-exchange membranes in electrochemical energy systems. *Energy Environ. Sci.* **2014**, *7*, 3135–3191.
8. L. Xiao, S. Zhang, J. Pan, C. Yang, M. He, L. Zhuang and J. Lu, First implementation of alkaline polymer electrolyte water electrolysis working only with pure water. *Energy Environ. Sci.* **2012**, *5*, 7869–7871.
9. C. C. Pavel, F. Cecconi, C. Emiliani, S. Santiccioli, A. Scaffidi, S. Catanorchi and M. Comotti, Highly efficient platinum group metal free based membrane-electrode assembly for anion exchange membrane water electrolysis. *Angew. Chem., Int. Ed.* **2014**, *53*, 1378–

1381.

10. W. M. Haynes, *CRC handbook of chemistry and physics*. CRC Press, Boca Raton, Florida, U. S. A., **2014**.
11. M. Auinger, I. Katsounaros, J. C. Meier, S. O. Klemm, P. U. Biedermann, A. A. Topalov, M. Rohwerder and K. J. J. Mayrhofer, Near-surface ion distribution and buffer effects during electrochemical reactions. *Phys. Chem. Chem. Phys.* **2011**, *13*, 16384–16394.
12. I. Katsounaros, J. C. Meier, S. O. Klemm, A. A. Topalov, P. U. Biedermann, M. Auinger and K. J. J. Mayrhofer, The effective surface pH during reactions at the solid-liquid interface. *Electrochem. Commun.* **2011**, *13*, 634–637.
13. Y. Zhao, N. M. Vargas-Barbosa, E. A. Hernandez-Pagan and T. E. Mallouk, Anodic deposition of colloidal iridium oxide thin films from hexahydroxyiridate(IV) solutions. *Small* **2011**, *7*, 2087–2093.
14. T. Reier, M. Oezaslan and P. Strasser, Electrocatalytic oxygen evolution reaction (OER) on Ru, Ir, and Pt catalysts: A comparative study of nanoparticles and bulk materials. *ACS Catal.* **2012**, *2*, 1765–1772.
15. Y. Lee, J. Suntivich, K. J. May, E. E. Perry and Y. Shao-Horn, Synthesis and activities of rutile IrO_2 and RuO_2 nanoparticles for oxygen evolution in acid and alkaline solutions. *J. Phys. Chem. Lett.* **2012**, *3*, 399–404.
16. O. Diaz-Morales, S. Raaijman, R. Kortlever, P. J. Kooyman, T. Wezendonk, J. Gascon, W. T. Fu and M. T. M. Koper, Iridium-based double perovskites for efficient water oxidation in acid media. *Nat. Commun.* **2016**, *7*, 12363.
17. L. C. Seitz, C. F. Dickens, K. Nishio, Y. Hikita, J. Montoya, A. Doyle, C. Kirk, A. Vojvodic, H. Y. Hwang, J. K. Norskov and T. F. Jaramillo, A highly active and stable $IrO_x/SrIrO_3$ catalyst for the oxygen evolution reaction. *Science* **2016**, *353*, 1011–1014.

18. K. Macounová, J. Jirkovský, M. V. Makarova, J. Franc and P. Krtil, Oxygen evolution on $Ru_{1-x}Ni_xO_{2-y}$ nanocrystalline electrodes. *J. Solid State Electrochem.* **2009**, *13*, 959–965.

19. T. Reier, Z. Pawolek, S. Cherevko, M. Bruns, T. Jones, D. Teschner, S. Selve, A. Bergmann, H. N. Nong, R. Schlögl, K. J. J. Mayrhofer and P. Strasser, Molecular insight in structure and activity of highly efficient, low-Ir Ir–Ni oxide catalysts for electrochemical water splitting (OER). *J. Am. Chem. Soc.* **2015**, *137*, 13031–13040.

20. S. Kumari, B. P. Ajayi, B. Kumar, J. B. Jasinski, M. K. Sunkara and J. Spurgeon, A low-noble-metal $W_{1-x}Ir_xO_{3-\delta}$ water oxidation electrocatalyst for acidic media via rapid plasma synthesis. *Energy Environ. Sci.* **2017**, *10*, 2432–2440.

21. C. P. De Pauli and S. Trasatti, Composite materials for electrocatalysis of O_2 evolution: IrO_2 + SnO_2 in acid solution. *J. Electroanal. Chem.* **2002**, *538–539*, 145–151.

22. T. Nakagawa, C. A. Beasley and R. W. Murray, Efficient electro-oxidation of water near its reversible potential by a mesoporous IrO_x nanoparticle film. *J. Phys. Chem. C* **2009**, *113*, 12958–12961.

23. D. Chandra, N. Abe, D. Takama, K. Saito, T. Yui and M. Yagi, Open pore architecture of an ordered mesoporous IrO_2 thin film for highly efficient electrocatalytic water oxidation. *ChemSusChem* **2015**, *8*, 795–799.

24. H.-S. Oh, H. N. Nong, T. Reier, M. Gliech and P. Strasser, Oxide-supported Ir nanodendrites with high activity and durability for the oxygen evolution reaction in acid PEM water electrolyzers. *Chem. Sci.* **2015**, *6*, 3321–3328.

25. M. Huynh, D. K. Bediako and D. G. Nocera, A functionally stable manganese oxide oxygen evolution catalyst in acid. *J. Am. Chem. Soc.* **2014**, *136*, 6002–6010.

26. R. Frydendal, E. A. Paoli, I. Chorkendorff, J. Rossmeisl and I. E. L. Stephens, Toward an active and stable catalyst for oxygen evolution in acidic media: Ti-stabilized MnO_2. *Adv.*

Energy Mater. **2015**, *5*, 1500991.

27. P. P. Patel, M. K. Datta, O. I. Velikokhatnyi, R. Kuruba, K. Damodaran, P. Jampani, B. Gattu, P. M. Shanthi, S. S. Damle and P. N. Kumta, Noble metal-free bifunctional oxygen evolution and oxygen reduction acidic media electrocatalysts. *Sci. Rep.* **2016**, *6*, 28367.
28. L. Han, P. Tang, Á. Reyes-Carmona, B. Rodríguez-García, M. Torréns, J. R. Morante, J. Arbiol, and J. R. Galan-Mascaros, Enhanced activity and acid pH stability of Prussian blue-type oxygen evolution electrocatalysts processed by chemical etching. *J. Am. Chem. Soc.* **2016**, *138*, 16037–16045.
29. Z.-H. Xue, H. Su, Q.-Y. Yu, B. Zhang, H.-H. Wang, X.-H. Li and J.-S. Chen, Janus Co/CoP nanoparticles as efficient Mott-Schottky electrocatalysts for overall water splitting in wide pH range. *Adv. Energy Mater.* **2017**, *7*, 1602355.
30. J. Wu, M. Liu, K. Chatterjee, K. P. Hackenberg, J. Shen, X. Zou, Y. Yan, J. Gu, Y. Yang, J. Lou and P. M. Ajayan, Exfoliated 2D transition metal disulfides for enhanced electrocatalysis of oxygen evolution reaction in acidic medium. *Adv. Mater. Interfaces* **2016**, *3*, 1500669.
31. J. S. Mondschein, J. F. Callejas, C. G. Read, J. Y. C. Chen, C. F. Holder, C. K. Badding and R. E. Schaak, Crystalline cobalt oxide films for sustained electrocatalytic oxygen evolution under strongly acidic conditions. *Chem. Mater.* **2017**, *29*, 950–957.
32. M. Blasco-Ahicart, J. Soriano-López, J. J. Carbó, J. M. Poblet and J. R. Galan-Mascaros, Polyoxometalate electrocatalysts based on earth-abundant metals for efficient water oxidation in acidic media. *Nat. Chem.* **2018**, *10*, 24–30.
33. M. Huynh, T. Ozel, C. Liu, E. C. Lau and D. G. Nocera, Design of template-stabilized active and earth-abundant oxygen evolution catalysts in acid. *Chem. Sci.* **2017**, *8*, 4779–4794.
34. I. A. Moreno-Hernandez, C. A. MacFarland, C. G. Read, K. M. Papadantonakis, B. S.

Brunschwig and N. S. Lewis, Crystalline nickel manganese antimonate as a stable water-oxidation catalyst in aqueous 1.0 M H_2SO_4. *Energy Environ. Sci.* **2017**, *10*, 2103–2108.

35. A. Nakamura, Y. Ota, K. Koike, Y. Hidaka, K. Nishioka, M. Sugiyama and K. Fujii, A 24.4% solar to hydrogen energy conversion efficiency by combining concentrator photovoltaic modules and electrochemical cells. *Appl. Phys. Exp.* **2015**, *8*, 107101.
36. A. Yamaguchi, R. Inuzuka, T. Takashima, T. Hayashi, K. Hashimoto and R. Nakamura, Regulating proton-coupled electron transfer for efficient water splitting by manganese oxides at neutral pH. *Nat. Commun.* **2014**, *5*, 4256.
37. F. Jaouen, V. Goellner, M. Lefèvre, J. Herranz, E. Proietti and J. P. Dodelet, Oxygen reduction activities compared in rotating-disk electrode and proton exchange membrane fuel cells for highly active Fe–N–C catalysts. *Electrochim. Acta* **2013**, *87*, 619–628.
38. A. Biswal, B. C. Tripathy, K. Sanjay, T. Subbaiah and M. Minakshi, Electrolytic manganese dioxide (EMD): a perspective on worldwide production, reserves and its role in electrochemistry. *RSC Adv.* **2015**, *5*, 58255–58283.
39. Y. Chabre and J. Pannetier, Structural and electrochemical properties of the proton / γ-MnO_2 system. *Prog. Solid State Chem.* **1995**, *23*, 1–130.
40. K. Fujii, S. Nakamura, M. Sugiyama, K. Watanabe, B. Bagheri and Y. Nakano, Characteristics of hydrogen generation from water splitting by polymer electrolyte electrochemical cell directly connected with concentrated photovoltaic cell. *Int. J. Hydrogen Energy* **2013**, *38*, 14424–14432.
41. H. Ooka, A. Yamaguchi, T. Takashima, K. Hashimoto and R. Nakamura, Efficiency of oxygen evolution on iridium oxide determined from the pH dependence of charge accumulation. *J. Phys. Chem. C* **2017**, *121*, 17873–17881.
42. Y. Surendranath, M. W. Kanan and D. G. Nocera, Mechanistic studies of the oxygen

evolution reaction by a cobalt-phosphate catalyst at neutral pH. *J. Am. Chem. Soc.* **2010**, *132*, 16501–16509.

43. C. C. L. McCrory, S. Jung, I. M. Ferrer, S. M. Chatman, J. C. Peters and T. F. Jaramillo, Benchmarking hydrogen evolving reaction and oxygen evolving reaction electrocatalysts for solar water splitting devices. *J. Am. Chem. Soc.* **2015**, *137*, 4347–4357.

Chapter 5.
Conclusions and Perspectives

Conclusions

This study successfully enhanced the multi-electron-transfer ability of Mn oxides both in aqueous electrolyte and PEM electrolyzers, by considering not only the properties as bulk materials such as crystal phases but also the bonding structures at the interface between solid and liquid phases and the factors related to proton and electron transfers such as ligands or distortion, learning from the Mn_4 cluster in PSII. This study aimed to maximize the multi-electron-transfer ability of Mn oxides by stabilizing Mn^{3+} by introducing stable ligands to induce CPET or distortion to the crystal structure.

In Chapter 2, the focus was put on the role of the amino-acid ligands of the Mn_4 cluster in PSII. While OER activity of the systems composed of Mn oxides and organic ligands generally gradually decreased because of the self-oxidation of the organic ligands, the Mn_4 cluster of PSII stably catalyzes the OER and the TON reaches as high as ~10^6.[1] Therefore, the amino-acid ligands of the Mn_4 cluster were regarded as the candidates for the stable ligands to induce CPET to enhance the OER activity. Using artificial amino-acid analogs and α-MnO_2, which was proposed to be the origin of the Mn_4 cluster,[2,3] as a model system, the effect and possible oxidation pathways of the organic compounds were analyzed and compared them with extant PSII from the viewpoint of energetics. As a result, it was demonstrated that benzoate, which possesses a carboxyl group, can enhance the OER activity of α-MnO_2 by inducing CPET. The changes of the onset potential of the anodic current corresponded to the shift of the onset potential of the OER. The changes in the reaction mechanism were revealed by the measurement of electrokinetics and H/D KIE. Also, it was found that benzoate and the surface of α-MnO_2 form outer-sphere complexes *via* water

molecules, the coordination structure analogous to D1-Asp61 on the Mn_4 cluster.[4] Among the seven direct amino-acid ligands of the Mn_4 cluster, six are the carboxyl group.[4] Also, D1-Asp61 is proposed to induce CPET in Kok cycle and serve as a starting point for a hydrogen-bond network to transfer protons to lumen.[5] Thus, the enhancement of the OER activity by benzoate indicated a possibility that carboxyl groups have been selectively incorporated around the Mn_4 cluster in the course of the evolution of PSII. Also, it was demonstrated that the introduction of organic acid ligands which are stable and able to induce CPET can be an effective strategy to stably enhance the OER activity of Mn oxides. On the other hand, the addition of guanidine did not cause apparent changes in both the anodic current and the OER, and imidazole was oxidized at more negative potential than the region the OER proceeded. The stability of the imidazolyl group was found to be a distinct difference between PSII and the model system. By the analysis of energetics, imidazolyl groups were suggested to be oxidized on α-MnO_2 *via* a proton-coupled multi-electron oxidation pathway, while both single and multi-electron oxidation reactions of D1-His332, whose transient oxidation has been discussed,[6–13] are effectively inhibited in PSII.

While the introduction of organic acid ligands was found to be a viable strategy to stably stabilize Mn^{3+} for the enhancement of the OER activity of Mn oxides, if the stabilization of Mn^{3+} can be achieved by engineering the crystal structure of Mn oxides, the stability problems of the ligands can be completely solved. In Chapter 3, the focus was put on recently reported 10-nm-sized Mn oxide NPs. The NPs showed distinctly higher OER activity than conventional bulk Mn oxides,[14] but the reason was unknown. It was hypothesized that Mn^{3+} can be easily stabilized on NPs because of the ligand fields which are readily or can be easily distorted due to the large ratio of the number of the surface atoms to the total atoms. To reveal the reason for the enhancement of the OER activity, comprehensive electrochemical and *in-situ* spectrochemical analysis of the reaction mechanism was conducted. *In-situ* electrochemical Raman spectroscopy clearly revealed

the flexible and reversible valency changes of Mn between Mn^{2+}, Mn^{3+}, and Mn^{4+} in the potential region less positive than that for the OER, suggesting that the charge accumulation is no longer the RDS in the case of the NPs. Also, it is noted that, probably because of the high ratio of the surface atoms, the Raman spectra were able to be obtained without the surface enhancement effect by noble metal substrates. The Raman spectra also revealed the flexible changes in the bonding structures. The flexible and reversible changes of the valency, as well as proton transfer during the valency changes, were confirmed by CV, EPR, *in-situ* UV–vis, and *in-situ* XAS measurement. The results suggested that, in the case of the NPs, the RDS is not charge accumulation but O–O bond formation and that the Mn oxides whose surface bonding structure can flexibly change and accommodate distortion in the ligand field of Mn can show substantially higher OER activity than conventional Mn oxide catalysts due to the stabilization of Mn^{3+}.

In Chapter 2 and 3, viable strategies to stably enhance the OER activity of Mn oxides by the stabilization of Mn^{3+} were revealed. For the application of the enhanced OER activity to industry or the global energy cycles, however, it will be essential to consider what type of device configuration will be used to convert renewable energy to chemical fuels. PEM electrolyzers are clearly promising device configuration for efficient energy conversion.[15] Sugiyama and Fujii *et al.* demonstrated that PEM electrolyzers with Pt/C as the OER catalyst connected with solar cells can achieve as high as 24.4% STH energy conversion efficiency.[16] Also, Mn oxides for the devices can hopefully be synthesized on an industrial scale. Thus, evaluation of six types of Mn oxides synthesized by industrial methods provided by Tosoh Corporation, a supplier of electrolytic Mn dioxides (EMDs) which is one and only in Japan and largest in the world, was conducted in PEM electrolyzers (Chapter 4). As a result, it was demonstrated that the examined Mn oxides can readily show comparable OER activity to that of Pt/C. Also, curiously, in an acidic aqueous electrolyte which is often used for the search for the OER catalysts suitable for PEM electrolyzers,

the activity trend between the Mn oxide samples was different from the trend in PEM electrolyzers. This result suggested the importance of the evaluation of OER catalysts in actual reaction conditions in target devices.

Overall, considering the natural and artificial systems to convert renewable energy to chemical fuels, PSII and PEM electrolyzers, this study demonstrated viable approaches to stably stabilize Mn^{3+} to enhance the OER activity of Mn oxides in non-alkaline conditions, as well as the importance of the consideration of the surface bonding structures including the surrounding environment or ligands and their dynamic changes during the reaction, in addition to the bulk structure of the catalyst, for the maximization of multi-electron-transfer ability of Mn oxides for the OER.

Perspectives

Insight into Design Strategy and Computational Models for Multi-Electron-Transfer Catalysts

As noted previously, not only the OER, but also other multi-electron transfer reactions such as carbon dioxide fixation, the ORR, nitrogen fixation, sulfate reduction, nitrate reduction, and the HER have essential roles in the global energy and material cycles and metabolism of organisms. The dynamic structural changes and the interaction of the reactants and products with not only the reaction center but also surrounding molecules should be important for the catalysis in the enzymes catalyzing those other reactions too. For example, in the case of carbon monoxide dehydrogenase (CODH) of *Carboxydothermus hydrogenoformans*, which can reversibly catalyze the conversion between carbon dioxide and carbon monoxide with high turnover number, His93 and Lys563 also coordinate to carbon dioxide when it is on the $[NiFe_4S_4]$ reaction center, according to the crystal structure analysis (Figure 5.1).[17]

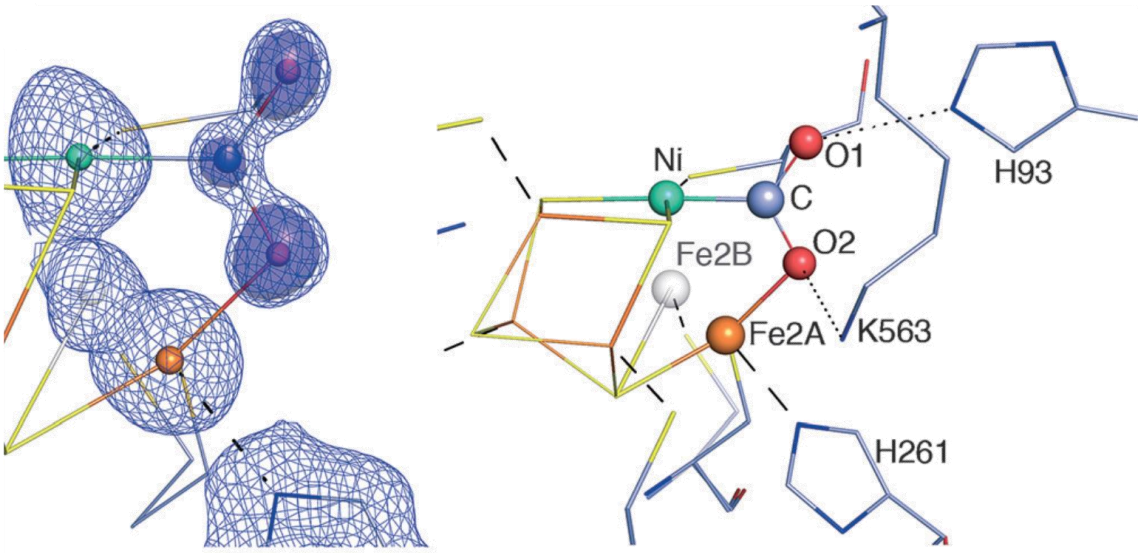

Figure 5.1 | The structure of carbon dioxide bound to the [$NiFe_4S_4$] reaction center of CODH of *C. hydrogenoformans*. $2F_o–F_c$ maps are shown with the refined model. The right panel is the ball-and-stick model of the cluster and the second coordination sphere. The colors of atoms: C (Gray-blue), N (blue), O (red), S (yellow), Fe (orange), and Ni (cyan). Adapted with permission from ref. 17. Copyright 2015 Wiley-VCH Verlag GmbH & Co. KGaA, Weinheim.

However, as summarized in Section 1.3.2.3, in the theoretical approaches for the development of OER catalysts, the extension of the theory to the three-dimensional surfaces has just recently started. This study demonstrated the importance of the consideration of dynamic structural changes of the bonding structure of both the surface of the catalysts and external ligands. Such kind of dynamic changes is usually, however, not considered in theoretical approaches for the development of artificial electrocatalysts. Based on the results of this study, it is expected that the more explicit consideration in calculation of the changes in the surface structure which is most stable at certain potential or external ligands is a promising direction to improve the existing theoretical approaches summarized in Section 1.3.2.3 and will help to find active catalysts in actual reaction environment where additives or ionomers may exist.

Potential Achievement of High STH Energy Conversion Efficiency

The comparable OER activity of Mn oxides to that of Pt/C in PEM electrolyzers suggested that it would be possible to achieve high STH energy conversion efficiency by PEM electrolyzers connected with solar cells without using noble metal OER catalysts, because STH energy conversion efficiency as high as 24.4% was already achieved by PEM electrolyzers with Pt/C as the OER catalyst connected to solar cells.[16] The perspective from and the meaning of the above result are herein summarized.

Figure 5.2 and Table 5.1 show STH energy conversion efficiency reported so far in chronological order. At the time when Ager *et al.* summarized the reported efficiency in 2015 (Figure 5.2),[18] the highest efficiency was 18.3% achieved by Licht *et al.* using an AlGaAs/Si photoelectrode with platinum as the electrocatalyst for the HER and RuO_2 for the OER.[19] After this summary (Figure 5.2), Spiccia *et al.* reported 22% using an alkaline electrolyzer with Ni form electrodes and 1 M NaOH connected with a multi-junction solar cell.[20] Soon after that, the report about the 22.4% STH energy conversion efficiency was published.[16] Jaramillo *et al.* later demonstrated that the efficiency can be more than 30% if PEM electrolyzers with Ir OER catalysts are connected to solar cells (Table 5.1).[21] The 22.4% STH energy conversion efficiency is significantly higher than the efficiency reported before 2015 and already higher than the target to be achieved by 2020 set by United States Department of Energy (15% STH energy conversion efficiency and \$17.30 kg^{-1} H_2 by 2015, 20% STH and \$5.70 kg^{-1} H_2 by 2020, and ultimately 25% STH and \$2.10 kg^{-1} H_2).[18,22]

From the target values, it can be noticed that the current challenge is the reduction of the cost of hydrogen production. Ayers *et al.* reported that the cost of the catalyst coated membrane becomes a major cost driver when the power of PEM electrolyzers is in the order of megawatt.[23] It is also important to note that the scarcity of rare metals may fundamentally limit the spread of

PEM electrolyzers for large-scale energy conversion systems. Vesborg *et al.* reported the results of their analysis showing that nine tons of Ir are produced per year while 300 tons of electrocatalysts are needed for each electrode for water electrolysis per one terawatt.[24]

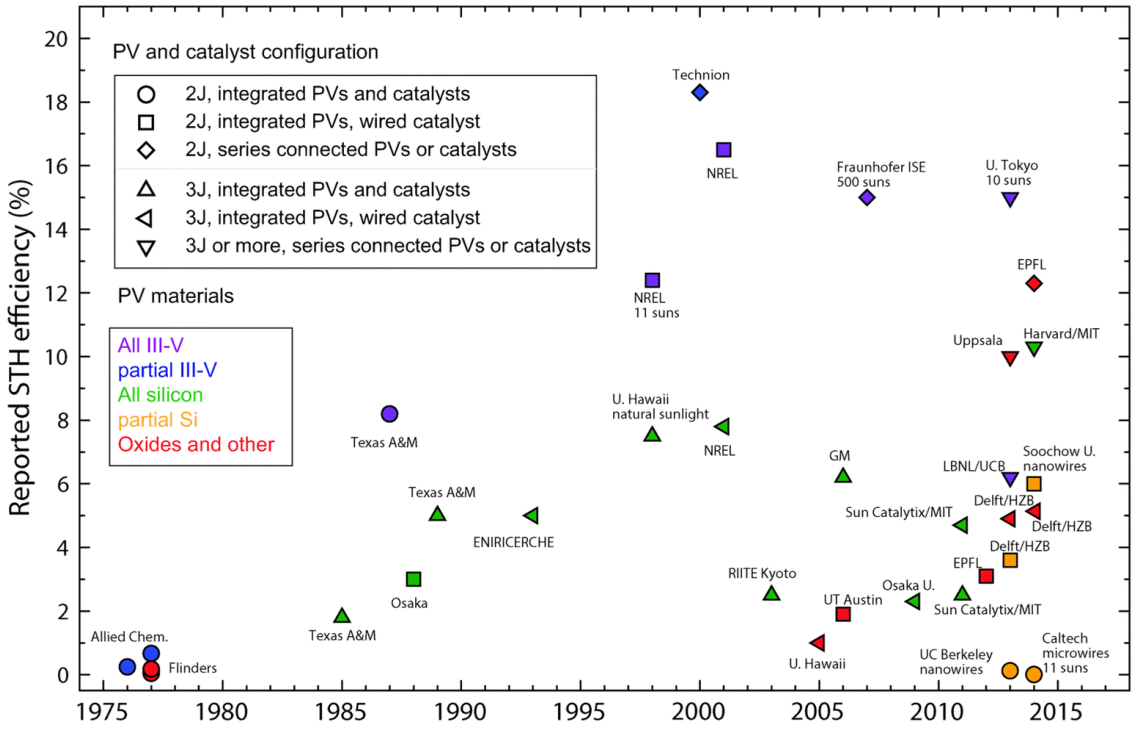

Figure 5.2 | Reported STH energy conversion efficiencies shown in chronological order. Different colors and shapes of the marks mean different configurations of PVs and catalysts and different kinds of materials for PVs, respectively. Reproduced from ref. 22 with permission of The Royal Society of Chemistry.

Table 5.1 | Reported STH energy conversion efficiencies after those in Figure 5.2.

Year	STH efficiency	Configuration of electrolyzer	Ref.
2015	22%	Alkaline electrolyzer with Ni form electrodes	20
2015	22.4%	PEM electrolyzers (Pt for both the OER and the HER)	16
2016	>30%	PEM electrolyzers (Ir for the OER and Pt for the HER)	21

As discussed in Section 4.3, the stability still remains as the problem in PEM electrolyzers developed in this study using Mn oxides. Nevertheless, it can be emphasized that the comparable OER activity was achieved using Mn oxides in PEM electrolyzers to the cases with Pt/C. The resolution of the stability problems in PEM electrolyzers using Mn oxide OER catalysts will be a large step toward the large-scale usage of STH energy conversion systems.

Selectivity for OER Catalysts

Selectivity issues have usually not been considered in the case of OER catalysts because other molecules than water are not regarded as the reactant when only inert molecules are in the electrolyte. Motivated by the previous success of the introduction of organic ligands to stabilize Mn^{3+} and enhance the OER activity of Mn oxides, this study dealt with the selectivity issues between water and other molecules in Chapter 2, with the attention on the surrounding molecules around the Mn_4 cluster in PSII. Although the carboxyl group was found to be a viable ligand for the enhancement of the OER activity of Mn oxides and the possible reasons for the absence of the oxidation of histidine ligands in PSII were discussed to some extent, the reason for the difference in the stability of imidazolyl groups in PSII and artificial systems has not been unambiguously clarified. Clarification of the mechanism by which the oxidation of imidazolyl groups in PSII is prevented, probably mostly based on the calculation, will aid in finding stable and efficient Mn-oxide-based systems for the OER.

It is noted here that the selectivity issue should be considered even when there are no external molecules which can be oxidized other than water. Binniger *et al.* reported based on thermodynamic reasoning that a lattice oxygen evolution reaction ($M^{2n+}O_n^{2-} \rightarrow M_{aq}^{2n+} + 1/2nO_2 + 2ne^-$, where M denotes a metal atom.) also proceeds at the potential where the OER proceeds.[25]

The consideration of the selectivity between the target reaction and the decomposition of catalysts may be important for the development of stable catalysts.

Also, selectivity issues are important in seawater electrolysis. Seawater exists in a huge amount on the earth and thus is an attractive candidate as the electron source for large-scale energy conversion systems from renewable energy to solar fuels. However, the evolution of toxic chlorine gas usually dominates in seawater electrolysis even though the thermodynamic potential for the OER is less positive than that for chlorine evolution ($2Cl^- \rightarrow Cl_2 + 2e^-$; E° = +1.36 V vs. SHE) in a wide range of pH. The ratio of the exchange current density for chlorine evolution to that for the OER was reported to be 1×10^3 to 1×10^7.[26]

Here, it is noted that a linear correlation between required electrode potentials for chlorine evolution and the OER was suggested by Trasatti,[28] and that the results of DFT calculation on rutile IrO_2 and RuO_2 (110) surfaces by Rossmeisl *et al.* revealed scaling relationships between adsorption energies of Cl, ClO, and O, which enabled the construction of volcano plots as shown in Figure 5.3.[28] The three volcanos for chlorine evolution correspond to three different pathways for the reaction. Parallelism in each part of the volcanos in Figure 5.3 for chlorine evolution and the OER constitutes the scaling relationships and supports the linear relationship suggested by Trasatti.[27] The reason for the lower potential for chlorine evolution than the potential for the OER was attributed to these scaling relationships and multiple reaction pathways for the chlorine evolution. For the OER to be the dominant reaction during the seawater oxidation, breaking the scaling relationships may be a key.

Again, the selectivity for the OER catalysts, which was considered in this study, will also be important for the development of stable catalysts or the catalysts for seawater electrolysis.

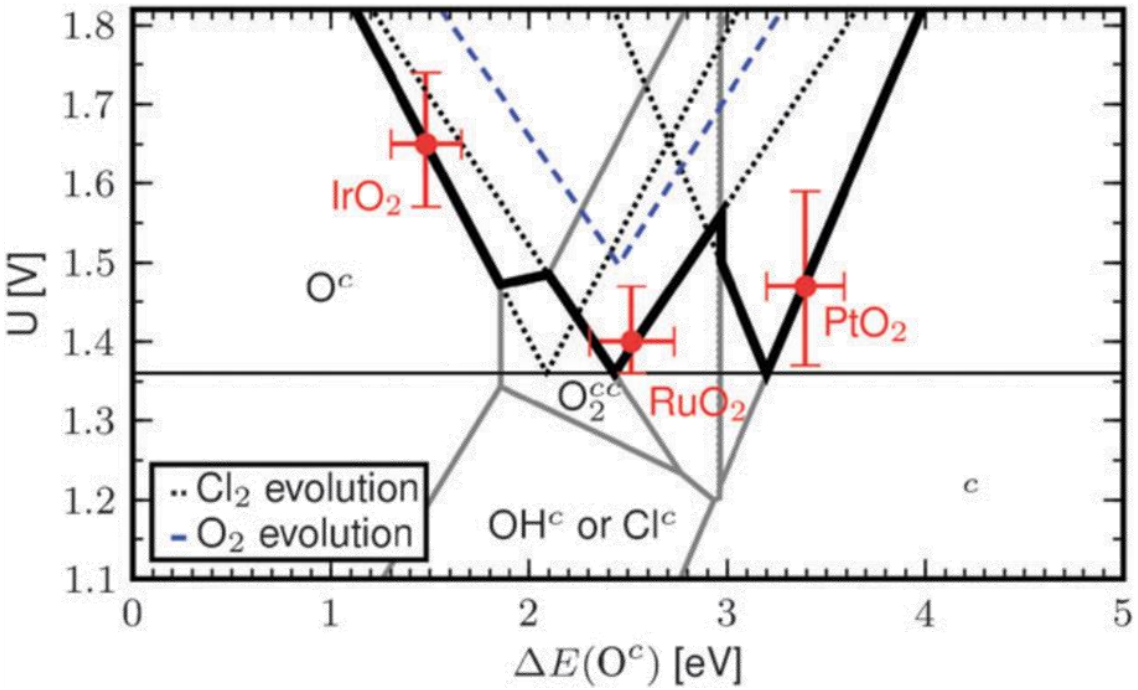

Figure 5.3 | Volcano-type plot which predicts the onset potential of chlorine evolution as a function of the adsorption energy of an oxygen atom at a coordinatively unsaturated site (O^c) on the rutile oxide (110) surface (thick solid black line). Black broken lines show the volcano-type plots depicted when only one of the three reaction pathways for chlorine evolution was considered. The blue broken line is the volcano-type plot which predicts the onset potential of the OER. The onset potential for chlorine evolution is predicted to be always more negative than that for the OER. Gray lines divide the regions where different surface structures are the most stable. Reproduced from ref. 28 with permission of The Royal Society of Chemistry.

References of Chapter 5

1. N. Cox, M. Retegan, F. Neese, D. A. Pantazis, A. Boussac and W. Lubitz, Electronic structure of the oxygen-evolving complex in photosystem II prior to O–O bond formation. *Science*, **2014**, *345*, 804–808.
2. M. J. Russell and A. J. Hall, presented in part at Sixth International Congress on Carbon Dioxide Utilization, Breckenridge, Colorado, U. S. A., September **2001**.
3. K. Sauer and V. K. Yachandra, A possible evolutionary origin for the Mn_4 cluster of the photosynthetic water oxidation complex from natural MnO_2 precipitates in the early ocean. *Proc. Natl. Acad. Sci. U. S. A.* **2002**, *99*, 8631–8636.
4. Y. Umena, K. Kawakami, J.-R. Shen and N. Kamiya, Crystal structure of oxygen-evolving photosystem II at a resolution of 1.9 Å. *Nature* **2011**, *473*, 55–61.
5. D. R. Weinberg, C. J. Gagliardi, J. F. Hull, C. F. Murphy, C. A. Kent, B. C. Westlake, A. Paul, D. H. Ess, D. G. McCafferty and T. J. Meyer, Proton-coupled electron transfer, *Chem. Rev.* **2012**, *112*, 4016–4093.
6. J. Yano and V. Yachandra, Mn_4Ca cluster in photosynthesis: Where and how water is oxidized to dioxygen. *Chem. Rev.* **2014**, *114*, 4175–4205.
7. N. Cox and J. Messinger, Reflections on substrate water and dioxygen formation. *Biochim. Biophys. Acta, Bioenerg.* **2013**, *1827*, 1020–1030.
8. A. Boussac, J.-L. Zimmermann, A. W. Rutherford and J. Lavergne, Histidine oxidation in the oxygen-evolving photosystem-II enzyme. *Nature* **1990**, *347*, 303–306.
9. B. J. Hallahan, J. H. A. Nugent, J. T. Warden and M. C. W. Evans, Investigation of the origin of the "S3" EPR signal from the oxygen-evolving complex of photosystem 2: the role of tyrosine Z. *Biochemistry* **1992**, *31*, 4562–4573.
10. A. Boussac and A. W. Rutherford, The origin of the split S_3 EPR signal in Ca^{2+}-depleted

photosystem II: Histidine versus tyrosine. *Biochemistry* **1992**, *31*, 7441–7445.

11. J. Stubbe and W. A. van der Donk, Protein radicals in enzyme catalysis. *Chem. Rev.* **1998**, *98*, 705–762.
12. M. L. Gilchrist, Jr., J. A. Ball, D. W. Randall and R. D. Britt, Proximity of the manganese cluster of photosystem II to the redox-active tyrosine Y_Z. *Proc. Natl. Acad. Sci. U. S. A.* **1995**, *92*, 9545–9549.
13. X.-S. Tang, D. W. Randall, D. A. Force, B. A. Diner and R. D. Britt, Manganese-tyrosine interaction in the photosystem II oxygen-evolving complex. *J. Am. Chem. Soc.* **1996**, *118*, 7638–7639.
14. K. Jin, A. Chu, J. Park, D. Jeong, S. E. Jerng, U. Sim, H.-Y. Jeong, C. W. Lee, Y-S. Park, K. D. Yang, G. K. Pradhan, D. Kim, N.-E. Sung, S. H. Kim and K. T. Nam, Partially oxidized sub-10 nm MnO nanocrystals with high activity for water oxidation catalysis. *Sci. Rep.* **2015**, *5*, 10279.
15. M. Carmo, D. L. Fritz, J. Mergel and D. Stolten, A comprehensive review on PEM water electrolysis. *Int. J. Hydrogen Energy* **2013**, *38*, 4901–4934.
16. A. Nakamura, Y. Ota, K. Koike, Y. Hidaka, K. Nishioka, M. Sugiyama and K. Fujii, A 24.4% solar to hydrogen energy conversion efficiency by combining concentrator photovoltaic modules and electrochemical cells. *Appl. Phys. Exp.* **2015**, *8*, 107101.
17. J. Fesseler, J.-H. Jeoung and H. Dobbek, How the $[NiFe_4S_4]$ cluster of CO dehydrogenase activates CO_2 and NCO^-. *Angew. Chem., Int. Ed.* **2015**, *54*, 8560–8564.
18. J. W. Ager, M. R. Shaner, K. A. Walczak, I. D. Sharp and S. Ardo, Experimental demonstrations of spontaneous, solar-driven photoelectrochemical water splitting. *Energy Environ. Sci.* **2015**, *8*, 2811–2824.
19. S. Licht, B. Wang, S. Mukerji, T. Soga, M. Umeno and H. Tributsch, Efficient solar water

splitting, exemplified by RuO_2-catalyzed AlGaAs/Si photoelectrolysis. *J. Phys. Chem. B* **2000**, *104*, 8920–8924.

20. S. A. Bonke, M. Wiechen, D. R. MacFarlane and L. Spiccia, Renewable fuels from concentrated solar power: towards practical artificial photosynthesis. *Energy Environ. Sci.* **2015**, *8*, 2791–2796.
21. J. Jia, L. C. Seitz, J. D. Benck, Y. Huo, Y. Chen, J. Wei D. Ng, T. Bilir, J. S. Harris and T. F. Jaramillo, Solar water splitting by photovoltaic-electrolysis with a solar-to-hydrogen efficiency over 30%. *Nat. Commun.* **2016**, *7*, 13237.
22. "DOE Technical Targets for Hydrogen Production from Photoelectrochemical Water Splitting." Office of Energy Efficiency & Renewable Energy, U. S. Department of Energy. https://energy.gov/eere/fuelcells/doe-technical-targets-hydrogen-production-photoelectrochemical-water-splitting (accessed January 1, 2018).
23. K. E. Ayers J. N. Renner N. Danilovic, J. X. Wang, Y. Zhang, R. Maric and H. Yu, Pathways to ultra-low platinum group metal catalyst loading in proton exchange membrane electrolyzers. *Catal. Today* **2016**, *262*, 121–132.
24. P. C. K. Vesborg and T. F. Jaramillo, Addressing the terawatt challenge: scalability in the supply of chemical elements for renewable energy. *RSC Adv.* **2012**, *2*, 7933–7947.
25. T. Binninger, R. Mohamed, K. Waltar, E. Fabbri, P. Levecque, R. Kötz and T. J. Schmidt, Thermodynamic explanation of the universal correlation between oxygen evolution activity and corrosion of oxide catalysts. *Sci. Rep.* **2015**, *5*, 12167.
26. J. E. Bennett. Electrodes for generation of hydrogen and oxygen from seawater. *Int. J. Hydrogen Energy* **1980**, *5*, 401–408.
27. S. Trasatti, Electrocatalysis in the anodic evolution of oxygen and chlorine. *Electrochim. Acta* **1984**, *29*, 1503–1512.

28. H. A. Hansen, I. C. Man, F. Studt, F. Abild-Pedersen, T. Bligaard and J. Rossmeisl, Electrochemical chlorine evolution at rutile oxide (110) surfaces. *Phys. Chem. Chem. Phys.* **2010**, *12*, 283–290.

List of Publications

For This Dissertation

1. **Toru Hayashi**, Akira Yamaguchi, Kazuhito Hashimoto, Ryuhei Nakamura
   "Stability of organic compounds on the oxygen-evolving center of photosystem II and manganese oxide water oxidation catalysts"
   Chemical Communications, Vol. 52, pp. 13760–13763, 2016 (Selected as Inside Back Cover).

2. Kyoungsuk Jin†, Hongmin Seo†, **Toru Hayashi†**, Mani Balamurugan, Donghyuk Jeong, Yoo Kyung Go, Jung Sug Hong, Kang Hee Cho, Hirotaka Kakizaki, Nadège Bonnet-Mercier, Min Gyu Kim, Sun Hee Kim, Ryuhei Nakamura, Ki Tae Nam
   "Mechanistic investigation of water oxidation catalyzed by uniform, assembled MnO nanoparticles"
   Journal of the American Chemical Society, Vol. 139, pp. 2277–2285, 2017. († K.J., H.S., and T.H. contributed equally.)

3. **Toru Hayashi**, Nadège Bonnet-Mercier, Akira Yamaguchi, Kazumasa Suetsugu, Ryuhei Nakamura
   "Electrochemical characterization of manganese oxides as a water oxidation catalyst in proton exchange membrane electrolysers"
   Royal Society Open Science, Vol. 6, Article No. 190122, 2019.

Others

4. Xiaoqing Qiu, Min Liu, **Toru Hayashi**, Masahiro Miyauchi, Kazuhito Hashimoto
   "Solution-based synthesis of pyrite films with enhanced photocurrent generation"
   Chemical Communications, Vol. 49, pp. 1232–1234, 2013.

5. Akira Yamaguchi, Riko Inuzuka, Toshihiro Takashima, **Toru Hayashi**, Kazuhito Hashimoto, Ryuhei Nakamura
   "Regulating proton-coupled electron transfer for efficient water splitting by manganese oxides at neutral pH"
   Nature Communications, Vol. 5, Article No. 4256, 2014.

6. Pengwei Wang, **Toru Hayashi**, Qing'an Meng, Qianbin Wang, Huan Liu, Kazuhito Hashimoto, Lei Jiang
   "Highly boosted oxygen reduction reaction activity by tuning the underwater wetting state of the superhydrophobic electrode"
   Small, Vol. 13, Article No. 1601250, 2017.

7. Hideshi Ooka, Toshihiro Takashima, Akira Yamaguchi, **Toru Hayashi**, Ryuhei Nakamura
   "Element strategy of oxygen evolution electrocatalysis based on *in situ* spectroelectrochemistry"
   Chemical Communications, Vol. 53, pp. 7149–7161, 2017.

8. Hirotaka Kakizaki, Hideshi Ooka, **Toru Hayashi**, Akira Yamaguchi, Nadège Bonnet-Mercier, Kazuhito Hashimoto, Ryuhei Nakamura
   "Evidence that crystal facet orientation dictates oxygen evolution intermediates on rutile manganese oxide"
   Advanced Functional Materials, Vol. 28, Article No. 1706319, 2018.

9. Ailong Li, Hideshi Ooka, Nadège Bonnet, **Toru Hayashi**, Yimeng Sun, Qike Jiang, Can Li, Hongxian Han, Ryuhei Nakamura
   "Stable potential windows for long-term electrocatalysis by manganese oxides under acidic conditions"
   Angewandte Chemie International Edition, Vol. 58, pp. 5054–5058, 2019.

10. Yuanqing Wang, **Toru Hayashi**, Daoping He, Yamei Li, Fangming Jin, Ryuhei Nakamura
    "A reduced imidazolium cation layer serves as the active site for electrochemical carbon dioxide reduction"
    Submitted.

Acknowledgement

This study was conducted under the supervision of Dr. Ryuhei Nakamura at RIKEN Center for Sustainable Resource Science (CSRS), to whom the supervision was officially delegated. I would like to express my sincere appreciation to Dr. Ryuhei Nakamura for his invaluable guidance and constant encouragement throughout the course of this research.

I deeply thank Prof. Hiroshi Ishikita and Prof. Kazuhito Hashimoto as the supervisors for the doctorate course.

I sincerely appreciate the instruction before this study from Prof. Lei Jiang at Institute of Chemistry, Chinese Academy of Sciences (ICCAS) and Beihang University, Dr. Huan Liu at Beihang University, and Dr. Bin Su at ICCAS during my stay there, and from Prof. Shuji Nakanishi, Dr. Kazuhide Kamiya, and Dr. Kayano Sunada.

I would like to express my profound gratitude also to the current and previous members of Biofunctional Catalyst Research Team, RIKEN CSRS, led by Dr. Nakamura, especially to Ms. Nadège Bonnet-Mercier and Dr. Akira Yamaguchi for their scientific and technical contribution to this study, Ms. Tomomi Minami for her kind daily assistance, and Dr. Hideshi Ooka, Mr. Hirotaka Kakizaki, Mr. Shogo Mori, Dr. Yamei Li, Mr. Ailong Li, Mr. Daoping He, Dr. Tetsuya Yamada, Dr. Nobuaki Shono, and Ms. Keiko Tsukamoto for their kind help. Support from Ms. Echiko Noritoshi at Ishikita Laboratory, The University of Tokyo is also gratefully acknowledged.

I truly appreciate the fruitful collaboration with Prof. Ki Tae Nam, Dr. Kyoungsuk Jin, and Mr. Hongmin Seo at Seoul National University, and Mr. Kazumasa Suetsugu at Tosoh Corporation.

I am deeply grateful to Dr. Xi Yao and Dr. Jie Ju at ICCAS and Dr. Chunmei Ding, Mr. Zhe Cheng, Ms. Zhaoyuan Liu, and Mr. Chi-Tat Cheng at Beihang University during my stay there, and Mr. Sosuke Higuchi and Ms. Junko Sakai for their friendship.

I am also profoundly thankful to all other people at The University of Tokyo, RIKEN, ICCAS, and Beihang University who provided their kind help. This work is also supported by Grant-in-Aid for JSPS Research Fellows (DC1) No. 15J10583.

Finally, my heartfelt gratitude goes to my father, Hiroshi Hayashi, my mother, Yurie Hayashi, and my younger brother, Wataru Hayashi, who always supported me to complete this work.

April 29, 2019

Toru Hayashi